博士論文

Plasmonic Materials on Periodic Titania Mesostructures for Photoelectrochemical and Photovoltaic Applications

（酸化チタン周期構造上へのプラズモン材料構築とその
光電気化学および光電変換への応用）

呉 玲

Table of Contents

Chapter 1 General Introduction

1.1 Introduction to Plasmonics

Plasmonics is a field that deals with fundamentals and applications of surface plasmon resonance (SPR) which is based on an interaction between electromagnetic radiation and conduction electrons at metal interfaces or in metal nanostructures, resulting in a localized optical near field and a far field scattering. SPR has attracted much interest in the last decades. There are more than 30,000 published papers with titles containing "plasmonics", "plasmonic", or "plasmon" (using Web of Science). Plasmonic structures can be applied to stained glass as coloring agents, sub-wavelength focusing beyond diffraction limit,[1,2] sensing,[3,4] surface-enhanced spectroscopy,[5-7] photocurrent enhancement for solar cells,[8-13] photocatalysis,[14-23] and so on. This chapter first focuses on the fundamental physics and applications of SPR. Then, a related phenomenon, plasmon-induced charge separation (PICS), is reviewed. Finally, the aims and outlines of this thesis are described.

1.2 Surface Plasmon Resonance (SPR)

1.2.1 Dielectric Function of Metal[24-28]

The first approximation to describe metal dielectric function is the Drude model, which only takes unbound free electrons into account. In this case, the dielectric function of metals is expressed as follows:

$$\varepsilon_{\mathrm{m}}(\omega) = 1 - \frac{\omega_{\mathrm{p}}^2}{\omega^2 + i\omega\gamma} \tag{1.1}$$

where ω_{p} is the plasma frequency, given by $\omega_{\mathrm{p}} = (\frac{ne^2}{\varepsilon_0 m_{\mathrm{e}}})^{1/2}$ (n: the free electron density, e: the electric charge, ε_0: the vacuum permittivity, m_{e}: the effective mass of the electrons), and γ is the bulk damping constant that is related to the mean free path of the electrons l and the Fermi velocity v_{F} by $\gamma = v_{\mathrm{F}}/l$. The damping of electron oscillation is caused by several processes including electron-electron collisions, electron-ion collisions, and electron-photon collisions. Considering that the complex

dielectric function is shown as $\varepsilon_{\mathrm{m}}(\omega) = \varepsilon'(\omega) + i\varepsilon''(\omega)$, the real and imaginary parts are given by

$$\varepsilon'(\omega) = 1 - \frac{\omega_{\mathrm{p}}^2}{\omega^2+\gamma^2} \tag{1.2}$$

$$\varepsilon''(\omega) = \frac{\omega_{\mathrm{p}}^2\gamma}{\omega(\omega^2+\gamma^2)} \tag{1.3}$$

For $\omega \gg \gamma$ (the case of almost no damping), the $\varepsilon_m(\omega)$ is predominantly real. The dielectric function can be written as

$$\varepsilon_m(\omega) = 1 - \frac{\omega_{\mathrm{p}}^2}{\omega^2} \tag{1.4}$$

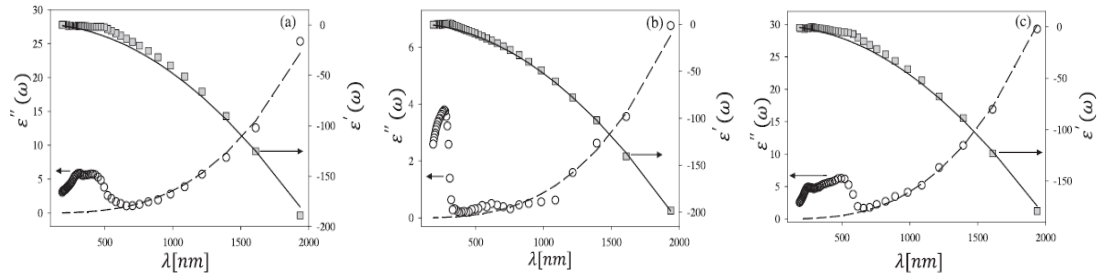

Figure 1.1 Real (solid line) and imaginary (dashed line) parts of the dielectric functions for (a) Au, (b) Ag and (c) Cu given by the Drude mode (Eq. 1.1). Grey squares and open circles represent the real and imaginary parts obtained from an experimental measurement, respectively. Reprinted with permission from ref. 26. Copyright 2014 AIP Publishing.

For noble metals such as Au, Ag, and Cu, the Drude model gives us an approximate description of the dielectric functions in the low-frequency regime (*e.g.* near-infrared (NIR) region) where the free electrons make a major contribution to the function. However, it is invalid at the high frequencies (e.g. visible to near-UV region), due to the contributions from the bound electrons by interband transitions from the deep d band to the sp band. Figure 1.1 shows the real and imaginary components of the dielectric functions for Au, Ag, and Cu, given by the Drude model and an experimental measurement.[26] The curves plotted according to the Drude model fit well with the experiment data in the wavelength range longer than 600 nm, 300 nm, and 600 nm for Au, Ag, and Cu, respectively. These are roughly consistent with the onsets of the

interband transitions, 2.3 eV for Au, 3.7 eV for Ag, and 2.1 eV for Cu.[28] It is obvious at the shorter wavelengths that the fittings break down because of an increase in imaginary part of the dielectric function caused by interband transitions.

1.2.2 Surface Plasmon Resonance (SPR)[24, 27]

In the visible to NIR wavelength range, light just penetrates into metal within the skin depth (tens of nanometers). For instance, the skin depth is 20 nm for Au at 500 nm incident wavelength. Consequently, only the free electrons at the metal surface are excited and forced to oscillate relative to the metal atoms, known as plasma oscillation. If the plasma oscillations are coupled to the incident photons, SPR occurs. There are two distinct SPRs: propagating surface plasmon resonance (PSPR) and localized surface plasmon resonance (LSPR) as illustrated in Figure 1.2.

(1) Propagating surface plasmon resonance (PSPR)

PSPR is an excitation of a coupled state between photons and plasma oscillations at the interface between metal and dielectric. As shown in Figure 1.2a, the electromagnetic surface wave propagates along the *x* direction as an evanescent wave. The PSPR is characterized by the following dispersion relation:

$$k_x = k_0\sqrt{\frac{\varepsilon_{\mathrm{m}}(\omega)\varepsilon_{\mathrm{d}}}{\varepsilon_{\mathrm{m}}(\omega)+\varepsilon_{\mathrm{d}}}} \tag{1.5}$$

where k_x is the wave vector of PSPR, $k_0 = \frac{\omega}{c}$ is the wave vector of incident light, ε_{d} is dielectric constant of the dielectric. Under the condition without damping of the electron oscillation, $\omega \gg \gamma$, substituting Eq. 1.4 into Eq. 1.5 yields

$$k_x = \frac{\omega}{c}\sqrt{\frac{(\omega^2-\omega_{\mathrm{p}}^2)\varepsilon_{\mathrm{d}}}{\omega^2(1+\varepsilon_{\mathrm{d}})-\omega_{\mathrm{p}}^2}} \tag{1.6}$$

When $\omega^2(1+\varepsilon_{\mathrm{d}})-\omega_{\mathrm{p}}^2$ approaches to 0, k_x diverges to infinity, indicating propagation of the electromagnetic surface wave along the *x* direction. Therefore, the frequency of PSPR is obtained as follows:

$$\omega_{\mathrm{PSPR}} = \frac{\omega_{\mathrm{p}}}{\sqrt{1+\varepsilon_{\mathrm{d}}}} \tag{1.7}$$

It can be concluded that the resonance frequency is strongly dependent on the dielectric

environment. The resonance wavelength red-shifts as ε_d increases. PSPR is thus used for optical sensing of refractive index changes on the metal surface. For the metals in air ($\varepsilon_d = 1$), $\omega_{PSPR} = \omega_p/\sqrt{2}$.

In Eq. 1.5, the value of the square root is larger than one for metals ($\sqrt{\frac{\varepsilon_m(\omega)\varepsilon_d}{\varepsilon_m(\omega)+\varepsilon_d}} > 1$), suggesting that the wave vector of the PSPR is greater than that of the incident light travelling in free space ($k_x > k_0$). Thus, PSPR can only be excited with special setups, such as prism and periodic structure.

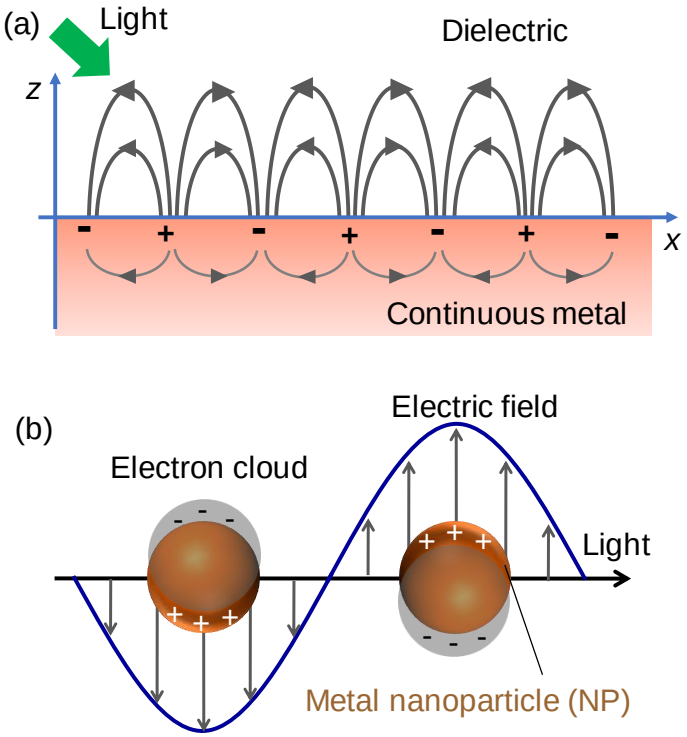

Figure 1.2 Schematic illustrations of (a) propagating surface plasmon resonance (PSPR) and (b) localized surface plasmon resonance (LSPR).

(2) Localized surface plasmon resonance (LSPR)

LSPR is a non-propagating excitation of SPR at the surface of metallic nanostructures. In the case of a metal nanosphere, the charge oscillation is different from that in the continuous metal film. If the particle size is much smaller than the light wavelength, a simple quasi-static (dipolar) approximation can be applied to the metal

nanosphere. Polarizability in the particle is given by

$$\alpha = 4\pi R^3 \frac{\varepsilon_m(\omega)-\varepsilon_d}{\varepsilon_m(\omega)+2\varepsilon_d} \tag{1.8}$$

where R is the radius of the nanosphere. Obviously, a minimum $|\varepsilon_m(\omega) + 2\varepsilon_d|$ achieves a maximum polarizability, leading to LSPR. Therefore, the resonant condition in the case of metal following Drude model and without considering damping of electron oscillation is

$$\varepsilon'(\omega) = -2\varepsilon_d \tag{1.9}$$

Using Eq. 1.4, it can be further expressed as

$$\omega_{LSPR} = \frac{\omega_p}{\sqrt{1+2\varepsilon_d}} \tag{1.10}$$

Similar to PSPR, the resonance frequency of LSPR is strongly dependent on the dielectric environment. For metal nanosphere in air ($\varepsilon_d = 1$), $\omega_{LSPR} = \omega_p/\sqrt{3}$.

The metal nanosphere efficiently scatters and absorbs light as a consequence of the resonantly enhanced polarization α. The corresponding scattering and absorption cross sections, σ_{Sca} and σ_{Abs}, respectively, are determined by

$$\sigma_{Sca} = \frac{k^4}{6\pi}|\alpha|^2 = \frac{8\pi}{3}k^4R^6\left|\frac{\varepsilon_m(\omega)-\varepsilon_d}{\varepsilon_m(\omega)+2\varepsilon_d}\right|^2 \tag{1.11}$$

$$\sigma_{Abs} = k\mathrm{Im}[\alpha] = 4\pi kR^3\mathrm{Im}\left[\frac{\varepsilon_m(\omega)-\varepsilon_d}{\varepsilon_m(\omega)+2\varepsilon_d}\right] \tag{1.12}$$

where $\mathrm{Im}[\alpha]$ is the imaginary part of α. Extinction cross section, the sum of absorption and scattering cross section, can be expressed as

$$\sigma_{Ext} = \sigma_{Sca} + \sigma_{Abs} \tag{1.13}$$

The above theory of scattering and absorption of the metal nanosphere based on the dipole approximation is strictly valid only for small particles ($R << \lambda$). In the case of larger nanospheres for which the approximation is not justified, however, a rigorous electrodynamic approach is required. In 1908, Mie proposed an exact theory in the case of nanospheres of any size.[29] For other shapes, similar approximation can be applied by introducing a shape factor.[30, 31] Many numerical methods, such as discrete dipole approximation (DDA), finite difference time domain (FDTD), and boundary element

method (BEM), have been developed to simulate the optical properties of plasmonic nanostructures.[32]

1.2.3 Characteristics of LSPR

LSPR has been of much interest due to its unique characteristics and wide applications. For example, plasmonic nanostructures exhibit very high extinction cross section, concentrate light in a nanoscale region close to their surfaces, and their LSPR properties can be tailored easily by changing size, shape, and composition of the nanostructure. Here the details of the characteristics are introduced.

(1) High extinction cross section

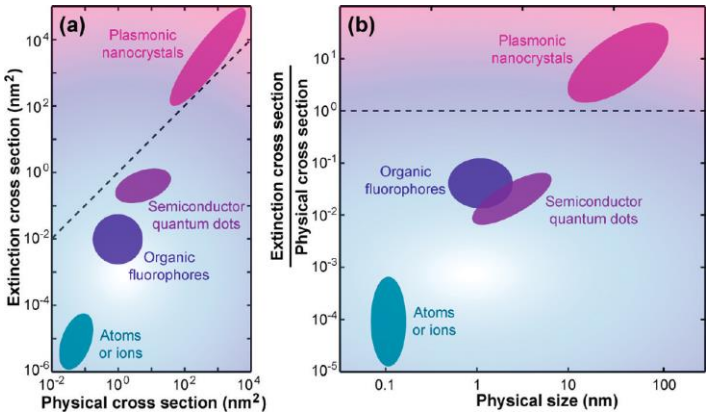

Figure 1.3 Comparison of the extinction cross sections of metal nanostructures and other optical species. (a) Plot of the extinction cross section to the physical cross section. (b) Plot of the ratio between the extinction cross section and physical cross section to the size of optical species. Reprinted with permission from ref. 33. Copyright 2012 American Chemical Society.

Extinction cross section, the sum of absorption and scattering cross sections (Eq. 1.13), is usually used to quantitatively characterize the interaction probability between light (photons) and electron oscillation in the plasmonic nanostructures. A higher extinction cross section suggests a higher interaction probability. Wang *et al.*[33] summarized the extinction cross sections of four types of nanoscale optical species: atoms/ions, organic fluorophores, semiconductor quantum dots, and plasmonic

nanocrystals (Figure 1.3). The physical cross section refers to total area of the orthographic projection of the optical species normal to the incident plane. It can be clearly seen from Figure 1.3 that plasmonic nanocrystals show much higher extinction cross section than that of other optical species. In addition, the ratio of the extinction cross section to the physical one for plasmonic nanocrystals is larger than 1, indicating light is confined to the nanocrystals.

(2) Localized electric field

As shown in Eq. 1.8, the large polarization is induced under the resonant condition, resulting in strong electric field localized aroun the metal nanoparticle (NP) compared with the excitation electric field. Figure 1.4[34] depicts FDTD simulated electric field distributions of Au nanoparticles (NPs) of various shapes (nanosphere, nanorod, and nanoplate) under light irradiation, demonstrating how strong the electric field localized around the Au NPs is. The Au nanorod and nanoplate exhibited much higher electric field intensity than the Au nanosphere. The local field enhancement factor is defined by $|E|^2/|E_0|^2$ where E is the localized electric field and E_0 is the incident one. Earlier studies showed that the enhancement depended on the curvature of the metal NP.[35] The sharper a metal NP is, the stronger local electric field becomes. A prime example is the Au bipyramid in which the enhancement factor at the tips is much larger than the Au nanorod.[36]

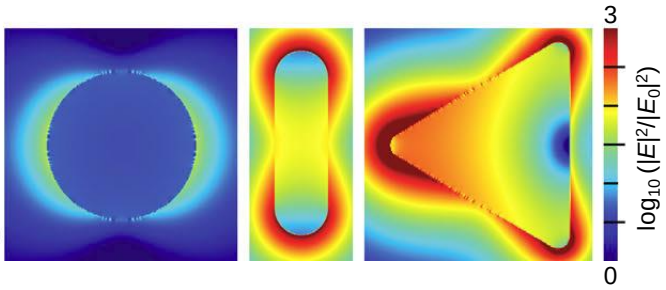

Figure 1.4 FDTD simulated electric field distributions of Au NPs with different shapes. Reprinted with permission from ref. 34. Copyright 2014 Wiley-VCH.

The localized electric field enhancement provides the basis for many applications such as surface enhanced Raman scattering (SERS)[5-7] and photocurrent enhancement.[8-

[13, 37-39] Raman scattering is based on inelastic light scattering upon vibrational excitation of molecules and an extremely inefficient process. The signal can be enhanced significantly when the molecules are placed near the surface of plasmonic NPs (Figure 1.5). This is partly because the localized and intensified electric field promotes the excitation of the molecules.[6]

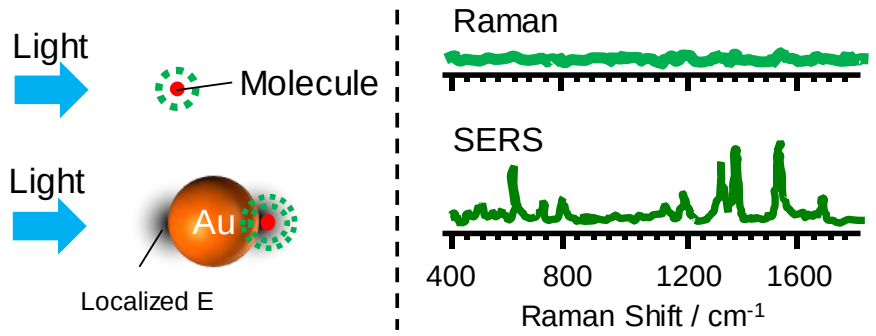

Figure 1.5 Schematic illustration for the mechanism of SERS.

Plasmonic NPs can work as nanoantennas to enhance the photocurrents of photoelectrodes or solar cells by increasing the light absorption. Figure 1.6a shows schematic illustration of an photoanode where the light absorbers such as dyes[37, 38] or quantum dots[39] are placed within the localized electric field through TiO_2 spacer. As

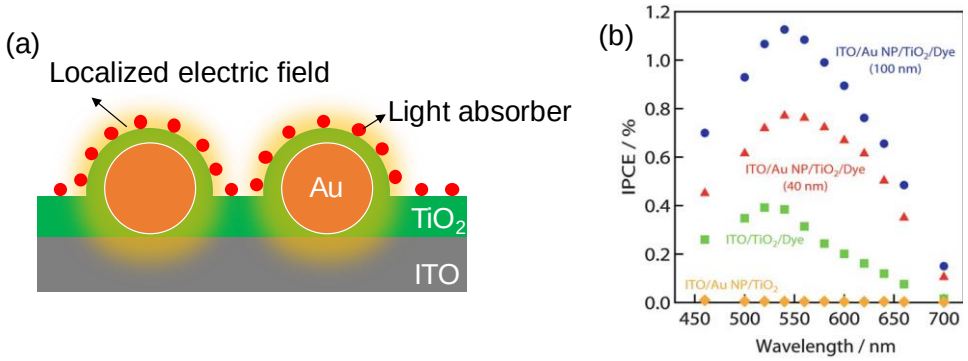

Figure 1.6 (a) Schematic illustration of a photoanode with Au NPs as nanoantennae. (b) Short-circuit photocurrent action spectra (shown by incident photon-to-current conversion efficiency, IPCE) of ITO/Au NP/TiO_2/dye photoelectrodes. Reprinted with permission from ref. 37. Copyright 2011 Royal Society of Chemistry.

shown in Figure 1.6b,[37] the dye-sensitized photocurrents are increased by 2 and 3 times by means of 40-nm and 100-nm Au NPs, respectively. This strategy has been also applied widely to various types of solar cells such as dye-sensitized solar cells,[8-10] organic photovoltaics,[11] and perovskite solar cells[13] for improvement of photocurrents and thereby power conversion efficiency (PCE).

(3) Tunable optical properties

As discussed in section 1.2.2, the LSPR wavelength can be controlled by the dielectric constant of the surrounding medium according to Eq. 1.10. In addition, the optical properties of NPs derived from LSPR can also be tuned by their size, shape and chemical composition.

Size of NP

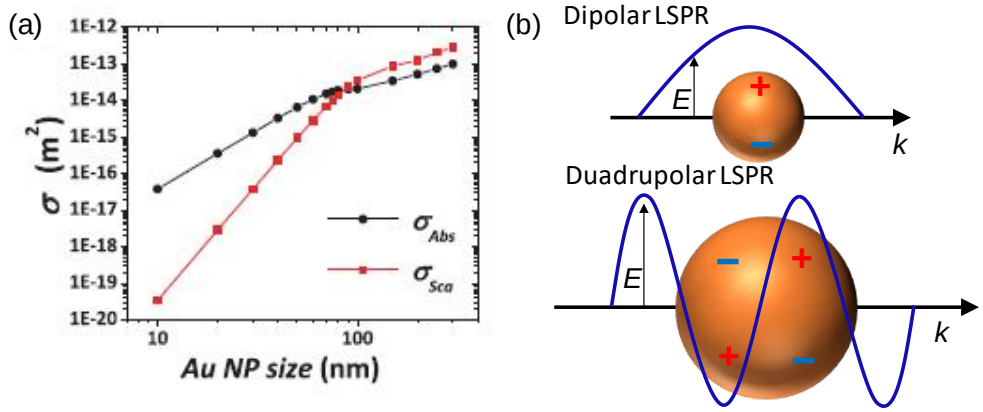

Figure 1.7 (a) Calculated maximum absorption and scattering cross sections for Au NPs with different sizes dispersed in water. Reprinted with permission from ref. 40. Copyright 2013 American Chemical Society. (b) Schematic illustration of dipolar and quadrupolar LSPR of plasmonic NPs.

The size of NP has important effects on scattering and absorption cross sections. As shown in Figure 1.7a, the absorption dominates over scattering for smaller NPs, whereas the scattering prevails when the size becomes larger.[40] This can be explained partially by Eq. 1.11 and 1.12. Furthermore, the size of NP also affects the resonant wavelength and full width at half maximum (FWHM) of the spectrum. Dipolar mode

is excited when the size of NPs is much smaller than the wavelength of incident light (Figure 1.7a), while multipolar modes contribute to absorption and scattering of NPs the size of which is comparable to or larger than the incident wavelength (Figure 1.7b), resulting in the broadening and redshift of extinction peak.[40]

Shape of NP

Peak wavelength, shape, and FWHM of the spectrum are highly dependent on the shape of NPs. Isotropic Au nanospheres show a LSPR peak (Figure 1.8a),[40] whereas anisotropic Au nanorods exhibit two peaks (Figure 1.8c) which are attributed to two different LSPR modes, transverse and longitudinal ones (Figure 1.8b).[41] The absorption cross section of transverse mode is relatively low and almost independent of the aspect ratio (ratio of the length to the width of the nanorod), while the longitudinal peak is much more intense and strongly dependent on the aspect ratio. Other anisotropic NPs, such as Au nanoplates,[42] nanotubes,[43] and nanostars[44] were also prepared and their optical properties were investigated.

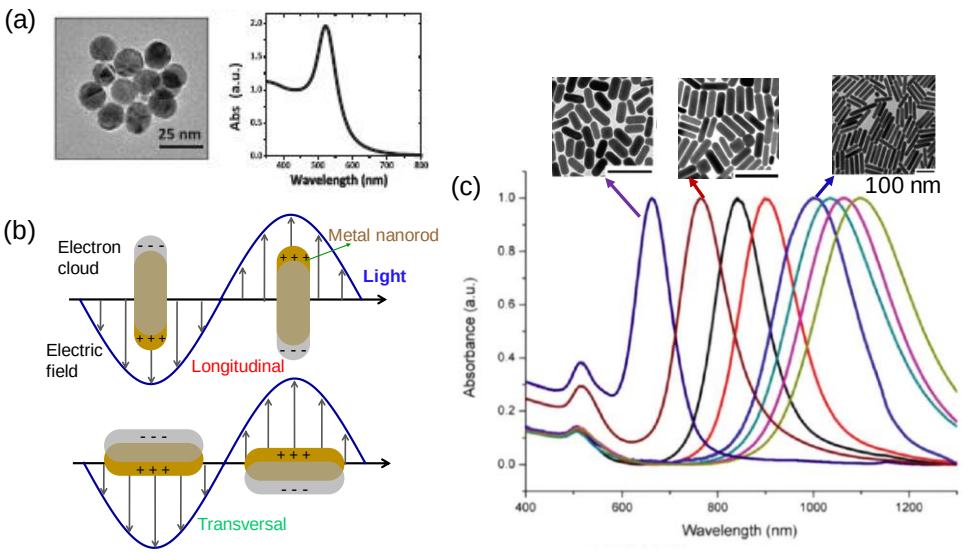

Figure 1.8 (a) TEM image and absorption spectrum of Au nanospheres. Reprinted with permission from ref. 40. Copyright 2013 American Chemical Society. (b) Schematic illustrations of longitudinal and transverse modes of Au nanorods. (c) SEM images and absorption spectra of Au nanorods with various aspect ratios. Reprinted with permission from ref. 41. Copyright 2015 Ivyspring International Publisher.

Chemical composition of NP

Plasmonic properties of metal NPs are associated strongly with the dielectric function of the metal. Therefore, plasmonic NPs composed of different metals (Au, Ag, and Cu) show different optical properties.[14] Metal alloying is one of the ways to tune the optical responses of plasmonic NPs. As can be seen from Figure 1.9, the LSPR wavelength of Au–Ag alloy NPs shows linear dependence on the alloy composition.[45]

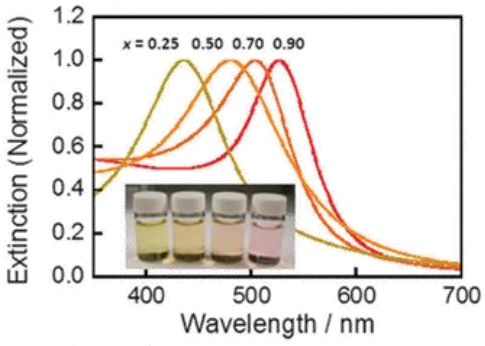

Figure 1.9 Extinction spectra of aqueous solutions of Au–Ag alloy NPs. Inset is the corresponding photographs of the solution. Reprinted with permission from ref. 45. Copyright 2015 Royal Society of Chemistry.

1.2.4 Relaxation Processes of LSPR

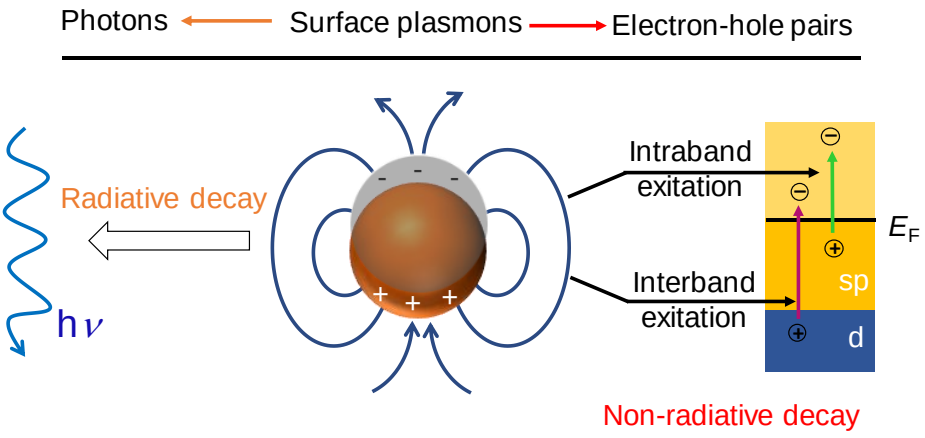

Figure 1.10 Schematic representation of radiative decay and non-radiative decay of LSPR.

The surface plasmons have a certain lifetime. They decay through two ways: radiative and non-radiative decay (Figure 1.10). The radiative decay takes place via

emission of photons, which is the scattered light in the far-field. The surface plasmons also decay non-radiatively by producing electron-hole pairs through intraband excitation (within the sp-band) and interband excitation (from the d-band to the sp-band).

1.3 Fabrication and LSPR of Periodic Metal Nanostructures

In general, substrates with plasmonic metal nanostructures are easily prepared by photocatalytic reduction, electrodeposition, thermal dewetting, and wet chemistry combined with electrostatic attraction. However, the obtained substrates are composed of disordered metal NP assemblies. For these substrates, it is difficult to precisely control some important factors, such as NP shape, size, interparticle distance described above, which can determine wavelength, shape, FWHM, and number of LSPR peak. Instead, periodic metal nanostructures immobilized on substrates are characterized by good controllability and reproducibility. Some techniques like focused-ion-beam milling (FIB), photolithography, electron beam lithography (EBL), and nanosphere lithography (NSL) are used for fabrication of metal arrays. Among them, EBL and NSL are briefly introduced in the following.

1.3.1 Electron Beam Lithography (EBL)

Figure 1.11 illustrates fabrication process of periodic metal array by electron beam lithography (EBL): spin-coating with a e-beam resist layer, exposure to e-beam, metal

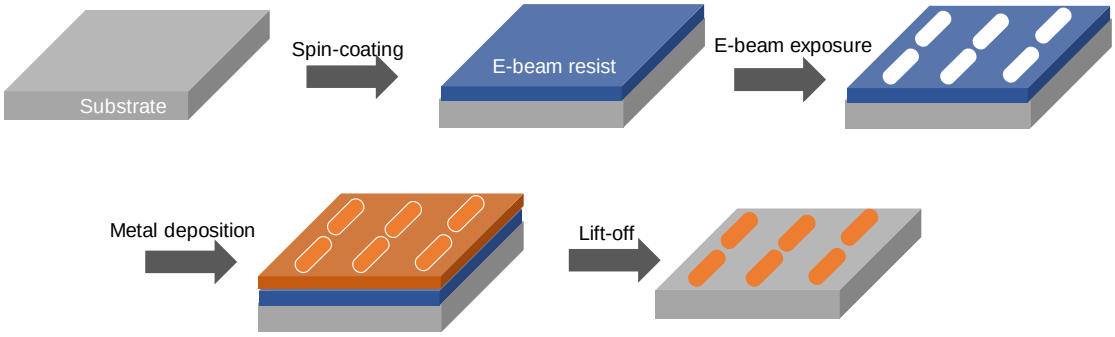

Figure 1.11 Schematic illustration for fabrication of periodic metal array by EBL.

deposition by evaporation or sputtering, and lift-off. EBL allows the successful fabrication of metal nanostructures with various geometrical shapes and different periodic arrangements.[46, 47] Two major advantages of EBL are its ability to accurate control small areas of a substrate and low defect densities.[48] The principle drawbacks of EBL are low throughput and high cost.[48]

1.3.2 Nanosphere Lithography (NSL)

Nanosphere lithography (NSL) is now recognized as an inexpensive and high-throughput nanomaterial fabrication technique capable of producing well-ordered NP arrays.[49] A self-assembled colloidal crystal is used as a mask in the NSL process, as shown in Figure 1.12. When the colloidal nanospheres are removed, the metal deposited between them remains on the substrate, resulting in formation of a triangular metal array. And then, it extends to double layer NSL and angle-resolved NSL by Van Duyne *et al*.[49, 50] The simple NSL can be used to prepare NPs which exhibited LSPR peaks over a wide range of wavelengths.[49] However, a certain amount of defects exist in the resulted metal array prepared by NSL, which arises from the imperfect colloidal crystal.

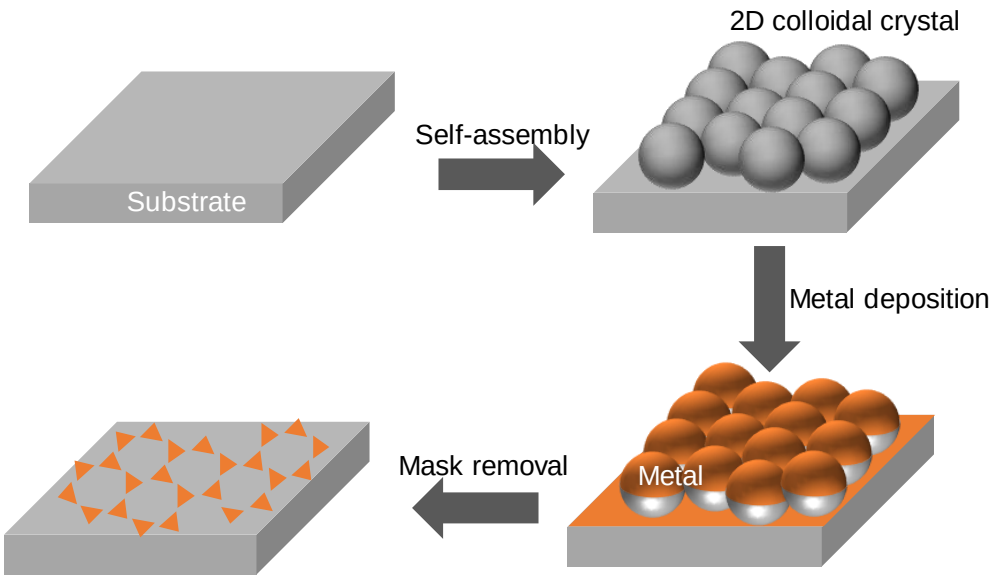

Figure 1.12 Schematic illustration for fabrication of metal array by NSL.

1.4 Plasmon-Induced Charge Separation (PICS)

1.4.1 Metal-Semiconductor Contact[51, 52]

Work function (W) is one of the important parameters to determine electronic structure of metals and semiconductors. The relationship of work function and Fermi level (E_F) is decided by

$$W = E_0 - E_F \tag{1.14}$$

where E_0 is vacuum energy. When a metal is in contact with a semiconductor, electron transfer occurs between them due to the difference of work function. Figure 1.13 shows energy band diagrams at the interface between a metal and an n-type semiconductor. When the semiconductor work function (W_s) is lower than that of the metal (W_m) (Figure 1.13a), the electrons flow from the semiconductor to the metal until their Fermi levels are aligned. The surface region of semiconductor is positively charged, while the metal is negatively charged, resulting in formation of build-in electric filed at their interface. The positive charges in the semiconductor are distributed in a micrometer order width from the interface which is called charge space layer. Because the electrons are depleted in the space charge region, it is named as the depletion layer. In the depletion layer, the energy bands bend upward toward the interface due to the build-in electric filed. The degree of band bending (E_{BB}) is determined by

$$E_{BB} = W_m - W_s \tag{1.15}$$

An energy barrier, called Schottky barrier, is formed at the metal-semiconductor interface. The height of the Schottky barrier (E_{SB}) can be calculated by

$$E_{SB} = W_m - \chi_s \tag{1.16}$$

where χ_s is the electron affinity of the semiconductor.

When $W_s > W_m$, the electrons transfer from the metal to the semiconductor until their Fermi levels become equal (Figure 1.13b). In this case, the electrons are accumulated in the space charge layer. Thus, this region is called the accumulation layer. The energy bands bend downward toward the metal-semiconductor interface and no energy barrier exists.

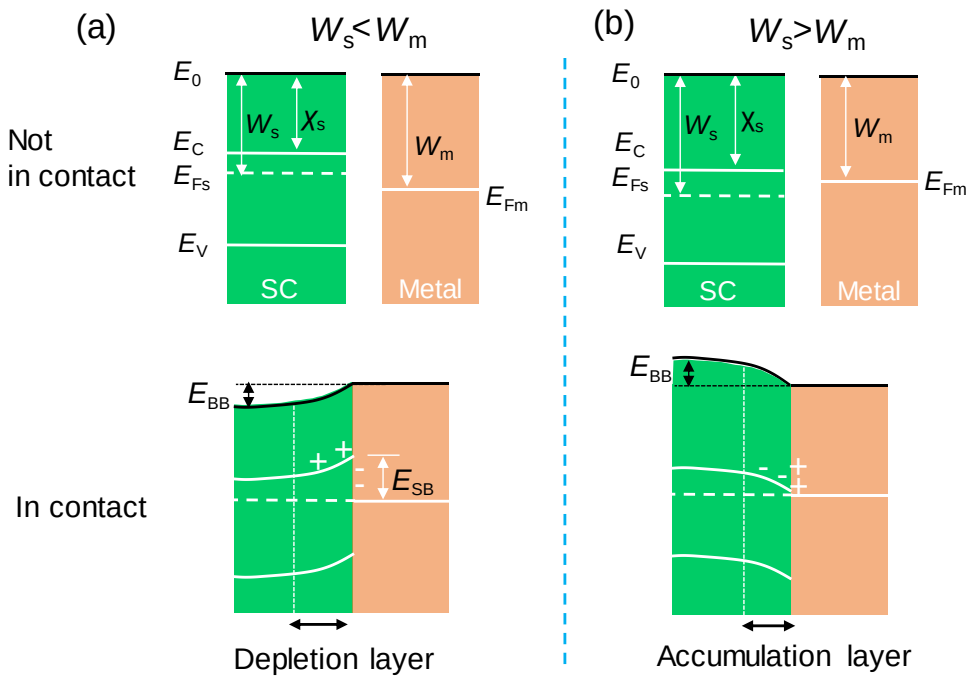

Figure 1.13 Energy band diagrams of metal and n-type semiconductor contacts in the case of (a) $W_s < W_m$ and (b) $W_s > W_m$. SC: semiconductor; E_0: vacuum energy; E_c: energy of conduction band minimum; E_v: energy of valence band maximum; E_{Fs}: Fermi level of the semiconductor; E_{Fm}: Fermi level of the metal; W_s: work function of the semiconductor; W_m: work function of the metal; χ_s: electron affinity of the semiconductor; E_{SB}: Schottky barrier; E_{BB}: degree of band bending.

1.4.2 Discovery and Evidences of PICS

In 2004, Tatsuma *et al.* found plasmon-induced charge separation (PICS) at the interface between TiO_2 and Au nanosphere.[23] Figure 1.14a shows a schematic illustration of PICS. PICS is an energetically uphill charge transfer process exited by the visible or NIR light at LSPR wavelength. Electrons transfer from a plasmonic metal NP (typically Au NP) to the conduction band of a semiconductor (typically TiO_2). The charge separation was first demonstrated by detectable negative open-circuit potential change (Figure 1.14b) and anodic short-circuit photocurrent (Figure1.14c) when a Au NP/TiO_2/ITO electrode was used as the working electrode in wet electrochemical cells. Under open-circuit conditions, the transferred electrons are accumulated in the TiO_2, leading to a negative potential shift of the electrode. Under short-circuit conditions, the separated holes in the metal NP can be used for oxidation of electron donors in the

electrolyte, while the electrons in the TiO_2 are transported to the counter electrode for reduction of electron acceptors, resulting in an anodic photocurrent. It should be noted that the peaks of the action spectra are in good accordance with those of the absorption spectra, indicating that the photoresponses are derived from LSPR of the Au NP.

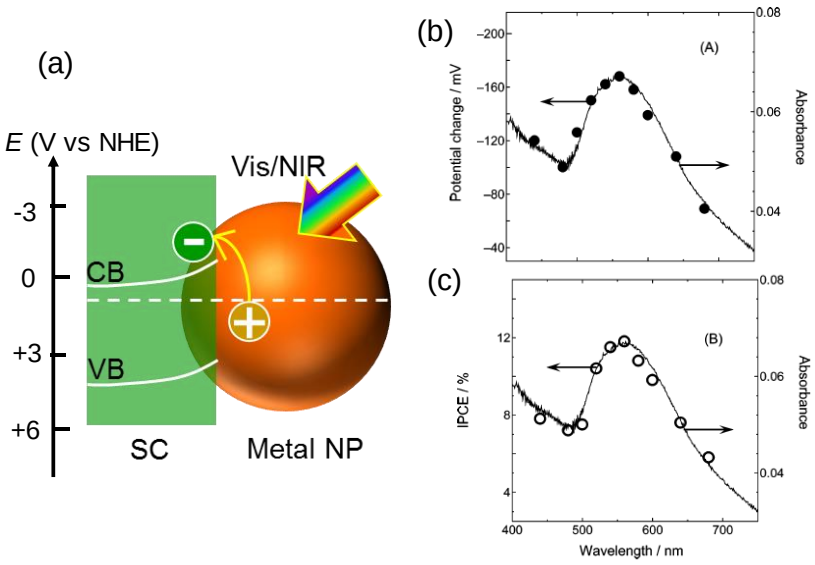

Figure 1.14 (a) Schematic Illustration for plasmon-induced charge separation (PICS). (b) Open-circuit photopotential action spectrum in a conventional three-electrode electrochemical cell and (c) short-circuit photocurrent action spectrum (IPCE spectrum) in a two-electrode sandwich cell with a Au NP/TiO_2/ITO electrode. Electrolyte contains 0.1 M $FeCl_2$ and 0.05 M $FeCl_3$. Reprinted with permission from ref. 23. Copyright 2005 American Chemical Society.

PICS process shown in Figure 1.14a is further supported by the results that cathodic photocurrents and positive photopotentials are observed by using ITO/Au NP/TiO_2 electrodes in an electrochemical cell.[53] If the electron transfer from the Au NP to the TiO_2 takes place, polarity of the photocurrent and the photopotential should be reversed when the Au NP/TiO_2 bilayer is inverted (Figure 1.15a and b).[53] PICS is also verified by in-situ nanoimaging of surface potential changes on Au nanoplate/TiO_2 under illumination of NIR light by the aid of Kelvin probe force microscopy (KFM).[54] Positive shift of the surface potential of Au nanoplate was observed upon NIR light irradiation (Figure 1.15c), suggesting electron injection from the exited Au NPs to TiO_2.

In the case of UV-induced photocatalysis process in which the TiO_2 is excited by UV light, however, opposite potential shift was observed (Figure 1.15c). This study gives us a direct and visual evidence for the PICS.

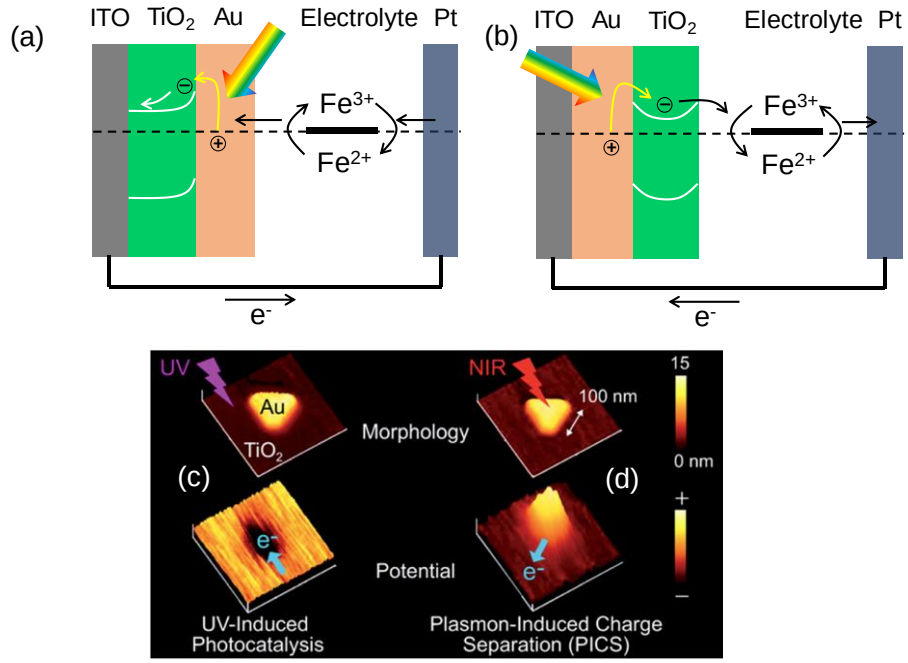

Figure 1.15 Schematic representations of (a) the photoelectrochemical cell with ITO/TiO_2/Au NP electrode and (b) that with ITO/Au NP/TiO_2 electrode. Results of KFM analysis for the Au nanoplate/TiO_2 electrode under (c) UV and (d) NIR light irradiation. Reprinted with permission from ref. 54. Copyright 2014 Wiley-VCH.

1.4.3 Mechanism of PICS

There are three mechanisms that contribute to the charge transfer from the exited metal to a semiconductor: the interfacial photoelectric effect (Figure 1.16a), the distal photoelectric effect (Figure 1.16b), and the photoinduced interfacial electron transition (Figure 1.16c).

PICS based on the interfacial and distal photoelectric effects includes hot electron generation within the metal (Figure 1.10), followed by electron transfer to the contacted semiconductor. The PICS efficiency is related to the lifetime and energy of the excited electrons. In the case of photoelectric effects, the excited electrons relax through

various ways such as electron-electron scattering before they diffuse to the metal-semiconductor interface. In addition, the energies of the excited electrons are distributed in a wide range[55] and most of the fractions do not have enough energy to overcome the Schottky barrier. These electrons cannot contribute to the charge separation but are converted to heat. Due to the above factors, the efficiency of PICS is very low in the most cases.

It is reported that PICS can also be realized by the photoinduced interfacial electron transition: electrons are excited directly from the metal to the semiconductor conduction band. In this case, strong interactions between the metal and semiconductor result in a new pathway for uphill electron transfer. This mechanism was experimentally confirmed in CdSe-Au nanorod heterostructures.[56] The highly efficient charge separation with >24% quantum efficiencies was observed by excitation of the Au tip.

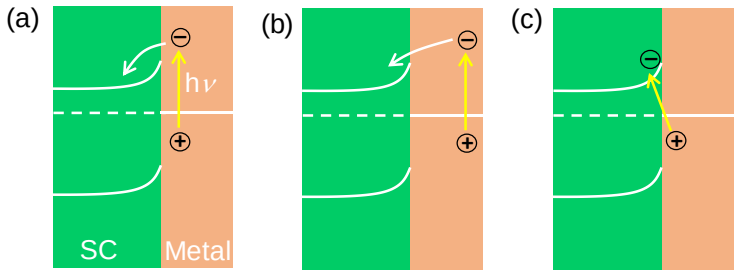

Figure 1.16 Schematic illustrations for (a) PICS based on the interfacial photoelectric effect, (b) PICS based on the distal photoelectric effect, and (c) PICS based on the photoinduced interfacial electron transition.

1.4.4 Roles of Localized Electric Field

Some researchers focused on relationship between PICS and localized electric field generated by LSPR. Selective dissolution of Ag NPs deposited on TiO_2 is one of the prominent approaches to investigate the relationship. PICS drives the electron transfer from the resonant Ag NP to the TiO_2 and oxidative dissolution of Ag to Ag^+ ions, indicating that reaction site of PICS can be determined from the morphology

change of the NP. As shown in Figure 1.17a,[57-59] PICS-based anodic reaction proceeds preferentially at the bottom part of the Ag nanosphere upon excitation of plamonic interface mode in which electric field is localized at the interface between the nanosphere and TiO_2. When the electric field is distributed over the nanosphere surface (full-surface mode), selective dissolution does not proceed. Similar results were observed in the cases of Ag nanorods and nanocubes loaded on TiO_2. Excitation of the transverse and longitudinal modes induces the corresponding site-selective dissolution (Figure 1.17b). Distal and proximal modes for Ag nanocubes also contribute to the site selective dissolution (Figure 1.17c).

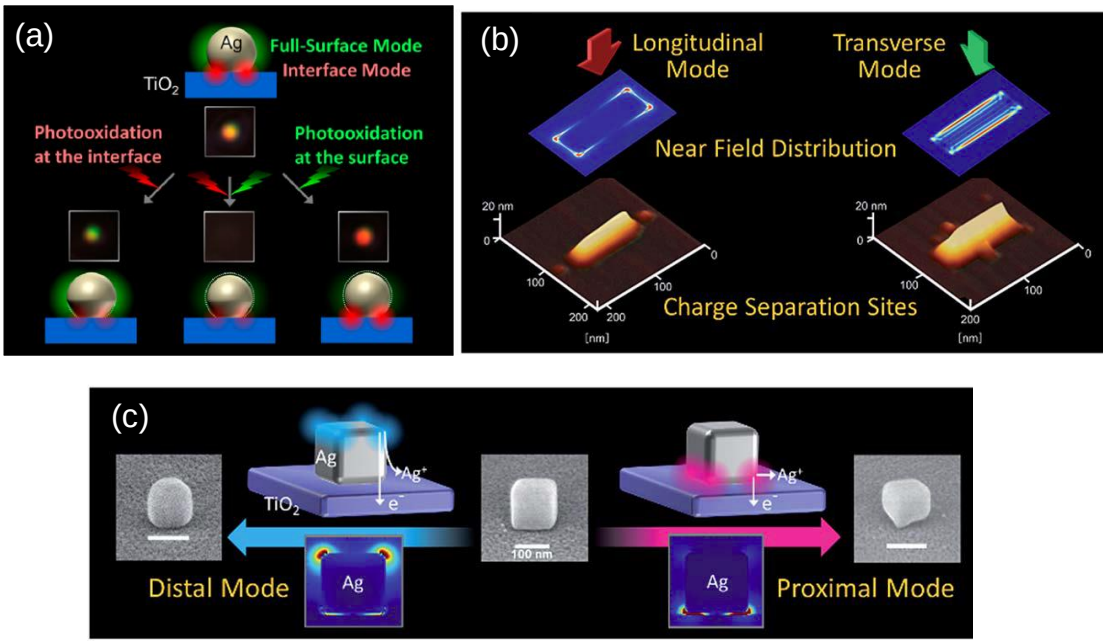

Figure 1.17 Results on investigation of PICS reaction site for (a) Ag nanospheres on TiO_2. Reprinted with permission from ref. 57. Copyright 2012 American Chemical Society. Results for (b) Ag nanorods on TiO_2 and (c) Ag nanocubes on TiO_2. Reprinted with permission from ref. 61. Copyright 2017 Royal Society of Chemistry.

The site selective dissolution is explained partly by the fact that the strong electric field localized around the plasmonic nanostructure is advantageous for the generation of hot carriers.[60] Therefore, Au nanostars/TiO_2 showed higher catalytic efficiency toward the degradation of a pollutant than Au nanospheres or nanorods deposited on

TiO_2.[60] In other words, it is important to pay attention to the nanostructure with sharp edge which tends to exhibit strong localized electric field as mentioned in Section 1.2.3.

1.4.5 Application of PICS

PICS has been widely applied to photocatalysis,[14-23] photovoltaics and photodetection,[55,62-71] chemical and biological sensors,[3,4] and photochromism,[58,72,73]. Here, their applications to photocatalysis and photovoltaics which are related to the studies in this thesis are reviewed.

(1) Photocatalysis

As shown in Figure 1.18, the electrons and holes provided by PICS drive reduction and oxidation reactions, respectively. For instance, decomposition of organics (*e.g.* aldehydes, alcohols, and dyes),[14,16,17,23] oxidation of water to O_2[15,20], reduction of water to H_2[17,19,20], and water splitting[18,21] are feasible under visible and NIR light irradiation. The PICS-induced photocatalytic reactions offer a promising strategy to overcome the absorption limitation of the semiconductor. Photoresponse of the PICS-based catalysts can be tuned easily by using various plasmonic nanostructures as described in Section 1.2.3 and 1.3.

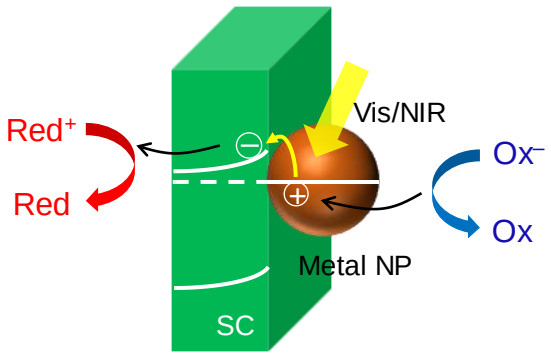

Figure 1.18 Schematic illustration for the anodic and cathodic reactions caused by PICS.

Degradation of organics is often used for evaluation of the photocatalytic activity. Moshfegh *et al.* reported photocatalytic activity of a TiO_2 films with different metallic NPs (Au, Ag, and Cu). It was found that TiO_2 films with Au and Cu NPs provided a

higher catalytic performance for degradation of methylene blue (MB) under visible irradiation.[14] The structural and electronic properties of TiO_2 should also be essential for achieving excellent photocatalytic performance. It is revealed that the Au NPs on TiO_2 with dominantly exposed {0 0 1} facets exhibited superior photocatalytic activity towards degradation of rhodamine B (RhB) compared with Au NPs deposited on commercial P25 (Figure 1.19a).[16] Moreover, Au NPs on mesocrystal TiO_2 showed much better photocatalytic activity than those on conventional P25 (Figure 1.19b).[17] This is explained by the anisotropic electron flow which significantly retards the recombination of electron and hole (Figure 1.19b).

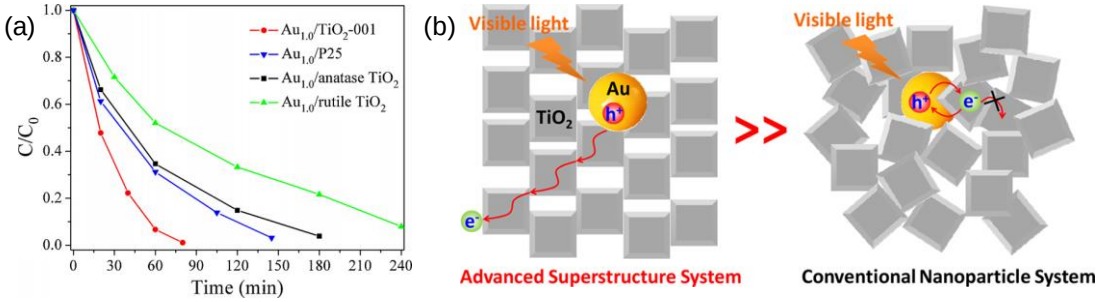

Figure 1.19 (a) Photocatalytic performance of the Au-TiO_2 photocatalysts with different TiO_2 supports.[16] Reprinted with permission from ref. 61. Copyright 2017 Royal Society of Chemistry. (b) Illustration for the comparison of Au NPs on mesocrystal TiO_2 and conventional TiO_2. Reprinted with permission from ref. 17. Copyright 2014 American Chemical Society.

Photocatalytic water splitting has received growing attention since the first report of Honda-Fujishima effect of TiO_2 in 1972[74] because H_2 is a clean and alternative fuel.[75] PICS enables us to realize water splitting under visible and NIR light. To date, a large number of Au/TiO_2 catalysts with various nanostructures have been reported one after another. For example, Moskovits *et al.* demonstrated water splitting by a plasmonic photocatalyst consisting of TiO_2 coated Au nanorods and Pt and Co-based cocatalyts (latter one is denoted as Co-OEC) (Figure 1.20).[18] Cocatalysts are generally incorporated into the plasmonic photocatalyst systems because they have important roles in enhancing the chare separation efficiency and provide many active sites for

surface reactions.[22] In addition to TiO_2, other semiconductors such as ZnO,[21] WO_3,[20] CdS,[19] and CeO_2,[15] were also used for the plasmonic photocatalysts.

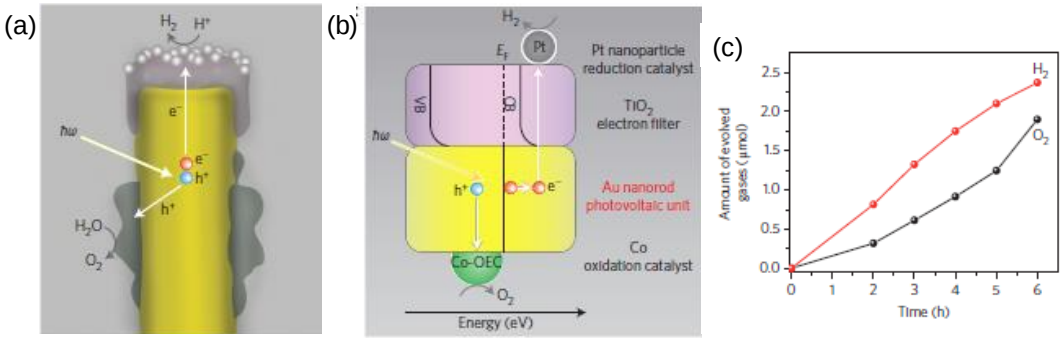

Figure 1.20 (a) Schematic illustration and (b) energy level diagram for an individual unit of plasmonic water splitter. (c) Measured O_2 and H_2 as a function of time illuminated by white light (AM 1.5). Reprinted with permission from ref. 18. Copyright 2013 Nature Publishing Group.

(2) Photovoltaics

The first reported PICS photovoltaic device was a wet cell in which plasmonic Au works as a light absorber. The photograph and structure of the cell are shown in Figure 1.21a and b.[23] However, wet cells have several drawbacks such as low stability, leakage, and electrolyte evaporation. To overcome these issues, solid-state devices with various plasmonic nanostructures were designed. The performances of the solid-state PICS cells are summarized in Table 1.1. The cell with the structure of ITO/TiO_2/PL/HTL/Au (PL = plasmonic material and HTL = hole transport layer) was developed first (Figure 1.21b). However, its efficiency was very low: the IPCE at 560 nm was only 0.0024%. Cells with a simpler structure, In/TiO_2/PL/ITO, were then developed (Figure 1.21c). A device showed a good response in the visible to NIR range, leading to IPCE at 450 nm and power conversion efficiency (PCE) of 0.6% and 0.016%, respectively.

Table 1.1 Performances of PICS-based solid-state photovoltaic cells.

Year	Cell	PL	IPCE (%)	PCE (%)	Ref
2008	ITO/TiO_2/PL/HTL/Au	Au NS	0.0024	—	62
2011	In/TiO_2/PL/ITO	Au NS	0.4	0.016 (>400 nm)	64
		Ag NS	0.6	—	
2012	FTO/TiO_2/PL/HTL/Au	Au NS	0.93	—	65
		Ag NS	0.46	—	
2013	FTO/TiO_2/Al_2O_3/PL	Au NS	1.2	—	66
		Ag NS	3.8	0.03 (AM1.5)	
2014	Ti/TiO_2/PL/ITO	Au NR	1.0	0.002 (AM1.5)	68
2016	Cu/InGa/TiO_2/PL/NiO/Au	Au NS	0.1	0.033 (AM1.5) ~0.01 (>410 nm)	70
2016	FTO/TiO_2/PL/HTL/Au	Au NS	2.1	—	71

Abbreviations: ITO = indium tin oxide; FTO = fluorine-doped tin oxide; NS = nanosphere; NR = nanorod; HTL = hole transport layer.

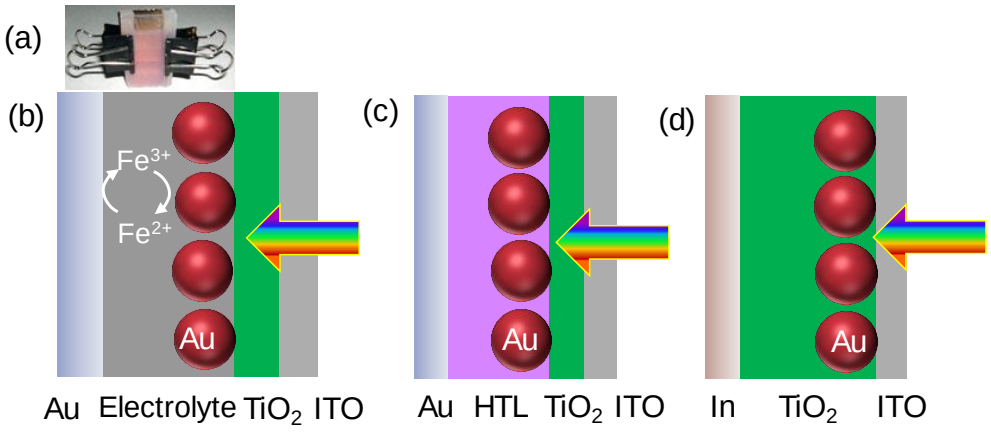

Figure 1.21 (a) Photograph and (b) structure of a PICS wet-type photovoltaic cell. PICS solid-state cells with the structures of (c) ITO/TiO_2/PL/HTL/Au and (d) In/TiO_2/PL/ITO.

PICS efficiency was further improved in the past few years. The solid-state cells with the structure of FTO/TiO_2/Al_2O_3/PL were reported (Figure 1.22a).[66] The external quantum efficiency (EQE, also called IPCE) of 3.8% at 460 nm for FTO/TiO_2/Ag (Figure 1.22b) and that of 1.2% at 550 nm for FTO/TiO_2/Au were achieved. However, the cell cannot generate a measurable photovoltage in the absence of the Al_2O_3 layer, suggesting that the insulator layer plays a critical role in interface passivation. The device with Al_2O_3 achieved high open-circuit voltage (V_{oc}) of 0.5 V (Figure 1.22d), whereas the insulator reduced short-circuit photocurrent (J_{sc}) simultaneously (Figure 1.22c). The maximum PCE was 0.03% for the cell with Al_2O_3 of 0.5 nm (Figure 1.22e). Metal nanorods were also used as the plasmonic material in a solid-state cell. The device with the structure of Ti/TiO_2/PL/ITO showed a maximum PCE of 0.002%.[68]

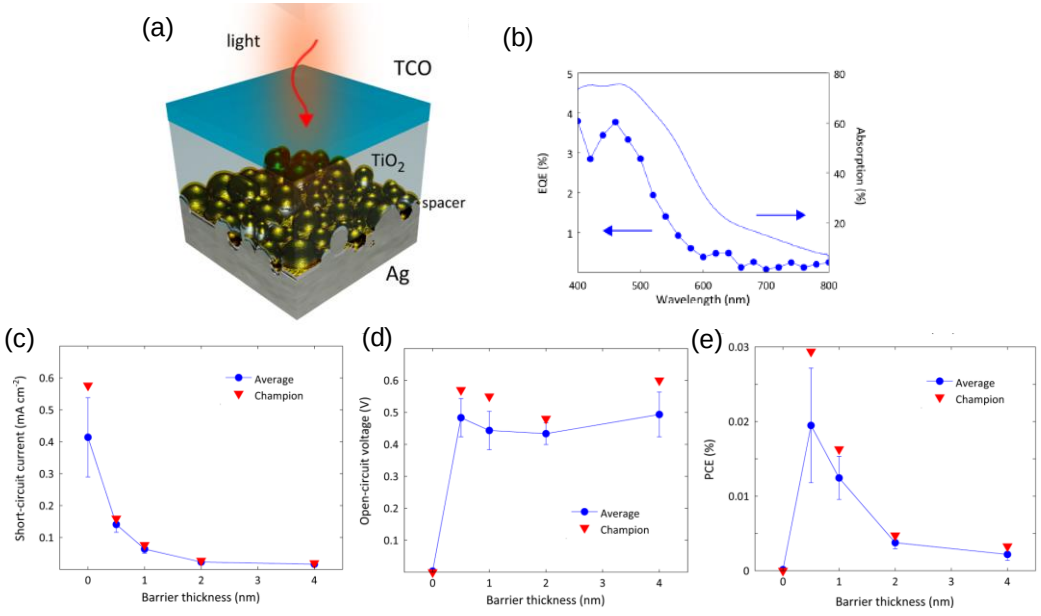

Figure 1.22 (a) Schematic illustration of the PICS solid-state cell with structure of FTO/TiO_2/Al_2O_3/PL. (b) External quantum efficiency (EQE) and absorption of the cell without a spacer (FTO/TiO_2/PL). (c) Short-circuit current, (d) open-circuit voltage, and (d) power conversion efficiency (PCE) of the cell (FTO/TiO_2/Al_2O_3/PL) with different thicknesses of A_2lO_3 under light irradiation (AM1.5). Reprinted with permission from ref. 66. Copyright 2013 American Chemical Society.

1.5 Scope of This Thesis

In the studies of PICS, disordered and dispersed metal NPs deposited on TiO_2 have been used in most cases. However, it is difficult to precisely control important factors, such as NP shape, size, interparticle distance, and other factors described above, which determine PICS behavior of metal nanostructures. Although there are a few reports on plasmonic systems with ordered metal NPs, electron beam lithography (EBL), an expensive and time-consuming and high cost method, is often used for the preparation.[76] Therefore, it is important to turn our attention to more sophisticated and easily prepared plasmonic nanomaterials and their PICS properties.

Objectives of this thesis are fabrication of a novel well-defined plasmonic nanostructures and investigation of their PICS properties. A simple and low-cost colloidal template technique is exploited to prepare the ordered plasmonic nanostructures. First, periodic two-dimensional (2D) metal halfshell arrays can be prepared by evaporating metal onto self-assembled SiO_2@TiO_2 colloidal crystals. In this periodic photoelectrode, thickness and size of metal halfshell can be exactly controlled by the time of thermal evaporation and the size of SiO_2 core, respectively. Therefore, the controllability of the photoelectrode should be very high. In addition, the interconnected metal halfshell nanostructure may serve both as a light absorber and a current collector (counter electrode), allowing us to simplify the structure of solid-state photovoltaic cell. High photostability is also expected because the continuous nanostructure has lower surface-to-volume ratio than that of dispersed NPs. And then, other periodic plasmonic photoelectrodes with Au nanodisks and nanoholes are also prepared by evaporating metal onto TiO_2 nanohole arrays.

This doctoral thesis consists of five chapters. Chapter 1 reviews the fundamental physics and applications of SPR and the related PICS.

In chapter 2, the plasmonic photoelectrodes with an ordered and continuous Au semishell or halfshell structure are developed by sputtering or evaporating Au onto self-assembled SiO_2@TiO_2 core-shell colloidal crystals. The morphologies, optical properties, and photoresponses of the prepared electrodes are investigated. The effects

of SiO_2 core size is also examined. Finite-difference time-domain (FDTD) calculation is carried out to simulate the optical properties and electric field distribution of Au halfshell arrays.

Chapter 3 deals with development of PICS solid-state photovoltaic cells based on the metal halfshell arrays. The cells are designed by taking advantage of the interconnected Au halfshell array which serves both as a light absorber and a current collector (counter electrode). Effects of the thickness of TiO_2 shell and hole transport layer (MoO_3 and Spiro-OMeTAD) are discussed. Finally, the photovoltaic properties of the cells with Au, Ag, and Cu halfshell arrays are compared.

Chapter 4 describes fabrication of plasmonic photoelectrodes with Au nanoholes and Au nanoplates. Optical responses to refractive index change and photoelectrochemical properties of the obtained electrodes are investigated. FDTD simulation is also performed for calculation of the optical spectra and electric field distributions.

Chapter 5 makes a conclusion about this thesis.

1.6 References

1. H. Lee, Y. Xiong, N. Fang, W. Srituravanich, S. Durant, M. Ambati, C. Sun, and X. Zhang, *New J. Phys.*, 2005, **7**, 255.
2. R. Yang, M. A. Abushagur, and Z. Lu, *Opt. Express*, 2008, **16**, 20142-20148.
3. P. Da, W. Li, X. Lin, Y. Wang, J. Tang, and G. Zheng, *Anal. Chem.*, 2014, **86**, 6633-6639.
4. T. Tatsuma, Y. Katagi, S. Watanabe, K. Akiyoshi, T. Kawawaki, H. Nishi, and E. Kazuma, *Chem. Commun.*, 2015, **51**, 6100-6103.
5. N. R. Jana and T. Pal, *Adv. Mater.*, 2007, **19**, 1761-1765.
6. N. C. Lindquist, P. Nagpal, K. M. McPeak, D. J. Norris, and S. H. Oh, *Rep. Prog. Phys.*, 2012, **75**, 036501.
7. J. Reguera, J. Langer, D. J. de Aberasturi, and L. M. Liz-Marzán, *Chem. Soc. Rev.*, 2017, **46**, 3866-3885.
8. M. Ihara, M. Kanno, and S. Inoue, *Physica E*, 2010, **42**, 2867-2871.
9. C. Nahm, H. Choi, J. Kim, D. R. Jung, C. Kim, J. Moon, B. Lee, and B. Park, *Appl. Phys. Lett.*, 2011, **99**, 253107.
10. Y. Li, H. Wang, Q. Feng, G. Zhou, and Z. S. Wang, *Energy Environ. Sci.*, 2013, **6**, 2156-2165.
11. P. Du, P. Jing, D. Li, Y. Cao, Z. Liu, and Z. Sun, *Small*, 2015, **11**, 2454-2462.

12. Y. H. Jang, Y. J. Jang, S. Kim, L. N. Quan, K. Chung, and D. H. Kim, *Chem. Rev.*, 2016, **116**, 14982-15034.
13. G. M. Kim and T. Tatsuma, *J. Phys. Chem. C*, 2017, **121**, 11693-11699.
14. P. Sangpour, F. Hashemi, and A. Z. Moshfegh, *J. Phys. Chem. C*, 2010, **114**, 13955-13961.
15. A. Primo, T. Marino, A. Corma, R. Molinari, and H. Garcia, *J. Am. Chem. Soc.*, 2011, **133**, 6930-6933.
16. S. Zhu, S. Liang, Q. Gu, L. Xie, J. Wang, Z. Ding, and P. Liu, *Appl. Catal. B*, 2012, **119**, 146-155.
17. Z. Bian, T. Tachikawa, P. Zhang, M. Fujitsuka, and T. Majima, *J. Am. Chem. Soc.*, 2013, **136**, 458-465.
18. S. Mubeen, J. Lee, N. Singh, S. Krämer, G. D. Stucky, and M. Moskovits, *Nat. nanotechnol.*, 2013, **8**, 247-251.
19. X. Ma, K. Zhao, H. Tang, Y. Chen, C. Lu, W. Liu, Y. Gao, H. Zhao, and Z. Tang, *Small*, 2014, **10**, 4664-4670.
20. A. Tanaka, K. Hashimoto, and H. Kominami, *J. Am. Chem. Soc.*, 2014, **136**, 586-589.
21. X. Zhang, Y. Liu, and Z. Kang, *ACS Appl. Mater. Interfaces*, 2014, **6**, 4480-4489.
22. L. Liu, X. Zhang, L. Yang, L. Ren, D. Wang, and J. Ye, *Natl. Sci. Rev.*, 2017, doi: 10.1093/nsr/nwx019.
23. Y. Tian and T. Tatsuma, *J. Am. Chem. Soc.*, 2005, **127**, 7632-7637.
24. S. A. Maier, *Plasmonics: fundamentals and applications*, Springer Science & Business Media, 2007.
25. G. V. Hartland, *Chem. Rev.*, 2011, **111**, 3858-3887.
26. L. J. Mendoza Herrera, D. M. Arboleda, D. C. Schinca, and L. B. Scaffardi, *J. Appl. Phys.*, 2014, **116**, 233105.
27. C. Louis and O. Pluchery, *Gold nanoparticles for physics, chemistry and biology*, World Scientific, 2017.
28. H. Wang, F. Tam, N. K. Grady and N. J. Halas, *J. Phys. Chem. B*, 2005, **109**, 18218-18222.
29. G. Mie, *Annalen der physik*, 1908, **330**, 377-445.
30. P. Mulvaney, J. Pérez-Juste, M. Giersig, L. M. Liz-Marzán, and C. Pecharromán, *Plasmonics*, 2006, **1**, 61-66.
31. C. Novo, A. M. Funston, A. K. Gooding, and P. Mulvaney, *J. Am. Chem. Soc.*, 2009, **131**, 14664-14666.
32. V. Amendola, R. Pilot, M. Frasconi, O. M. Maragò, and M. A. Iatì, *J. Phys.: Condens. Matter*, 2017, **29**, 203002.
33. T. Ming, H. Chen, R. Jiang, Q. Li, and J. Wang, *J. Phys. Chem. Lett.*, 2012, **3**, 191-202.
34. R. Jiang, B. Li, C. Fang, and J. Wang, *Adv. Mater.*, 2014, **26**, 5274-5309.
35. T. K. Sau, A. L. Rogach, F. Jäckel, T. A. Klar, and J. Feldmann, *Adv. Mater.*, 2010, **22**, 1805-

1825.

36. X. Kou, W. Ni, C. K. Tsung, K. Chan, H. Q. Lin, G. D. Stucky, and J. Wang, *Small*, 2007, **3**, 2103-2113.
37. T. Kawawaki, Y. Takahashi, and T. Tatsuma, *Nanoscale*, 2011, **3**, 2865-2867.
38. T. Kawawaki, Y. Takahashi, and T. Tatsuma, *J. Phys. Chem. C*, 2013, **117**, 5901-5907.
39. T. Kawawaki and T. Tatsuma, *Phys. Chem. Chem. Phys.*, 2013, **15**, 20247-20251.
40. F. Bonaccorso, M. Zerbetto, A. C. Ferrari, and V. Amendola, *J. Phys. Chem. C*, 2013, **117**, 13217-13229.
41. S. Wang, W. Xi, F. Cai, X. Zhao, Z. Xu, J. Qian, and S. He, *Theranostics*, 2015, **5**, 251-266.
42. L. Scarabelli, M. Coronado-Puchau, J. J. Giner-Casares, J. Langer, and L. M. Liz-Marzán, *ACS Nano*, 2014, **8**, 5833-5842.
43. H. L. Wu, C. H. Kuo, and M. H. Huang, *Langmuir*, 2010, **26**, 12307-12313.
44. T. Kawawaki, A. Asakura, and T. Tatsuma, *ChemNanoMat*, 2016, **2**, 74-78.
45. H. Nishi, T. Torimoto, and T. Tatsuma, *Phys. Chem. Chem. Phys.*, 2015, **17**, 4042-4046.
46. G. Barbillon, J. L. Bijeon, J. Plain, M. L. De La Chapelle, P. M. Adam, and P. Royer, *Surf. Sci.*, 2007, **601**, 5057-5061.
47. W. Yue, Z. Wang, Y. Yang, L. Chen, A. Syed, K. Wong, and X. Wang, *J. Micromech.Microeng.*, 2012, **22**, 125007.
48. L. F. Thompson, *An introduction to lithography*, ACS Publications, 1983.
49. C. L. Haynes and R. P. Van Duyne, *J. Phys. Chem. B*, 2001, **105**, 5599-5611.
50. J. C. Hulteen and R. P. Van Duyne, *J. Vac. Sci. & Technol. A*, 1995, **13**, 1553-1558.
51. Z. Zhang and J. T. Yates Jr, *Chem. Rev.*, 2012, **112**, 5520-5551.
52. X. Zhang, Y. L. Chen, R. S. Liu, and D. P. Tsai, *Rep. Prog. Phys.*, 2013, **76**, 046401.
53. N. Sakai, Y. Fujiwara, Y. Takahashi, and T. Tatsuma, *ChemPhysChem*, 2009, **10**, 766-769.
54. E. Kazuma and T. Tatsuma, *Adv. Mater. Interfaces*, 2014, **1**, 1400066.
55. Y. Zhang, C. Yam, and G. C. Schatz, *J. Phys. Chem. Lett.*, 2016, **7**, 1852-1858.
56. K. Wu, J. Chen, J. R. McBride, and T. Lian, *Science*, 2015, **349**, 632-635.
57. I. Tanabe and T. Tatsuma, *Nano Lett.*, 2012, **12**, 5418-5421.
58. E. Kazuma and T. Tatsuma, *Chem. Commun.*, 2012, **48**, 1733-1735.
59. K. Saito, I. Tanabe and T. Tatsuma, *J. Phys. Chem. Lett.*, 2016, **7**, 4363-4368.
60. A. Sousa-Castillo, M. Comesaña-Hermo, B. Rodríguez-González, M. Pérez-Lorenzo, Z. Wang, X. T. Kong, A. O. Govorov, and M. A. Correa-Duarte, *J. Phys. Chem. C*, 2016, **120**, 11690-11699.
61. T. Tatsuma, H. Nishi, and T. Ishida, *Chem. Sci.*, 2017, **8**, 3325-3337.
62. K. Yu, N. Sakai, and T. Tatsuma, *Electrochemistry*, 2008, **76**, 161-164.
63. M. W. Knight, H. Sobhani, P. Nordlander, and N. J. Halas, *Science*, 2011, **332**, 702-704.
64. Y. Takahashi and T. Tatsuma, *Appl. Phys. Lett.*, 2011, **99**, 182110.

65. P. Reineck, G. P. Lee, D. Brick, M. Karg, P. Mulvaney, and U. Bach, *Adv. Mater.*, 2012, **24**, 4750-4755.
66. F. P. García de Arquer, A. Mihi, D. Kufer, and G. Konstantatos, *ACS Nano*, 2013, **7**, 3581-3588.
67. W. Li and J. Valentine, *Nano Lett.*, 2014, **14**, 3510-3514.
68. S. Mubeen, J. Lee, W. R. Lee, N. Singh, G. D. Stucky, and M. Moskovits, *ACS Nano*, 2014, **8**, 6066-6073.
69. F. P. García de Arquer, A. Mihi, and G. Konstantatos, *ACS Photonics*, 2015, **2**, 950-957.
70. K. Nakamura, T. Oshikiri, K. Ueno, Y. M. Wang, Y. Kamata, Y. Kotake, and H. Misawa, *J. Phys. Chem. Lett.*, 2016, **7**, 1004-1009.
71. P. Reineck, D. Brick, P. Mulvaney, and U. Bach, *J. Phys. Chem. Lett.*, 2016, **7**, 4137-4141.
72. K. Naoi, Y. Ohko, and T. Tatsuma, *J. Am. Chem. Soc.*, 2004, **126**, 3664-3668.
73. N. Crespo-Monteiro, N. Destouches, L. Bois, F. Chassagneux, S. Reynaud, and T. Fournel, *Adv. Mater.*, 2010, **22**, 3166-3170.
74. A. Fujishima and K. Honda, *Nature*, 1972, **238**, 37-38.
75. M. Kim, M. Lin, J. Son, H. Xu, and J. M. Nam, *Adv. Optical Mater.*, 2017, 170004.
76. Y. Nishijima, K. Ueno, Y. Yokota, K. Murakoshi, and H. Misawa, *J. Phys. Chem. Lett.*, 2010, **1**, 2031-2036.

Chapter 2 Plasmon-Induced Charge Separation of Two-Dimensional Au Halfshell Arrays on SiO_2@TiO_2 Colloidal Crystals in a Wet Cell

2.1 Introduction

Recently, plasmonic metal semishell or halfshell arrays fabricated over two-dimensional (2D) colloidal crystals have been developed.[1-11] They are characterized by extensive absorption due to excitation of both propagating and localized surface plasmon resonance (PSPR and LSPR).[12,13] The optical properties can be easily tailored from visible to near-infrared (NIR) region by changing metal thickness, size of the supporting colloidal sphere, and dielectric environment.[2,5,6,10,11] Moreover, it was reported that strong optical near field is generated at the junctions between two adjacent metal semishells or halshells.[7,9] Therefore, metal semishell or halfshell array has been widely applied to plasmonic refractometry,[5] surface-enhanced Raman spectroscopy (SERS),[1,7,9,11] surface-enhanced fluorescence (SEF),[4,6,10] and photocurrent enhancement.[8]

Nevertheless, to the best of our knowledge, plasmon-induced charge separation (PICS) by using metal semishell or halfshell array has not yet been reported. Compared with typical PICS systems, dispersed and disordered metal nanoparticles (NPs) deposited on TiO_2, it is reasonable to expect that the periodic and interconnected metal semishell or halfshell array exhibits higher and wider PICS-based photoresponses because of their unique photonic and SPR properties as well as large contact area between metal and TiO_2.

In this chapter, periodic plasmonic photoelectrodes with Au semishell and halfshell arrays on two-dimensional (2D) SiO_2@TiO_2 core-shell colloidal crystals are developed. Their optical and PICS-based photoelectrochemical properties are investigated.

2.2 Experimental Methods

2.2.1 Fabrication of Photoelectrodes with Au Semishell and Halfshell Arrays

As shown in Figure 2.1, photoelectrodes with Au semishell and halfshell arrays were obtained by using 2D SiO_2@TiO_2 colloidal crystals as templates. In detail, they were fabricated through four steps: pretreatment of substrate, self-assembly of 2D SiO_2 colloidal crystal, formation of 2D SiO_2@TiO_2 array, and Au sputtering or evaporation.

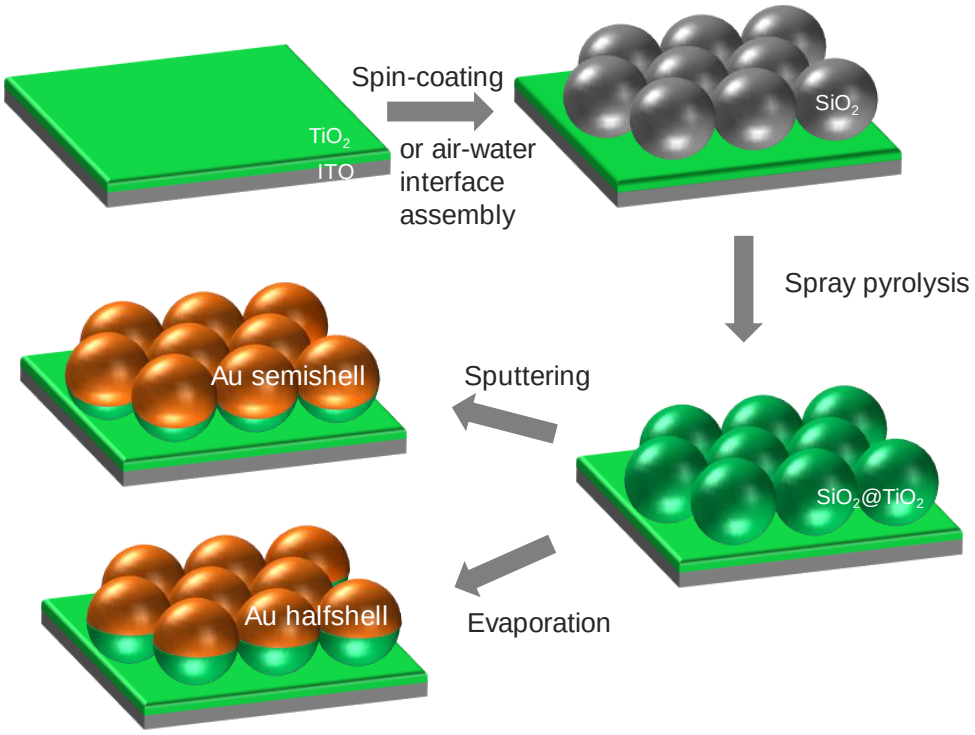

Figure 2.1 Schematic illustration for preparation of plasmonic photoelectrodes with Au semishell (or halfshell) array.

(1) Pretreatment of substrate

Indium tin oxide (ITO)-coated glass slides (1.1 cm × 4 cm) were ultrasonically washed by Milli-Q water, acetone, and 2-propanol successively. The slides were further coated with a compact TiO_2 layer by a spray pyrolysis technique using a precursor containing titanium diisopropoxide bis(acetylacetonate) and 2-propanol (volume ratio = 2:9).[14] Spray pressure and time were 0.12 MPa and 1 s (1 time), respectively. Calcination was carried out at 500 ºC for 30 min. The obtained substrates were exposed

to UV light for 30 min in order to make the surface clean and super-hydrophilic before use.

(2) Synthesis of monodispersed SiO_2 spheres

SiO_2 spheres of various diameters were synthesized by a modified Stöber method.[15]

SiO_2 spheres of 300 nm

Mixture of aqueous ammonia (28%, 14 mL), Milli-Q water (20 mL), and ethanol (99.5 vol%, 66 mL) and that of tetraethyl orthosilicate (TEOS, 8 mL) and ethanol (99.5 vol%, 92 mL) were poured simultaneously into a conical flask which was immersed in a water bath at 35 ºC. The reactant solution was stirred for 2.5 h.

SiO_2 spheres of 261 and 374 nm

Aqueous ammonia (0.8 or 3 g), Milli-Q water (6.367 or 5.710 g), and ethanol (16.525 or 16.226 g) were mixed and stirred for 10 min at room temperature. TEOS (1.676 mL) was then dropwise added to the solution, keeping stirring the mixture for 3 h.

SiO_2 spheres of 581 nm

Aqueous ammonia (1.9 g) was mixed with ethanol (8.87 g) and stirred for 10 min. Then, a mixture of TEOS (0.1 mL) and ethanol (0.3235 g) was dropwise added to the solution, keeping stirring for 2 h. Finally, a mixture of aqueous ammonia (2.5 g), TEOS (1.55 mL), and ethanol (4.535 g) were dropwise added to the solution and further stirred for 8−12 h.

The resultant white precipitates were collected by centrifugation at 8000 × g and washed by ethanol for several times. The obtained SiO_2 spheres were ultrasonically dispersed in Milli-Q water or 1-butanol.

(3) Fabrication of 2D SiO_2 and SiO_2@TiO_2 colloidal crystals

Self-assembly of two-dimensional (2D) SiO_2 colloidal crystal was performed by two different ways as shown in Figures 2.2 and 2.3.

Spin-coating

The SiO_2 suspension of 15 wt% was diluted with an equal volume of ethanol. The diluted SiO_2 suspension of 80 μL was dropped on the pretreated ITO/TiO_2 substrate and spin-coated at 1800 rpm for 60 s with acceleration rate of 800 rpm s^{-1}.

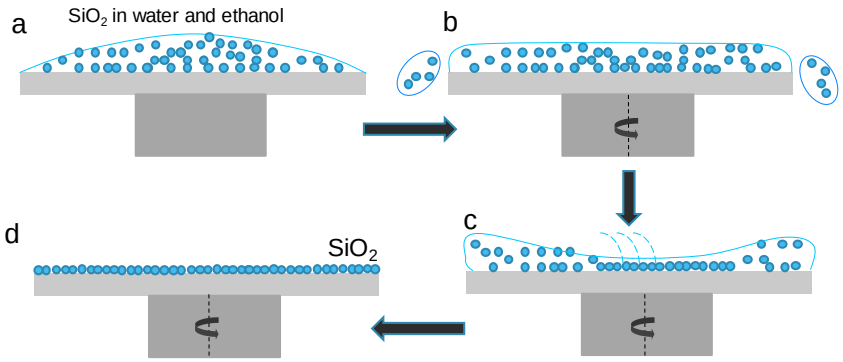

Figure 2.2 Schematic illustration for self-assembly of 2D SiO_2 colloidal crystal by spin-coating.

Air-water interface self-assembly[10]

The SiO_2 spheres dispersed in 1-butanol was dropped gently on the water surface in a Petri dish, resulting in the self-assembly of the SiO_2 spheres at the air-water interface to form a 2D colloidal crystal. The 2D colloidal crystal was transferred to the pretreated and wetted ITO/TiO_2 substrate by making a contact between the substrate and the water surface.

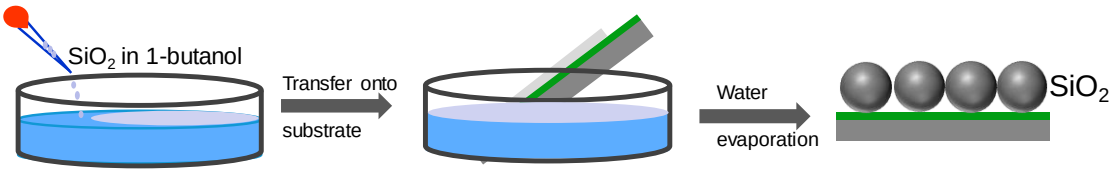

Figure 2.3 Schematic illustration for self-assembly of 2D SiO_2 colloidal crystal at air-water interface.

TiO_2 shell was coated on the 2D SiO_2 array by the spray pyrolysis method (1 s × 2 times) to form a SiO_2@TiO_2 core-shell colloidal crystal.

(4) Au sputtering or evaporation

Au semishell and halfshell arrays were obtained through sputtering (E-1030, Hitachi, 6 Pa, 0.27 nm s^{-1}) and thermal evaporation (0.3 nm s^{-1}, < 4 × 10^{-4} Pa) of Au onto the colloidal crystal, respectively. For the former one, the Au thickness was calculated according to the sputtering rate and time. In the case of the latter one, that was monitored by a quartz crystal microbalance (QCE).

2.2.2 Characterization

The morphologies of the prepared electrodes were investigated by a scanning electron microscope (SEM, JSM-7500FA, JEOL) and a transmission electron microscope (TEM, JEOL-2010F, JEOL). The optical properties of the electrodes were measured by a spectrophotometer (V-670, Jasco) equipped with an integrating sphere.

2.2.3 Photoelectrochemical Measurements

Photoelectrochemical measurements were performed using a two-electrode and single-compartment cell with a potentiostat (SI 1280B, Solartron). The electrode with Au semishell or halfshell array was used as the working electrode. For open-circuit photopotential measurements, the reference electrode was a Pt wire or Ag|AgCl (sat. KCl) and the electrolyte was 0.1 M KNO_3 aqueous solution. For short-circuit photocurrent measurements, the counter electrode and the electrolyte were a Pt wire and 0.1 M aqueous KNO_3 containing 0.1 M or 0.5 M electron donor, respectively. Monochromatic light (3.75 × 10^{15} photons cm^{-2} s^{-1}) was illuminated to the working electrode from the backside (ITO side) using a Xe lamp (LAX-103, Asahi Spectra) equipped with band-pass filters (full width at half maximum = 10 nm).

2.2.4 Computational Simulation

The optical spectra of the Au halfshell arrays were simulated by using a finite-difference time-domain (FDTD) algorithm software (FDTD Solutions, Lumerical Solutions). The calculation model is illustrated in Figure 2.4: Au halfshell array (thickness = 55 nm) on the 2D hexagonal close-packed SiO_2 array (diameter = 261, 374 or 581 nm) coated by a TiO_2 shell (thickness = 20 nm). The dielectric functions for SiO_2,

TiO_2, and Au were obtained from literatures reported by Palik *et al.*,[16] Jellison *et al.*,[17] and Johnson and Christy,[18] respectively. A periodic boundary condition was imposed in the *y* and *z* direction and a perfect matching layer (PML) was imposed in the *x* direction. The model was irradiated from the backside with a plane wave source (300−1100 nm) propagating along the *x* direction and polarized parallel to the *z* direction. Two frequency-domain field and power monitors were used to calculate transmittance (*T*) and reflectance (*R*). Two frequency-domain field profile monitors were set in the *yz* and *xz* plane to visualize the intensity of electric field as shown by the white and black dashed line in Figure 2.4, respectively.

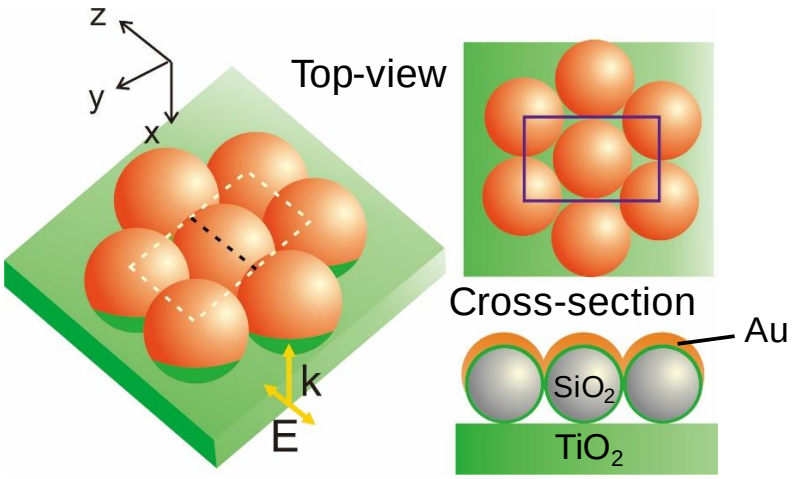

Figure 2.4 FDTD simulation model of Au halfshell array electrodes. The purple solid lines represent the calculation area. The white and black dashed lines denote two monitors for detecting optical near field.

2.3 Results and Discussion

2.3.1 Morphologies of the Prepared Arrays

The SEM images of a 2D SiO_2 colloidal crystal (300 nm) prepared by spin-coating were shown in Figure 2.5. It was clearly observed that SiO_2 spheres were in contact with six neighboring ones to form a hexagonal close-packed structure. Although there are a few multilayer domains and defects such as mismatches and cracks, the film is composed mostly of monolayer.

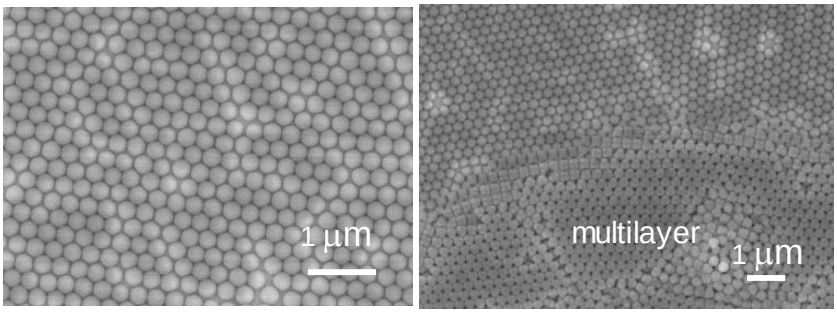

Figure 2.5 SEM images of a 2D SiO_2 colloidal crystal prepared by spin-coating. SiO_2 diameter = 300 nm.

Figure 2.6a and b show typical SEM images of a 2D SiO_2@TiO_2 colloidal crystal. After coating of a TiO_2 shell, the hexagonal structure was still retained. The surface of the SiO_2@TiO_2 spheres was very smooth. From TEM observation (Figure 2.6c), it can be seen that the TiO_2 layer of ca. 20 nm perfectly covers the whole surface of the SiO_2 core and connects to the underlying TiO_2, just as is the case for Au nanospheres coated with TiO_2.[18]

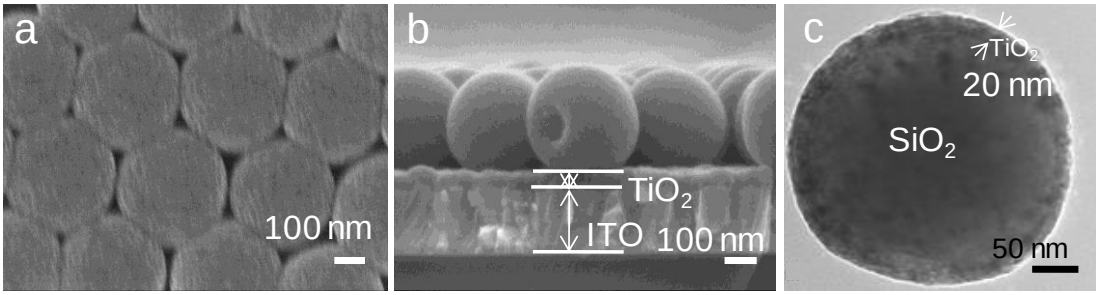

Figure 2.6 (a, b) SEM images of the 2D SiO_2@TiO_2 colloidal crystal and (c) TEM image of the SiO_2@TiO_2 particle.

SEM images of Au semishell arrays sputtered on SiO_2@TiO_2 colloidal crystals are shown in Figure 2.7. The periodic hexagonal structrue was maintained even after Au deposition. The TiO_2 compact layer, SiO_2@TiO_2 spheres, and Au semishells can be observed in the cross-sectional images, indicating that the desired plasmonic electrode is successfully prepared. It should be noted that Au is sputtered on most of the TiO_2

surface and preferentially piled up at the top of the SiO_2@TiO_2 sphere. The sharpness of the groove between two adjacent Au semishells was decreased with increasing the Au thickness from 8 to 96 nm.

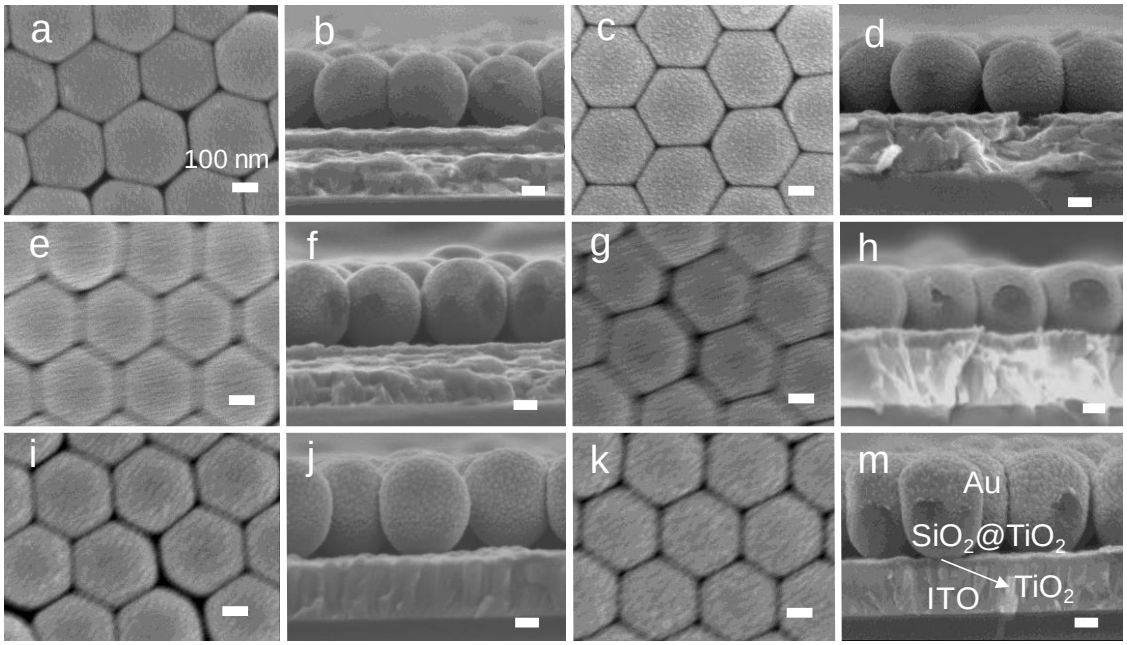

Figure 2.7 SEM images of Au semishell arrays sputtered on SiO_2@TiO_2 colloidal crystals. Au thickness: (a, b) 8, (c, d) 16, (e, f) 24, (g, h) 48, (i, j) 64, and (k, m) 96 nm. All scale bars are 100 nm.

Unlike in the case of sputtering, the evaporation technique led to the formation of perfect Au halfshells, that is, Au was only deposited on the upper surface of the SiO_2@TiO_2 sphere (Figure 2.8). The difference in the morphology maybe derive from the difference in directionality of metal ions in sputtering and evaporation processes. Actually, halfshell structures were fabricated typically by thermal evaporation in the previous studies.[4-10] The sharpness of the groove between two adjacent Au halfshells remained unchanged with the increase of Au thickness.

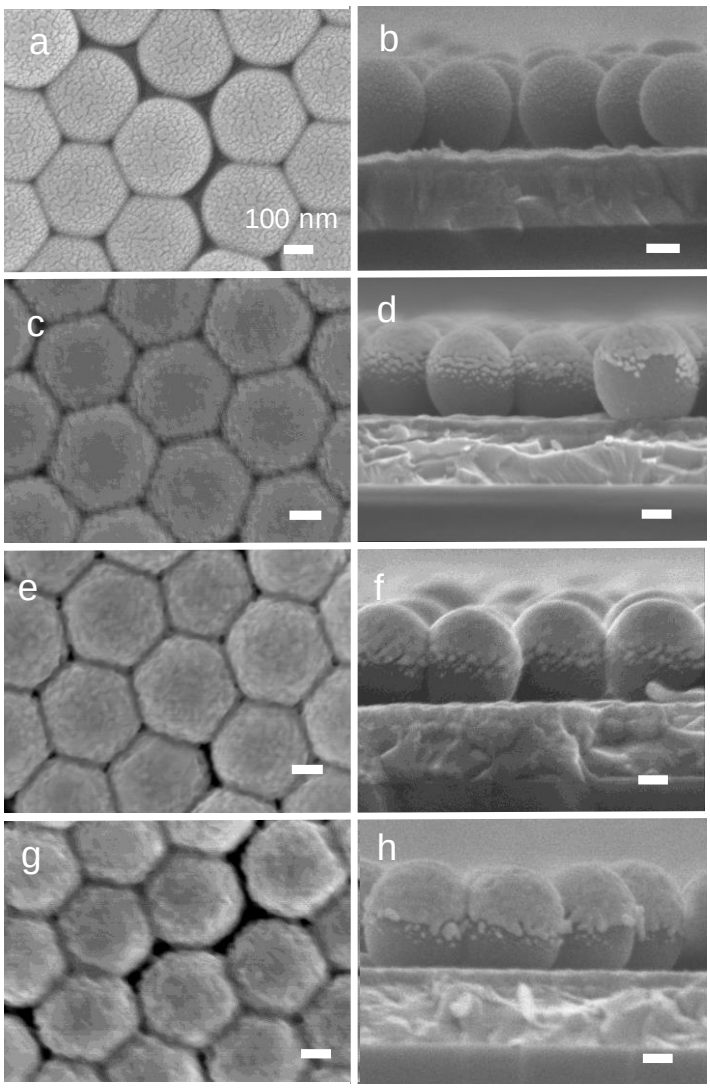

Figure 2.8 SEM images of Au halfshell arrays evaporated on SiO_2@TiO_2 colloidal crystals: Au thicknesses: (a, b) 10, (c, d) 25, (e, f) 55, and (g, h) 80 nm. The evaporation rate: 0.3 nm s^{-1}. All scale bars are 100 nm.

2.3.2 Optical Properties

The optical properties of SiO_2@TiO_2 colloidal crystals with and without Au semishell or halfshell array were examined. Absorption (A) was calculated from transmittance (T) and reflectance (R) according to equation $A = 100 - T - R$. Figure 2.9a and b show the absorption spectra of the electrodes (back incidence) prepared by sputtering and evaporation, respectively. The absorption spectrum of the electrode with a bare SiO_2@TiO_2 colloidal crystal is also presented as the reference. The absorption in

the UV region shorter than 380 nm is assigned to the interband transitions of TiO_2, while the absorption peak in the visible region at 448 nm is attributed to a photonic resonance. When the optical diameter (= diameter × refractive index) of the ordered structure is comparable to the wavelength of incident light, an absorption is observed because of light propagation parallel to the colloidal crystal.[6] The electrodes with sputtered Au semishell and evaporated halfshell arrays exhibited broad absorption in the visible and NIR range examined. It can also be seen that the absorption increases with the increase of Au thickness. Each spectrum includes interband transition of Au, photonic resonances of the periodic array, plasmonic absorption of the semishell or halfshell array. As reported in other literatures, the interconnected metal halfshell array shows both PSPR and LSPR.[12, 13] Unfortunately, it has not been quantitatively figured out the contribution of PSPR and LSPR to the absorption spectra.

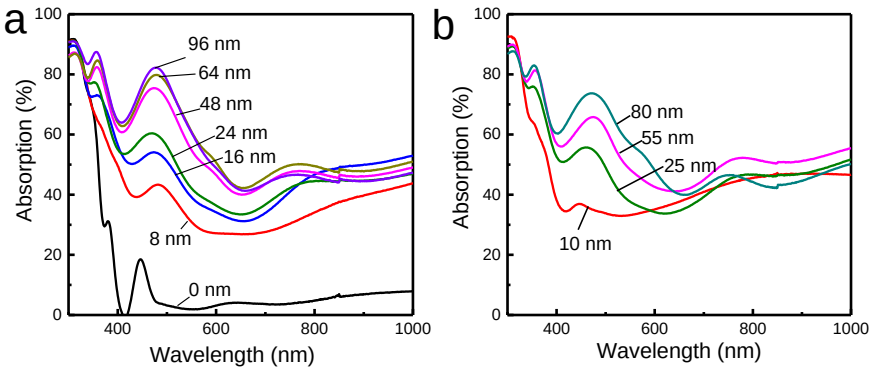

Figure 2.9 Absorption spectra of the electrodes with (a) sputtered and (b) evaporated Au arrays of various thicknesses.

2.3.3 PICS Behaviors

The electrodes with semishell arrays of different thicknesses exhibited negative photopotential shifts and anodic photocurrent responses under light irradiation. The photopotential response and incident photon-to-current conversion efficiency (IPCE) spectra in the wavelength range of 500-800 nm were shown in Figure 2.10a and b. The semishell array electrodes exhibited broad photorensponses in the visible and NIR regions, indicating that PICS is caused at the interface between the Au semishells and

the TiO_2 shells as is the case for the conventional PICS systems.[19,20] Figure 2.10c illustrates the possible PICS mechanism. Photoexcited electrons are transferred from the Au semishells to the conduction band of the TiO_2 and then transported to the counter electrode through outer circuit, while holes in the Au semishells are used for oxidation of electron donors such as hydroquinone. The electrode with bare SiO_2@TiO_2 colloidal crystal showed very low photoresponses at >600nm because there is almost no absorption in the wavelength range examined. However, the photoresponses, especially photocurrent responses, are not negligible in the short wavelength range. The large photocurrent responses to hydroquinone must be due to a trace amount of oxidized hydroquinone as a photosensitizer for TiO_2, which is photoexcited, particularly at <600 nm (Figure 2.10d). Actually, the color of the hydroquinone aqueous solution turned orange after keeping it for 4 months under the ambient conditions (Figure 2.10e) and photocurrents of the electrode with the SiO_2@TiO_2 colloidal crystal were further enhanced in the presence of the oxidized hydroquinone. The lower IPCE for the Au semishell array at <600 nm is explained in terms of a decrease in the exposed surface area of TiO_2.

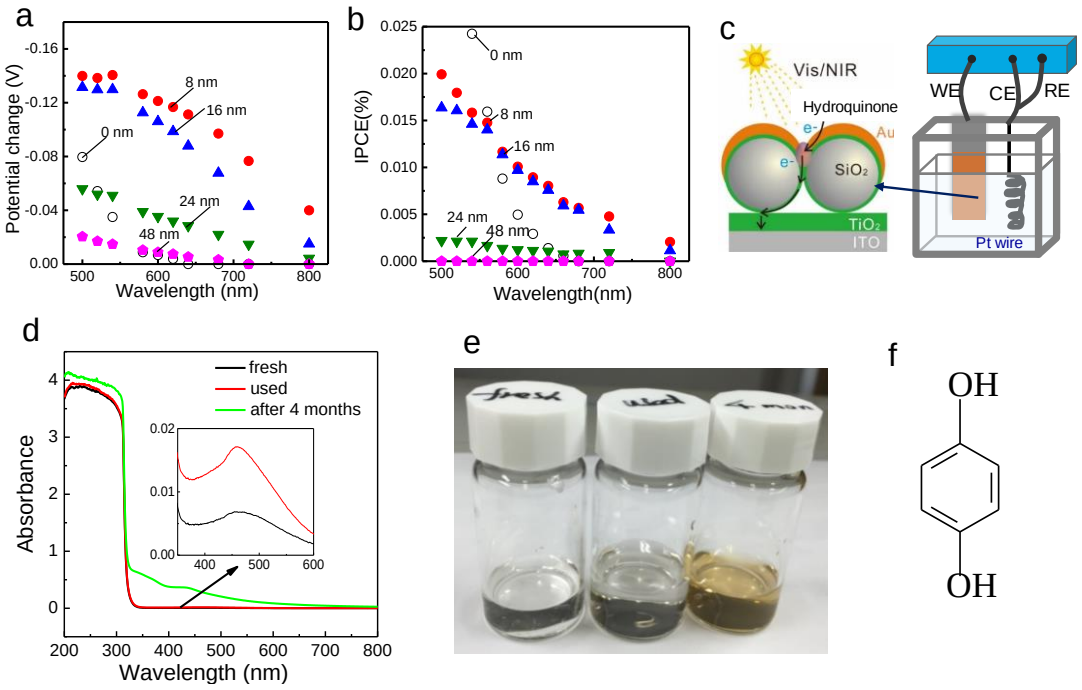

Figure 2.10 (a) Open-circuit photopotential and (b) short-circuit photocurrent responses of the

electrodes with sputtered Au semishell arrays of various thicknesses. Electrolyte: (a) 0.1M aqueous KNO_3, (b) 0.1 M KNO_3 with 0.1 M hydroquinone. (c) Schematic illustration of experimental setup for photoelectrochemical measurements and mechanism of PICS at Au semishell arrays on SiO_2@TiO_2 colloidal crystals. (d) Absorption spectra and (e) photographs of the hydroquinone aqueous solutions: freshly prepared one (left), that after photocurrent measurement (middle), and that after aging for 4 months (right). (f) Structural formula of hydroquinone used in the experiment.

The photopotential and photocurrent responses decreased with increasing the thickness of Au semishells as shown in Figure 2.10a and b. FDTD simulations reported elsewhere[7,9] and discussed later show that the semishell array generates strong localized electric field (*i.e.* optical near field) at the junctions between two adjacent semishells. It has been reported that PICS-based anodic reaction such as dissolution of Ag NPs deposited on TiO_2 proceeds preferentially at the sites where the optical near field is generated.[21-23] Moreover, the strong optical near field is advantageous for the generation of electron-hole pairs.[24] Since increase of the thickness of Au semishells leads to decrease in the sharpness of the groove and weaker optical near field, it is reasonable to think that the PICS-based oxidation of hydroquinone takes place at the semishell junctions and thinner semishells achieved higher PICS efficiency. In addition, the electron diffusion pathway becomes longer as the Au thickness increases, which thermalizes more electrons through electron-phonon relaxations.

Negative photopotential shifts (Figure 2.11a) and anodic photocurrent responses (Figure 2.11b) were also observed for the electrodes with evaporated Au halfshell arrays. The photoresponses were basically higher than those of the electrodes with sputtered semishell arrays. The electrode with 55-nm-thick Au halfshell array exhibited higher photoresponses than that with the halfshell of 25 or 80 nm. It is thought that the optical near field at the junctions may be intensified due to the increase of Au thickness without the decrease of groove sharpness, whereas the electron diffusion pathway becomes longer with increasing the Au thickness. Due to these competitive factors, the optimal thickness of Au halfshell is 55 nm in our experiment. Anodic photocurrents were also detected when hydroquinone was replaced with methanol, ethanol, or $[Fe(CN)_6]^{4-}$

(Figure 2.11c). Photocurrent was almost zero without Au halfshells, indicating that the anodic photocurrents are derived from photocatalytic oxidation of the donors based on PICS. The electrode exhibited anodic photocurrents even in 0.1 M KNO_3 aqueous solution, which suggests that water could also be an electron donor. Here, hydroquinone and ethanol are good electron donors for generation of higher photocurrents.

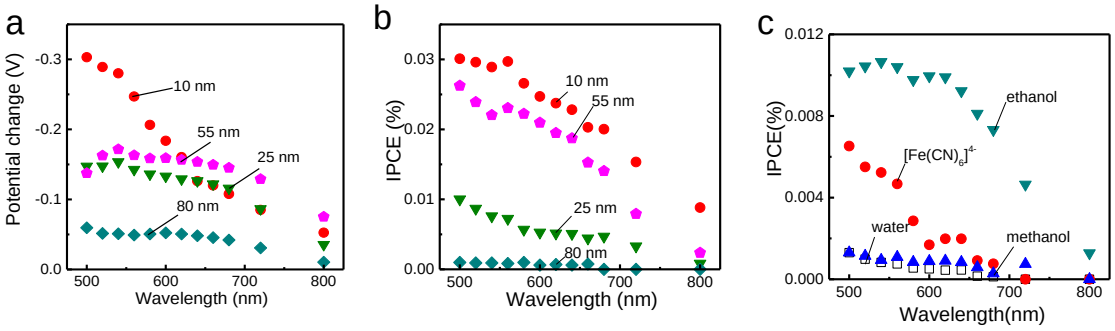

Figure 2.11 (a) Open-circuit photopotential and (b, c) short-circuit photocurrent responses of electrodes with evaporated Au halfshell arrays. The Au thickness in panel c is 55 nm. Electrolyte: (a) 0.1M aqueous KNO_3, (b) 0.1M aqueous KNO_3 with 0.1M hydroquinone, and (c) 0.1M aqueous KNO_3 with another electron donor (0.1 M).

As shown in Figure 2.12a and b, absorption and IPCE spectra of the electrode with Au halfshell array were compared with those with Au nanospheres of 13 nm. The nanospheres were prepared by a citrate reduction method[25] and deposited on ITO/TiO_2 (ca. 60 nm) electrode fabricated by a spray pyrolysis method.[26] A LSPR peak is clearly observed at 530 nm from the absorption spectrum of the electrode with Au nanospheres. However, the absorption in the NIR region was very weak. The shape of the IPCE spectrum for the nanospheres is in good accordance with the corresponding absorption spectrum. In contrast, the electrode with Au halfshell array exhibited very broad absorption in the visible and NIR regions. The IPCE values of the Au halfshell array are much higher than those of Au nanospheres especially at >600 nm because of the stronger absorption and larger contact area between Au and TiO_2. Although the absorption in the NIR region was as high as that in shorter wavelength range, the IPCE

values are much lower. As illustrated in Figure 2.12c, low energetic photons can't overcome the Schottky barrier E_{SB}, leading to lower IPCE in the longer wavelength region. Similar results were also reported in the literatures.[27]

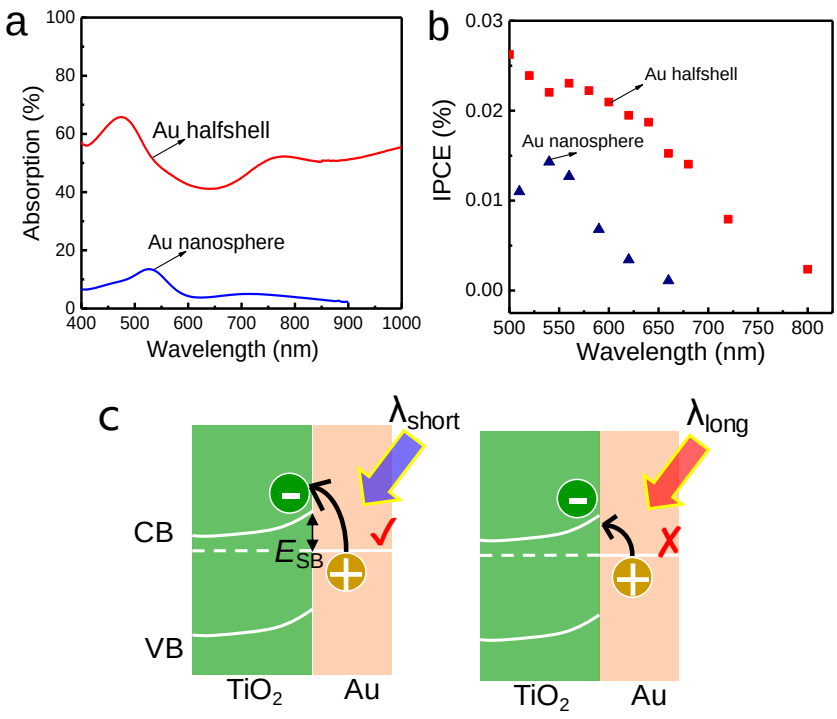

Figure 2.12 (a) Absorption spectra and (b) photocurrent action spectra of electrodes with disordered Au NPs and periodic Au halfshell array. (c) Schematic illustration of PICS at the interface between Au and TiO_2 upon shorter- and longer-wavelength light irradiation.

2.3.4 Dependence on SiO_2 Core Size

Dependence of the PICS-based photoelectrochemical properties of the Au halfshell array on the size of SiO_2 core was further examined. First, SiO_2 spheres of 261, 374, and 581 nm were self-assembled into 2D colloidal crystals by an air-water interface self-assembly method which is regarded as an effective approach for the preparation of large-area colloidal monolayers.[28] The morphology of the resultant colloidal crystal was shown in Figure 2.13a-c. Regardless of the particle size, they are arranged in a hexagonal close-packed structure and consist of almost 100% monolayer

domains. These colloidal crystals exhibited vivid structural colors depending on the SiO_2 size (Figure 2.13a-c). The extinction spectra of the colloidal crystals with diameters of 261, 374, and 581 nm at normal incidence showed clear peaks at around 603, 647, and 718 nm, respectively (Figure 2.13d). These peaks in the visible region can be explained in terms of photonic waveguide mode of the periodic structure. Incident light propagates horizontally to the structure, resulting in the fall of transmission in the vertical direction.[29] The peak is red-shifted with the increase of particle size. Appearance of optical peaks derived from structural colors confirms the formation of periodic structures.

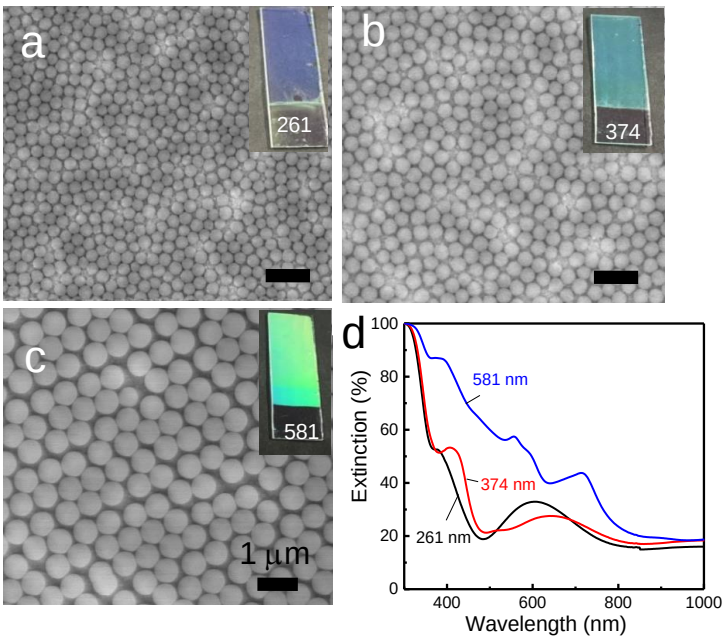

Figure 2.13 (a-c) SEM images of 2D SiO_2 colloidal crystals prepared by the air-water interface self-assembly method. SiO_2 diameter: (a) 261, (b) 374, and (c) 581 nm. The insets are the corresponding photographs. (d) Extinction spectra of the 2D SiO_2 colloidal crystals. All scale bars are 1 μm.

Figure 2.14 shows top-view and cross-sectional SEM images of the Au halfshell arrays with different SiO_2 sizes. These images indicate that the ordered structure of the colloidal crystal is maintained even after successive deposition of TiO_2 shell and Au halfshell. The size of the halfshell increased with increasing the diameter of the SiO_2 cores. Therefore, the Au halfshell arrays showed vivid but diverse colors due to the

different structural periods (insets of Figure 2.14a, c, and e). As shown in Figure 2.15a, the electrode without Au halfshells exhibited very weak absorption except for some photonic peaks in the visible and NIR regions. After Au evaporation, they showed broad absorption in the whole wavelength range examined.

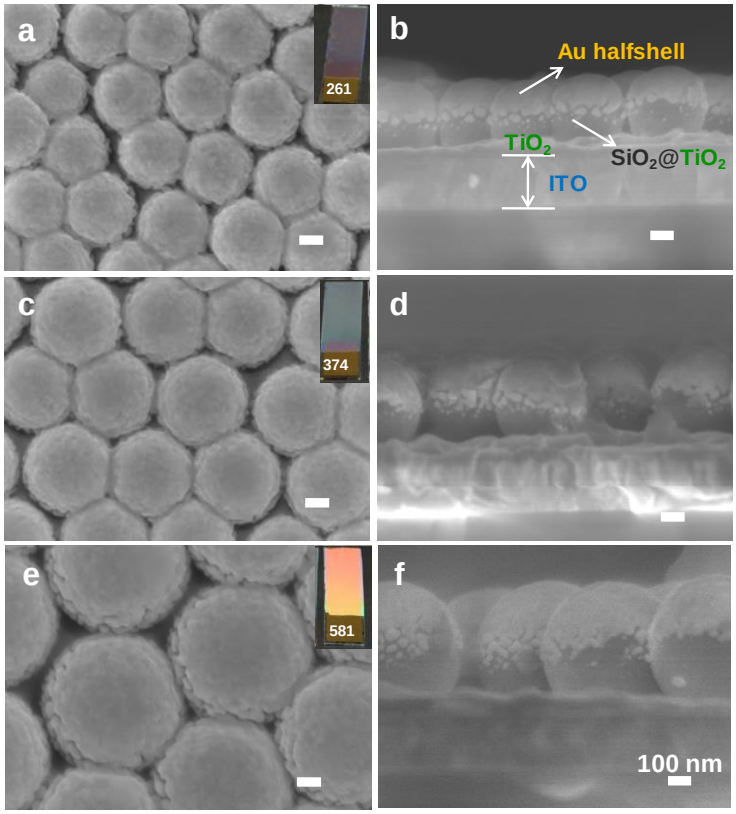

Figure 2.14 SEM images of Au halfshell arrays on SiO_2@TiO_2 colloidal crystals with different core sizes. SiO_2 diameter: (a, b) 261, (c, d) 374, and (e, f) 581 nm. The insets are the corresponding photographs. All scale bars are 100 nm.

Next, FDTD calculation was carried out to simulate the experimentally obtained optical spectra of the electrodes without and with Au halfshell arrays. Figure 2.15b shows the simulated and experimentally obtained transmittance (T) and reflectance (R) spectra for the Au halfshell arrays with the SiO_2 core of 261 nm. The shapes of the simulated spectra are roughly in accordance with the corresponding experimental results in the wavelength range of 500−1000 nm. However, some sharp peaks and dips are observed in the simulated spectra at <500 nm, which do not appear in the

experimental spectra because some structural defects exist in the real samples. It should be noticed that the simulated spectra seem to be red-shifted in comparison with the experimental ones, probably due to sharper structures of the simulation model (Figure 2.4). The simulated and measured absorption spectra ($A = 100 - T - R$) of the electrodes without and with Au halfshell arrays are summarized in Figure 2.15c. All the simulated spectra roughly match the experimental ones. The mismatch between them may also be because of the defects and randomly oriented domains.

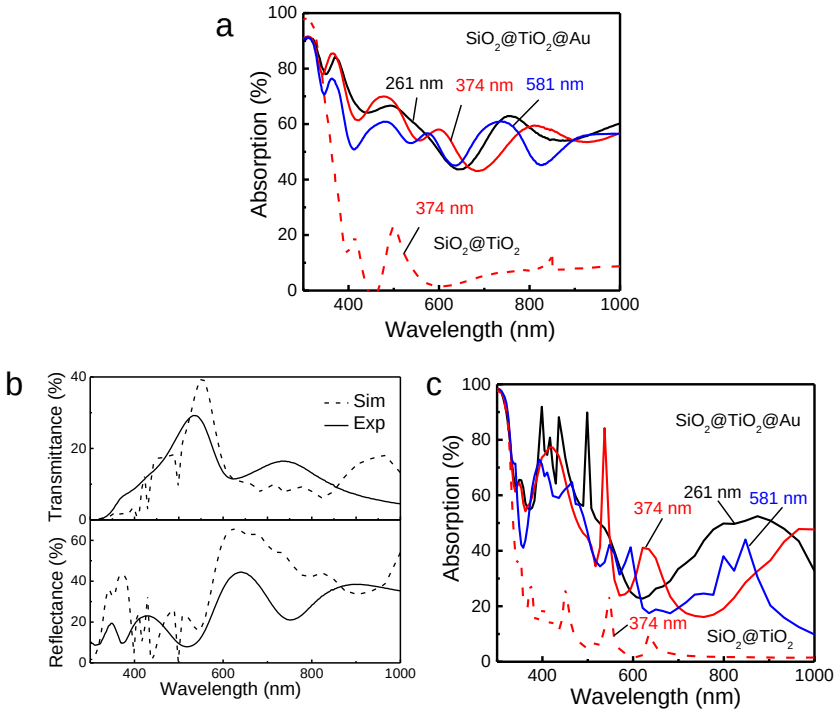

Figure 2.15 (a) Experimentally obtained absorption spectra of electrodes without and with Au halfshell arrays (SiO_2 diameter: 261, 374, and 581 nm). (b) Comparison of experimental and FDTD simulated transmittance and reflectance spectra of Au halfshell array (SiO_2 diameter: 261 nm). (c) Simulated absorption spectra of electrodes without and with Au halfshell arrays.

In ordered to examine the influence of halfshell size on the PICS efficiency, photoelectrochemical measurements were carried out in a wet cell. Figure 2.16 shows open-circuit photopotential and short-circuit photocurrent responses of the electrodes with and without Au halfshell arrays. The electrode without Au halfshell (SiO_2 size =

374 nm) exhibited small negative photopotential shifts and almost no photocurrent responses at <600 nm, which is cuased by the weak absorption of TiO_2. After Au deposition, all the electrodes showed much larger photoresponses in the wavelength range examined as is the case for that with SiO_2 colloidal crystal of 300 nm prepared by the spin-coating technique (Figures 2.10 and 2.11). Among the electrodes with different SiO_2 core sizes, the middle-sized one (374 nm) showed the highest photoresponses, which is around fourfold higher than those of the electrode by the spin-coating technique (Figure 2.11c) although the ethanol concentration is different. In order to explain the relationship between the core size and PICS efficiency, electric field distribution around Au halfshell arrays was calculated and its effect was discussed in the next section.

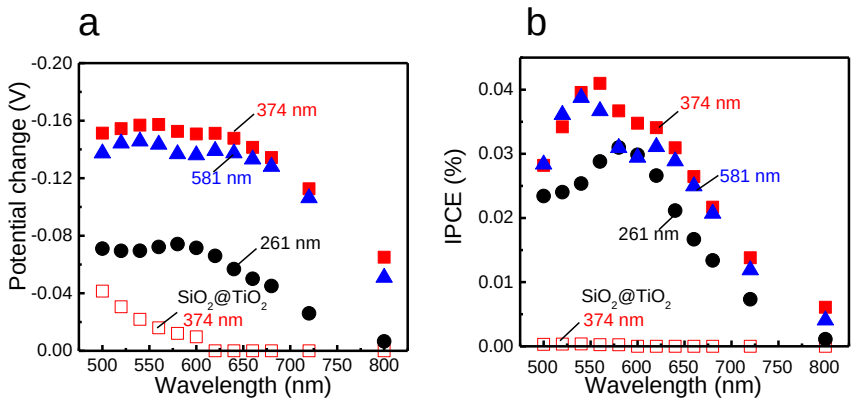

Figure 2.16 (a) Open-circuit photopotential and (b) short-circuit photocurrent responses of electrodes without and with Au halfshell arrays on SiO_2@TiO_2 colloidal crystals (SiO_2 diameter: 261, 374, and 581 nm). 0.5 M ethanol was used as the electron donor in the photocurrent measurements.

2.3.5 Effect of Optical Near Field

Figure 2.17a and b show the simulated electric filed distributions for the bare SiO_2@TiO_2 colloidal crystal (SiO_2 diameter = 374 nm) under irradiation at 665 and 547 nm, respectively. $|E|^2/|E_0|^2$ in these images denotes the electric field enhancement, where $|E|^2$ is the intensity of the electric field around the Au halfshell array, and $|E_0|^2$ is that of

the incident light in vacuum. Optical near fields with relatively low intensity are observed only at the junctions between two adjacent particles along the polarization direction when the colloidal crystal is illuminated at 665 nm. Upon irradiation at 547 nm (peak wavelength of the absorption spectrum shown in Figure 2.15c), in contrast, there are fringes of the electric field orthogonal to the polarization direction, suggesting that light propagates laterally through the SiO_2@TiO_2 colloidal crystals.[29] Such light propagation can also be seen from the electric field distributions for the Au halfshell arrays with SiO_2 cores of 374 and 581 nm (Figure 2.17c and d). The light propagation increases the path length and may enhance LSPR absorption of the halfshell arrays. The halfshell array with the cores of 374 nm showed the most intense electric field fringes and the highest photopotential and photocurrent responses in the 500−600 nm range. It is thus concluded that this strong light propagation through the middle-sized SiO_2@TiO_2 colloidal crystals is partially responsible for the high photoresponses.

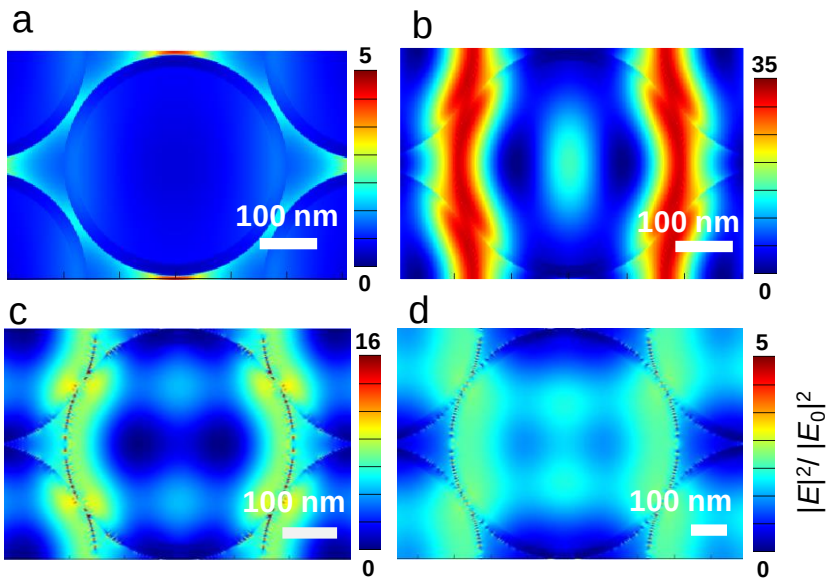

Figure 2.17 FDTD simulated electric filed distribution (top view) for bare SiO_2@TiO_2 colloidal crystal (SiO_2 diameter: 374 nm) under irradiation at (a) 665 and (b) 547 nm. That for Au halfshell arrays on the colloidal crystals with SiO_2 diameter of (c) 374 and (d) 581 nm under irradiation at 537 and 570 nm, respectively.

Strong electric fields are localized sharply at the junctions between two adjacent halfshells at 600−800 nm, as marked with the arrows in Figure 2.18b-e**.** Similar results were reported for Au semishells on TiO_2 hollow spheres,[9] Ag semishells on polystyrene spheres,[12,30,31] and Cu halfshells on SiO_2 spheres.[10] It has been reported that an isolated metal halfshell has two different plasmon modes: a transverse electron oscillation parallel to the rotational symmetry axis of the halfshell (α mode), and a longitudinal electron oscillation perpendicular to the axis (β mode),[32,33] as illustrated in Figure 2.18f. Since the α mode is suppressed in the array structure when the light is normally incident,[32] the strong electric fields located at the halfshell junctions are ascribed to the β mode. Figure 2.18a summarizes the maximum electric field enhancement ($|E|^2/|E_0|^2$) at the junction of Au halfshells as a function of irradiation wavelength. The array with the SiO_2 cores of 374 nm exhibits the highest values. Consequently, it is reasonable that the electrode with the middle-sized SiO_2 core exhibits the highest photocurrent responses.

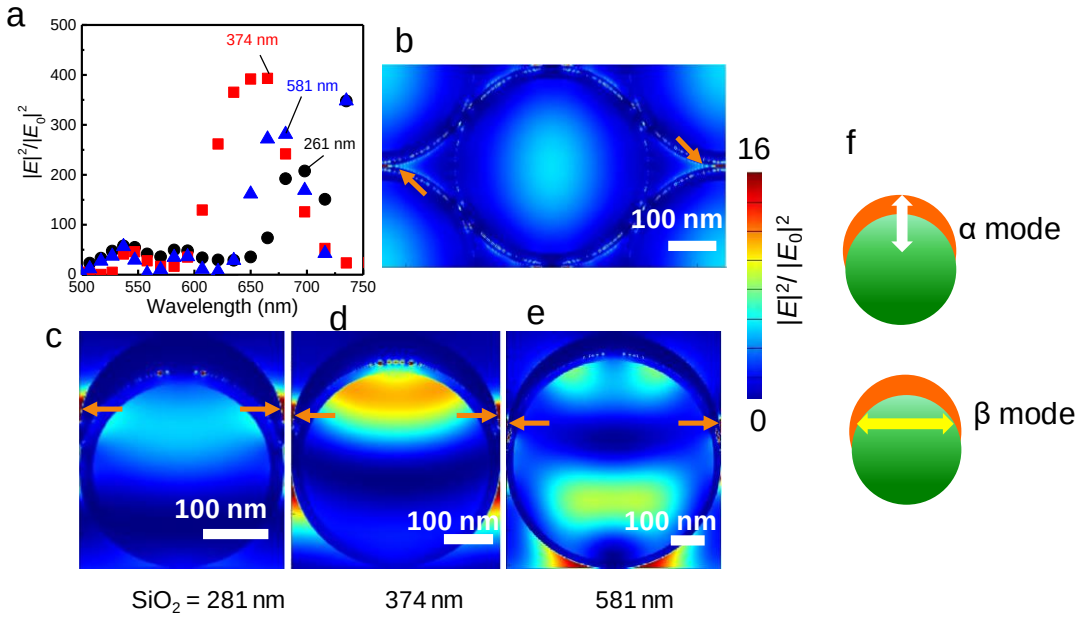

Figure 2.18 (a) Maximum electric field enhancement at the junction of Au halfshells (marked by the arrows in b-f) as a function of irradiation wavelength. Simulated electric filed distribution for Au halfshell arrays on SiO_2@TiO_2 colloidal crystals with SiO_2 diameters of (c) 261, (b, d) 374, and

(e) 581 nm under irradiation at (c) 698, (b, d) 665, and (e) 681 nm. (f) Scheme illustrating two different plasmon modes (α and β) of an isolated metal halfshell.

2.4 Conclusions

In summary, the plasmonic photoelectrodes with sputtered Au semishell arrays and halfshell arrays on SiO_2@TiO_2 colloidal crystals were developed and their PICS behaviors were investigated. All the electrodes exhibited broad absorption, negative open-circuit photopotential shifts, and anodic short-circuit photocurrent responses in the visible and NIR regions. The evaporated halfshell arrays showed higher PICS efficiency than the sputtered semishell ones. The dependence of PICS efficiency on the size of the SiO_2 was also examined. The photoelectrode with the middle-sized SiO_2 cores (374 nm) showed the highest photoresponses, which can be explained in terms of the highest electric field enhancement based on FDTD simulation. Compared with the conventional electrode with dispersed and disordered Au nanospheres, the present electrode with periodic and interconnected Au halfshell array possesses better controllability over the factors closely related to PICS. Moreover, they exhibit broader and more extensive absorption in the visible and NIR regions, due to supporting LSPR, PSPR, and photonic resonance, leading to higher and wider PICS-based photoresponses.

2.5 References

1. M. Baia, L. Baia, and S. Astilean, *Chem. Phys. Lett.*, 2005, **404**, 3-8.
2. P. Zhan, Z. L. Wang, H. Dong, J. Sun, J. Wu, H. T. Wang, S. N. Zhu, N. B. Ming, and J. Zi, *Adv. Mater.*, 2006, **18**, 1612-1616.
3. L. Landström, D. Brodoceanu, K. Piglmayer, and D. Bäuerle, *Appl. Phys. A*, 2006, **84**, 373-377.
4. T. Yamaguchi, T. Kaya, and H. Takei, *Anal. Biochem.*, 2007, **364**, 171-179.
5. Y. Li, J. Sun, L. Wang, P. Zhan, Z. Cao, and Z. Wang, *Appl. Phys. A*, 2008, **92**, 291-294.
6. C. Farcău and S. Aştilean, *Appl. Phys. Lett.*, 2009, **95**, 193110.
7. C. Farcau and S. Astilean, *J. Phys. Chem. C*, 2010, **114**, 11717-11722.
8. K. Sugawa, S. Hirono, T. Akiyama, and S. Yamada, *Photochem. Photobiol. Sci.*, 2012, **11**, 318-

322.

9. X. Li, H. Hu, D. Li, Z. Shen, Q. Xiong, S. Li, and H. J. Fan, *ACS Appl. Mater. Interfaces*, 2012, **4**, 2180-2185.
10. K. Sugawa, T. Tamura, H. Tahara, D. Yamaguchi, T. Akiyama, J. Otsuki, Y. Kusaka, N. Fukuda, and H. Ushijima, *ACS Nano*, 2013, **7**, 9997-10010.
11. J. Wang, F. Zhou, G. Duan, Y. Li, G. Liu, F. Su, and W. Cai, *RSC Adv.*, 2014, **4**, 8758-8763.
12. C. Farcau, M. Giloan, E. Vinteler, and S. Astilean, *Appl. Phys. B*, 2012, **106**, 849-856.
13. L. Baia, M. Baia, J. Popp, and S. Astilean, *J. Phys. Chem. B*, 2006, **110**, 23982-23986.
14. T. Kawawaki, Y. Takahashi, and T. Tatsuma, *Nanoscale*, 2011, **3**, 2865-2867.
15. W. Stöber, A. Fink, and E. Bohn, *J. Colloid Interface Sci.*, 1968, **26**, 62-69.
16. D. W. Lynch, W. R. Hunter, *Handbook of optical constants of solids*, Academic Press, 1985.
17. G. Jellison Jr, L. Boatner, J. Budai, B. S. Jeong, and D. Norton, *J. Appl. Phys.*, 2003, **93**, 9537-9541.
18. P. B. Johnson and R.W. Christy, *Phys. Rev. B*, 1972, **6**, 4370-4379.
19. E. Kazuma and T. Tatsuma, *Adv. Mater. Interfaces*, 2014, **1**, 1400066.
20. Y. Tian and T. Tatsuma, *J. Am. Chem. Soc.*, 2005, **127**, 7632-7637.
21. I. Tanabe and T. Tatsuma, *Nano Lett.*, 2012, **12**, 5418-5421.
22. E. Kazuma and T. Tatsuma, *Chem. Commun.*, 2012, **48**, 1733-1735.
23. K. Saito, I. Tanabe, and T. Tatsuma, *J. Phys. Chem. Lett.*, 2016, **7**, 4363-4368.
24. A. Sousa-Castillo, M. Comesaña-Hermo, B. Rodríguez-González, M. Pérez-Lorenzo, Z. Wang, X. T. Kong, A. O. Govorov, and M. A. Correa-Duarte, *J. Phys. Chem. C*, 2016, **120**, 11690-11699.
25. J. Turkevich, P. C. Stevenson, and J. Hillier, *Discuss. Faraday Soc.*, 1951, **11**, 55-75.
26. H. Nishi, T. Torimoto, and T. Tatsuma, *Phys. Chem. Chem. Phys.*, 2015, **17**, 4042-4046.
27. M. W. Knight, H. Sobhani, P. Nordlander, and N. J. Halas, *Science*, 2011, **332**, 702-704.
28. G. D. Moon, T. I. Lee, B. Kim, G. Chae, J. Kim, S. Kim, J.-M. Myoung, and U. Jeong, *ACS Nano*, 2011, **5**, 8600-8612.
29. C. Farcau, E. Vinteler, and S. Astilean, *J. Optoelectron. Adv. Mater.*, 2008, **10**, 3165-3168.
30. Z. Yi, G. Niu, J. Luo, X. Kang, W. Yao, W. Zhang, Y. Yi, Y. Yi, X. Ye, T. Duan, and Y. Tang,

Sci. Rep., 2016, **6**, 32314.

31. W. Du, Z. Yan, P. Gu, L. Tu, E. You, P. Zhan, and Z. Wang, *Appl. Phys. A*, 2015, **120**, 11-16.
32. A. I. Maaroof, M. B. Cortie, N. Harris, and L. Wieczorek, *Small*, 2008, **4**, 2292-2299.
33. M. Cortie and M. Ford, *Nanotechnology*, 2007, **18**, 235704.

Chapter 3 Solid-State Photovoltaic Cells with Plasmonic Metal Halfshell Arrays

3.1 Introduction

Because PICS causes electron deficiency in plasmonic metal nanostructures due to electron transfer to TiO_2, illuminated Ag and Cu nanoparticles (NPs) on TiO_2 are oxidized to ions in humid air or a solution.[1,2] Therefore, PICS-based wet photoelectrochemical cells have been developed using chemically stable Au as a light absorber. This is also the case for the metal halfshell arrays in the last chapter. For instance, when Ag was deposited on the SiO_2@TiO_2 colloidal crystal (diameter: ca. 370 nm) instead of Au (thickness: 55 nm), the Ag halfshell array was dissolved into an aqueous electrolyte after light irradiation as shown in (Figure 3.1a), leading to a rapid loss of plasmonic capability.

To maintain a long-term stability of the plasmonic halfshell arrays, solid-state photovoltaic cells are designed by taking advantage of their two-dimensional (2D) structure. The cross-sectional structure of the cell is shown in Figure 3.1b. The metal halfshell array serves not only as a light absorber but also as a current collector (*i.e.* counter electrode), resulting in a simpler structure of the solid-state cell. Since the continuous film structure has lower surface area to volume ratio than isolated metal NPs, it is expected that the halfshell arrays keep their stability even under exposure to ambient atmosphere. In comparison with the previously reported cells using dispersed metal NPs as light absorbers (Figure 3.1c),[3-10] the cell with metal halfshell array (denoted as metal halfshell cell for simplicity) would achieve excellent photovoltaic performance because of their broader light absorption, simpler construction structure, and better stability.

In this chapter, solid-state cells are prepared by depositing Au, Ag, or Cu onto SiO_2@TiO_2 colloidal crystals. The effects of TiO_2 thickness and hole transport layer (HTL) on the photovoltaic performance of Au halfshell cell are discussed. In addition, PICS behaviors of the Au halfshell cell are compared with those of Ag and Cu halfshell

cells.

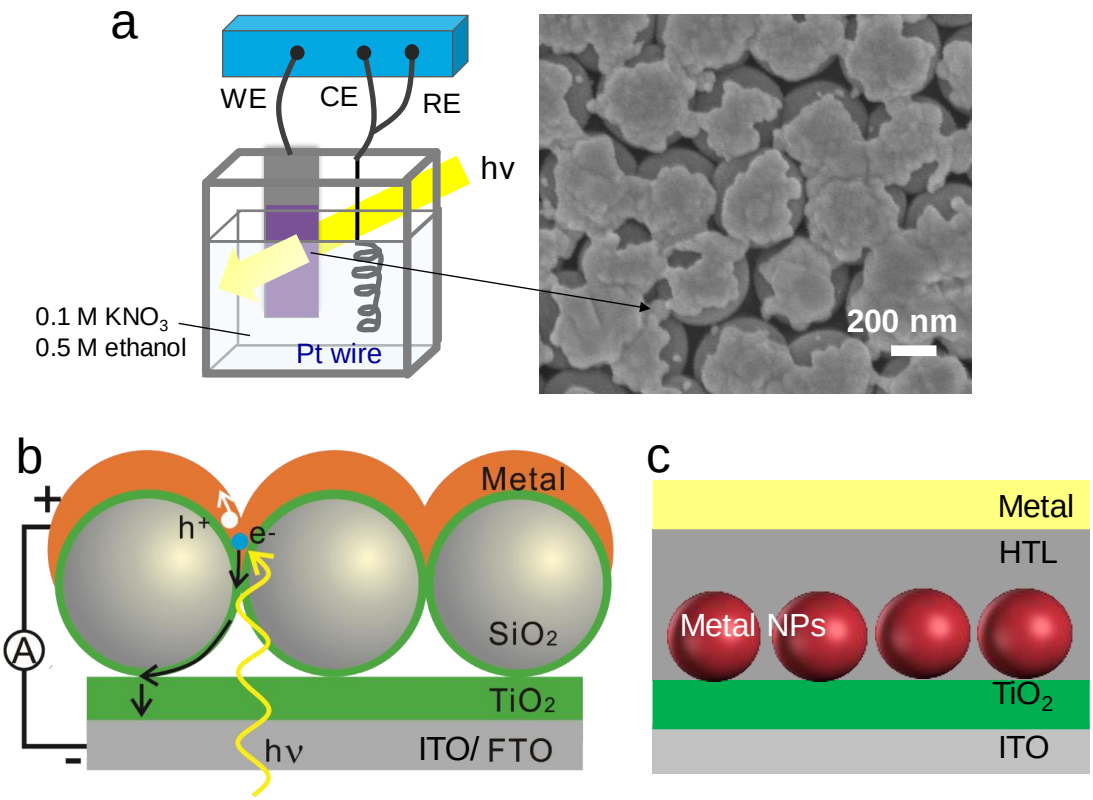

Figure 3.1 (a) Top-view SEM image of photoelectrode with Ag halfshell array after a 30-min short-circuit photocurrent measurement in 0.1 M aqueous KNO_3 containing 0.5 M ethanol. (b) Cross-sectional structure and working principle of a solid-state cell with a metal halfshell array. (c) Cross-sectional structure of a conventional solid-state cell with dispersed metal NPs.

3.2 Experimental Methods

3.2.1 Fabrication of Solid-State Cells

Indium tin oxide (ITO)- and (fluorine-doped tin oxide) FTO-coated glass plates (2.3 cm × 2.3 cm) were patterned utilizing aqua regia and a laser marker (YS-P20-SP, Sun Instruments), respectively. The patterned substrates (Figure 3.2) were sonicated in Milli-Q water, acetone, and 2-propanol successively. And then they were coated with a compact TiO_2 layer by the spray-pyrolysis method[11] and the surface was hydrophilized by UV-irradiation for 30 min as described in Chapter 2. 2D SiO_2 colloidal crystals were

prepared by spin-coating or air-water interface assembly[12] described in Chapter 2 and coated with TiO_2 by the spray-pyrolysis method (1s × 2, 4 or 6 times). The photovoltaic cell with 155-nm-thick metal (Au, Ag, or Cu) halfshell arrays was finally obtained by evaporating the metal (0.3 nm s^{-1}, <0.4 mPa) onto the SiO_2@TiO_2 colloidal crystals.

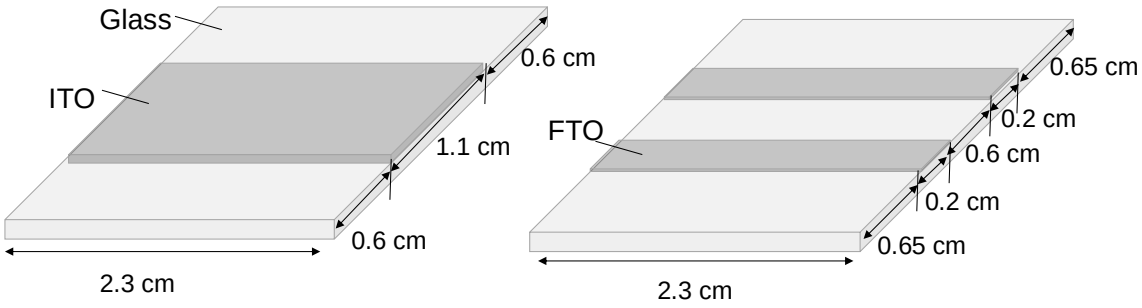

Figure 3.2 Schematic illustration for the patterned ITO and FTO glass plates.

The Au cells with HTL were also fabricated. MoO_3 or 2,2′,7,7′- tetrakis(*N*,*N*-di-*p*-methoxyphenylamine)-9,9-spirobifluorene (Spiro-OMeTAD) was deposited on the Au halfshell array (thickness = 55 nm) and Au counter electrode (100 nm) was further evaporated on the HTL. The MoO_3 layer was prepared by thermal evaporation (0.03 nm s^{-1}, <0.4 mPa). The Spiro-OMeTAD layer was obtained by spin-coating a mixture (80 μL) at 2000 rpm for 30 s. The mixture was prepared by adding 4-*tert*-butyl pyridine (28.8 μL) and lithium bis(trifluoromethanesulfonyl)imide (Li-TFSI) solution (17.5 μL, prepared by dissolving 260 mg Li-TSFI in 500 μL acetonitrile) to Spiro-OMeTAD (72.3 mg) dissolved in chlorobenzene (1 mL).[13]

3.2.2 Characterization

The morphology of the photovoltaic cells was investigated by a field emission scanning electron microscope (SEM, JSM-7500FA, JEOL) and a transmission electron microscope (TEM, JEOL-2010F, JEOL). Their optical properties were measured by a spectrophotometer (V-670, JASCO) equipped with an integrating sphere.

3.2.3 Evaluation of Photovoltaic Performance

A potentiostat (SI 1280B, Solartron) was employed to evaluate the photovoltaic

performances. All of the devices were illuminated through the ITO or FTO electrode by a Xe lamp (LAX-103, Asahi Spectra) equipped with a long-pass filter (>460 or 440 nm, 100 mW cm^{-2}). Photocurrent action spectra were collected under monochromatic light irradiation (3.75×10^{15} or 5.0×10^{15} photons cm^{-2} s^{-1}) using the Xe lamp equipped with band-pass filters (FWHM = 10 nm) or an optospectrum generator (L12194-00-4343079, Hamamatsu Photonics, FWHM = 20 nm)

3.3 Results and Discussion

3.3.1 Effect of TiO_2 Thickness

(1) Morphologies of the prepared arrays

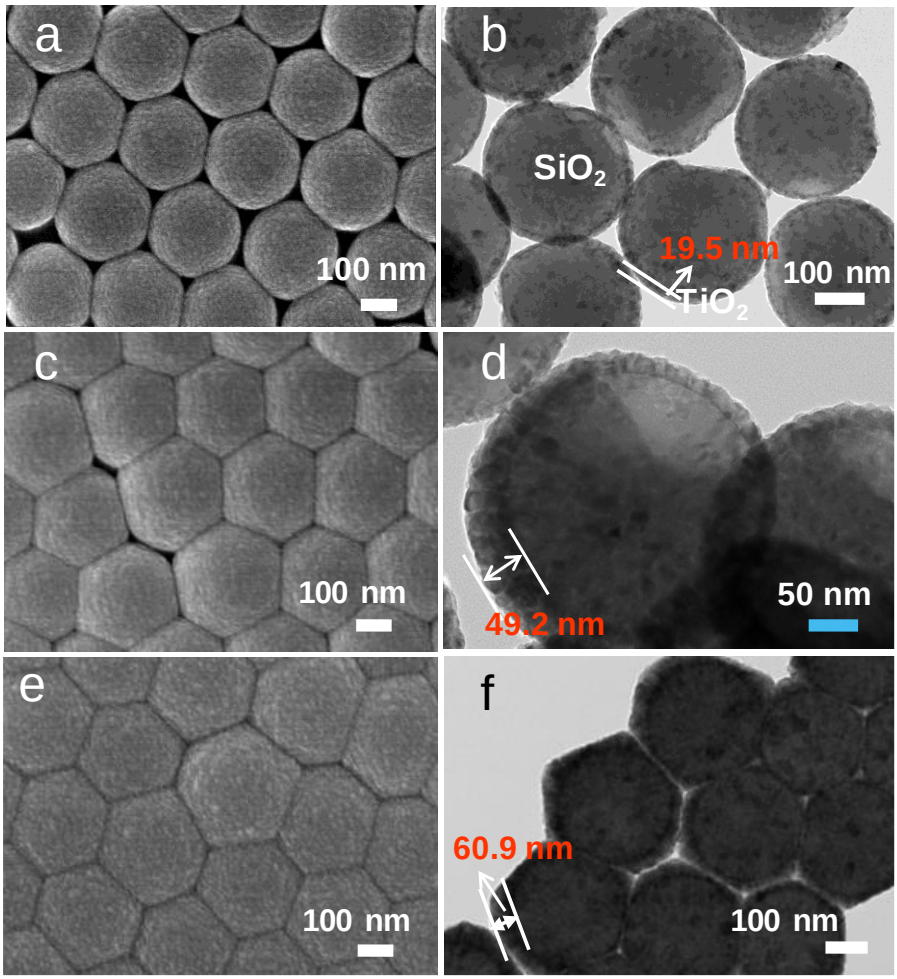

Figure 3.3 (a, c, e) SEM and (b, d, f) TEM images of 2D SiO_2@TiO_2 colloidal crystals with different TiO_2 shell thicknesses.

SEM images of the prepared SiO_2@TiO_2 colloidal crystals are shown in Figure 3.3a, c, and e. SiO_2@TiO_2 spheres are arranged in a hexagonal close-packed structure and the interstitial spaces are fully filled by TiO_2 when the spray-coating cycle is 6 (Figure 3.3e). The TEM images of the spheres (Figure 3.3b, d, and f) demonstrated that the thicknesses of TiO_2 shell fabricated by 2-, 4-, and 6-times spray-coating were increased from ca. 20 nm to 61 nm.

The structure of Au halfshell cell is shown in Figure 3.4a. Four devices (4.5 × 2 mm) are on one substrate (2.3 × 2.3 cm). Figure 3.4b depicts the photographs of the prepared cells with TiO_2 shells of different thicknesses. The cells with 20-, 49-, and 61 nm-thick TiO_2 are denoted as cell-2, cell-4, and cell-6, respectively. It was clearly observed that the Au halfshell arrays showed different reflection colors with the increase of TiO_2 thickness, owing to the diverse structural parameters of the underlying SiO_2@TiO_2 colloidal crystals.

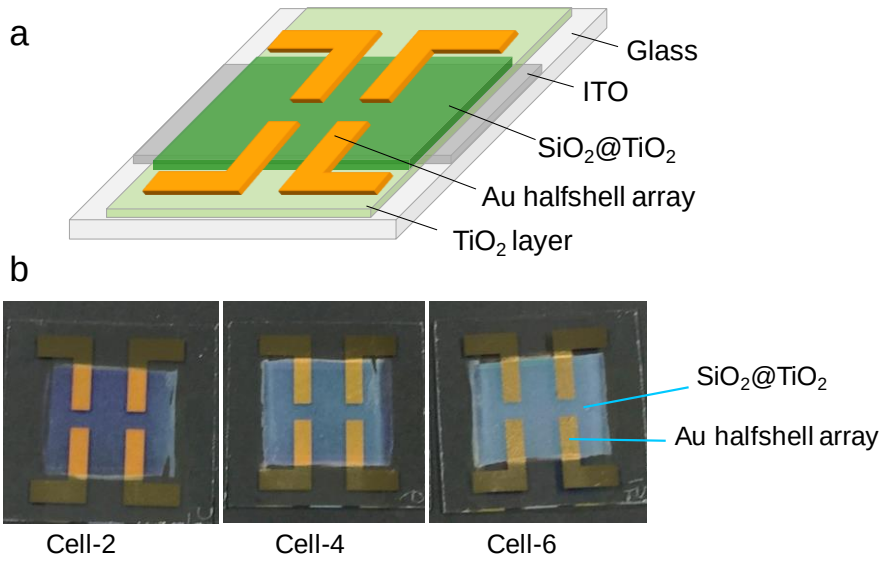

Figure 3.4 (a) Schematic illustration for the structure of Au halfshell cell. (b) Photographs of the prepared cell-2, cell-4, and cell-6.

The SEM images of the prepared Au halfshell cells are shown in Figure 3.5a–f. The device is composed of Au halfshells (thickness: 155 nm), SiO_2@TiO_2 monolayer

(SiO_2 diameter: 300 nm), compact TiO_2 layer (thickness: 40 nm), and ITO electrode, indicating successful fabrication of the designed photovoltaic cell (Figure 3.1b). As can be seen from the top-view SEM images (Figure 3.5d−f), the hexagonal structure still is remained after Au deposition. The halfshells were deposited as a continuous metallic film, which works both as a light absorber and as a counter electrode for collection of positive charges.

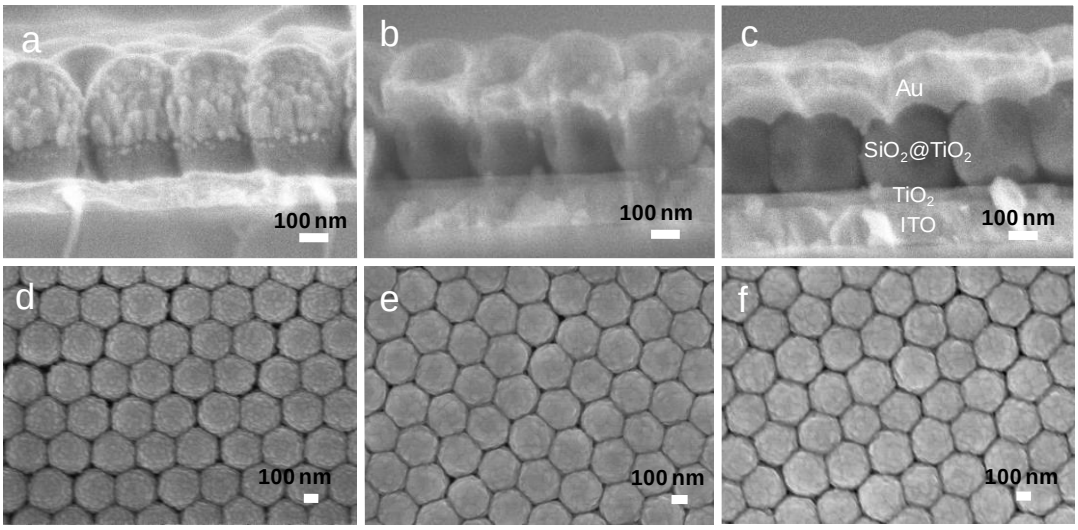

Figure 3.5 (a−c) Cross-sectional and (d−f) side-view SEM images of (c, f) cell-2, (d, g) cell-4, and (e, h) cell-6.

(2) Dependence of photovoltaic properties on TiO_2 thickness

Photovoltaic performances of the prepared Au halfshell cells were examined. In the dark, the cells showed good rectification behavior, indicating that the Au-TiO_2 interface forms a Schottky junction as shown in Figure 3.6a. Under light irradiation (>460 nm), open-circuit photovoltage (V_{oc}) and short-circuit photocurrent (J_{sc}) were generated (Figure 3.6b). The photoresponses of these devices arise exclusively from the PICS at the interface between Au halfshell and TiO_2 shell. Upon light illumination, electrons excited by the plasmonic absorption of Au halfshell array are injected to the conduction band of TiO_2 and flow to the ITO electrode, while positive charges are left in the Au halfshell array electrode (Figure 3.1b). The Au halfshell array thus serves not

only as a light absorber but also a current collector. The J_{sc} of the cells was also measured under intermittent light irradiation (Figure 3.6c). The J_{sc} values went down to zero right after turning off the light and came back immediately to the original values upon photoirradiation. Those photoresponses were highly reproducible.

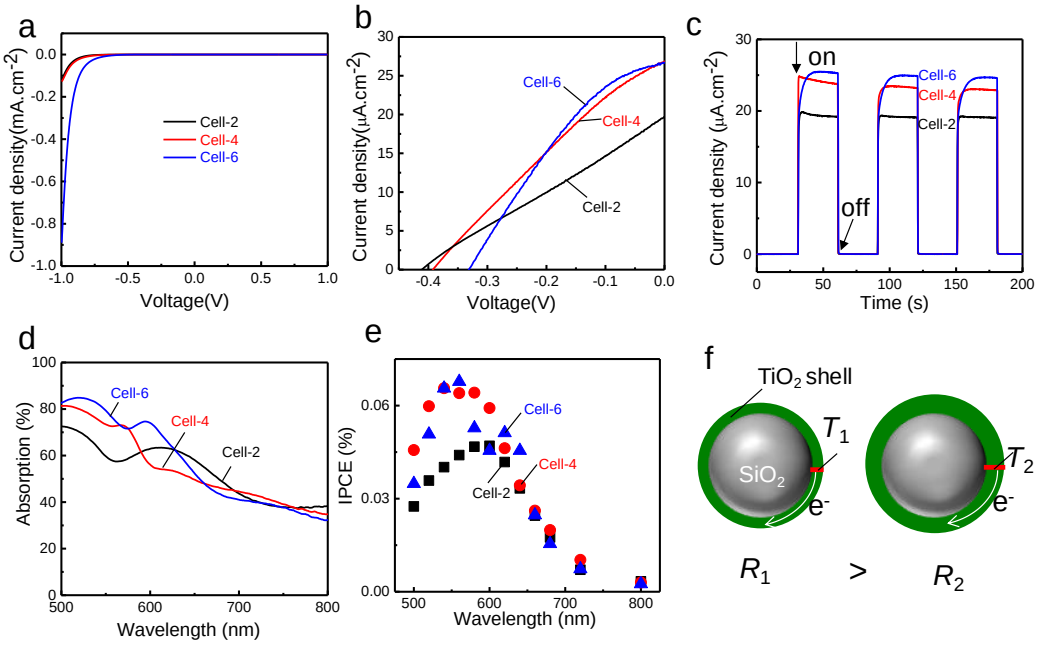

Figure 3.6 *J–V* characteristics measured (a) without and (b) with light irradiation, (c) short-circuit photocurrent responses of cell-2, -4, and -6 (>460 nm, 100 mW cm^{-2}). (d) Absorption spectra and (e) IPCE spectra of the cells. Light was illuminated from ITO side. (f) Scheme illustrating the decrease of series resistance with the increase of thickness of TiO_2 shell. R_1, R_2 are the series resistance of thin (thickness: T_1) and thick (thickness: T_2) TiO_2 shell, respectively.

The absorption spectra of the cells, calculated from transmittance (T) and reflectance (R) according to an equation A (%) = 100 – T – R, are presented in Figure 3.6d. The Au cells showed intensive and broad absorption in the visible and near infrared (NIR) regions, which results in broad photoresponses (Figure 3.6e). As discussed in Chapter 2, the shapes of IPCE spectra are not in good accordance with those of the absorption spectra because of low PICS efficiency in the NIR range.[4] Figure 3.5 indicates a thicker TiO_2 shell is advantageous for generation of higher photocurrents. This may be explained in terms of lower series resistance which can be determined from

the reciprocal of the slope of the $J-V$ curve at V_{oc}. The series resistance (R) of the TiO_2 shell is described as $R = \rho l/A$, where ρ is the resistivity of TiO_2, l is the pathway length of electron, and A is the cross-section area. Here, A means the thickness of the TiO_2 shell according to the direction of electron transport. As illustrated in Figure 3.6f, assuming that R_1, R_2 are the resistance of thin (thickness: T_1) and thick (thickness: T_2) TiO_2 shell, respectively, it can be concluded that the increase of thickness of TiO_2 shell ($T_1<T_2$) results in the decrease of series resistance ($R_1>R_2$).

3.3.2 Effect of Introduction of HTL

Although photovoltages and photocurrents derived from PICS were detected in the Au halfshell cells, the power conversion efficiency (PCE = $J_{sc}V_{oc}$FF/$P_{in,}$ where FF is fill factor and P_{in} is input photoenergy) were very low (0.0026%, see Table 3.1). In this section, HTLs (MoO_3 or Spiro-OMeTAD) are introduced to the Au halfshell cell to improve PCE.

Table 3.1 Performances of the cells without and with HTLs.

Cells	J_{sc} (A cm^{-2})	V_{oc} (V)	FF	PCE (%)	IPCE (%)
ITO/TiO_2/Au	25.0	0.36	0.28	0.0026	0.070 (540 nm)
ITO/TiO_2/Au/MoO_3-5 nm/Au	36.4	0.35	0.30	0.0038	0.096 (540 nm)
ITO/TiO_2/Au/MoO_3-10 nm/Au	40.8	0.32	0.30	0.0040	0.093 (540 nm)
ITO/TiO_2/Au/MoO_3-15 nm/Au	23.5	0.34	0.28	0.0022	0.043 (560nm)
ITO/TiO_2/Au/Spiro-OMeTAD/Au	27.2	0.31	0.46	0.0039	0.070 (560 nm)

(1) MoO_3 as HTL

Figure 3.7a shows structure of the photovoltaic cell with MoO_3 as HTL. The MoO_3 layer was inserted into the Au halfshell array. Here, the top Au halfshell array works as a counter electrode and the inner one works as a light absorber. The cross-sectional SEM images (Figure 3.7b–d) reveal that the cell is composed of an ITO electrode, a compact TiO_2 film (thickness: 60 nm), a SiO_2@TiO_2 monolayer (SiO_2 diameter: 300 nm), an inner Au halfshell (thickness: 55 nm), a MoO_3 film (thickness: 5–15 nm), and a top Au halfshell (thickness: 100 nm). The top-view SEM images (Figure 3.7 e–g) show that the morphology of the cell is similar to that without MoO_3 (Figure 3.5e).

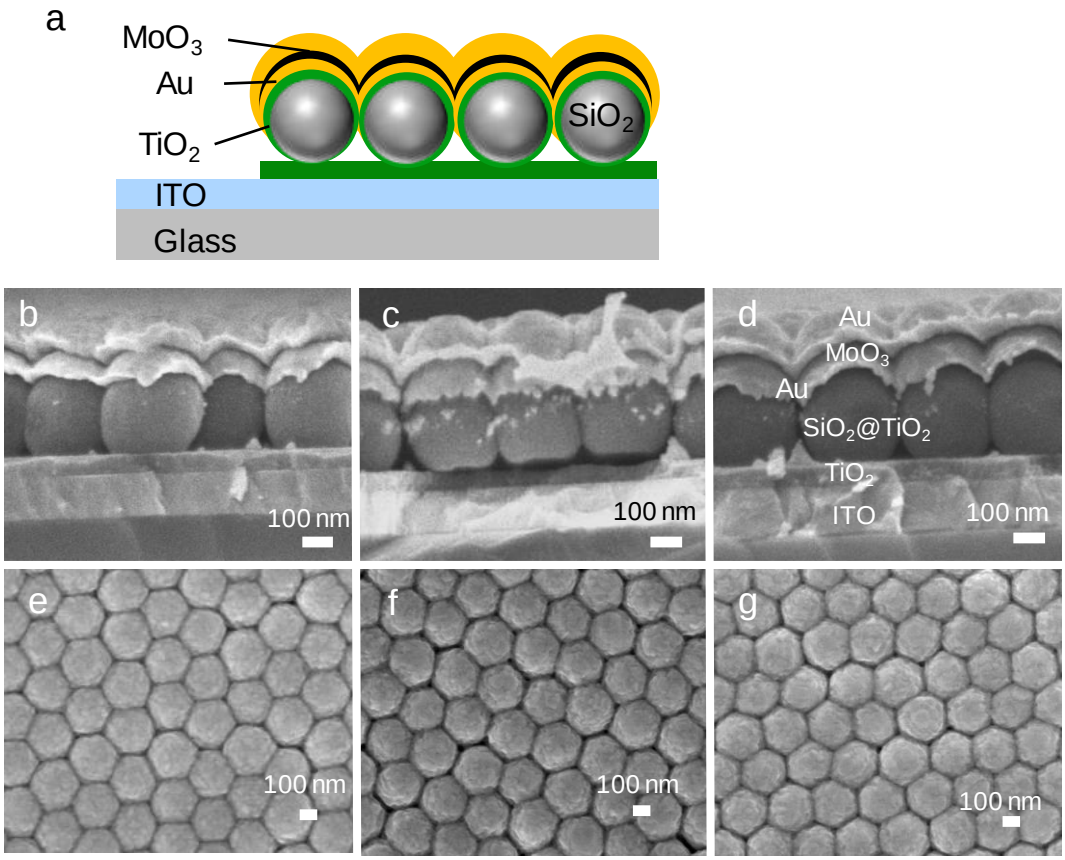

Figure 3.7 (a) Schematic illustration of cross-sectional structure of the Au halfshell cell with MoO_3 as HTL. (b–d) Top-view and (e–g) cross-sectional SEM images of the cells with different MoO_3 thicknesses: (b, e) 5 nm, (c, f) 10 nm, and (d, g) 15 nm.

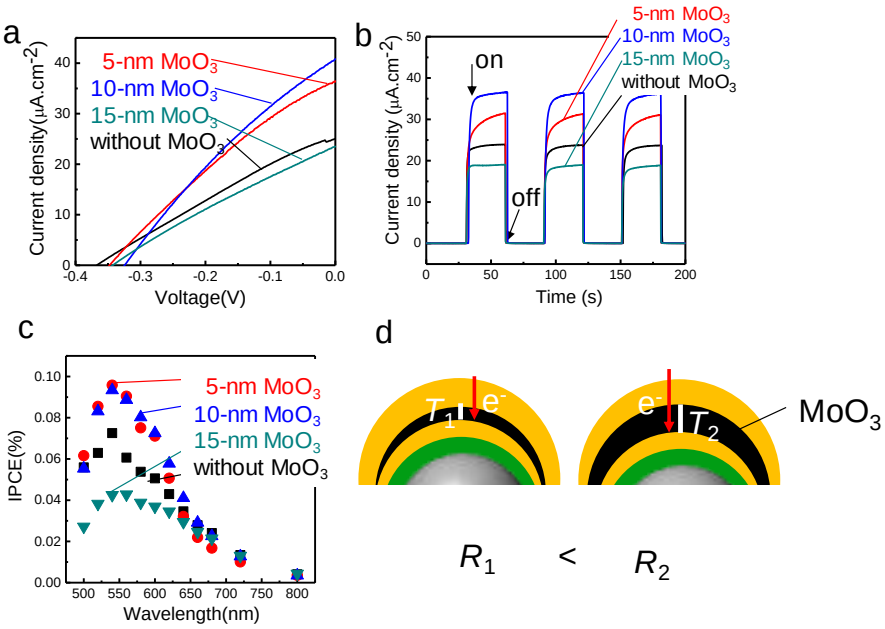

Figure 3.8 (a) *J*–*V* characteristics measured under light irradiation (>460 nm, 100 mW cm^{-2}), (b) short-circuit photocurrent responses, and (c) IPCE spectra of the cells with MoO_3 as HTL. Light was illuminated from ITO side. The thickness of the Au halfshell in the reference cell without MoO_3 is 55 nm. (d) Scheme illustrating the decrease of series resistance with the increase of thickness of MoO_3 layer. R_1, R_2 are the series resistance of thin (thickness: T_1) and thick (thickness: T_2) MoO_3 layer, respectively.

Photovoltaic performances of the cells without and with MoO_3 were shown in Figure 3.8. Similar to the cell without MoO_3, the cells with MoO_3 generated open-circuit photovoltage and short-circuit photocurrent (Figure 3.8a.), which can be explained as follows. The inner Au halfshell array absorbs light and generates electron-hole pairs. The electrons are injected into the TiO_2 shell as is the case for the cell without MoO_3, whereas holes are transported efficiently to the outer Au halfshell array (counter electrode) through the MoO_3 layer. It can also be seen from Figure 3.8a that introduction of a 5- or 10-nm-thick MoO_3 layer results in an increase of J_{sc} in comparison with the reference cell without MoO_3. This result was further demonstrated by J_{sc} responses under intermittent light irradiation (Figure 3.8b). Because the HTL has high hole

mobility and prevents electron transport, an efficient charge separation (higher J_{sc}) was realized by introducing MoO_3. This explanation is supported by an early report on PICS using p-NiO_x as HTL.[14] On the other hand, the increase J_{sc} of the cell may also be attributed to the top Au halfshell array which produces strong optical near field to enhance the photocurrent generation of the inner Au halfshell array. However, the thicker MoO_3 layer (15 nm) caused a decrease in J_{sc}, due to high series resistance determined from the reciprocal of the slope of the J−V curve at V_{oc}. As mentioned above, the series resistance (R) of the MoO_3 layer can be described as $R = \rho l/A$. It should be noted that l means the thickness of the MoO_3 layer in this case. As illustrated in Figure 3.8d, assuming that R_1, R_2 are the resistance of thin (thickness: T_1) and thick (thickness: T_2) MoO_3 layer, respectively, it can be concluded that the increase of thickness of MoO_3 layer ($T_1<T_2$) results in the decrease of series resistance ($R_1<R_2$).

The J_{sc}, V_{oc}, FF, and PCE calculated from J−V characteristics are summarized in Table 3.1. The increase of J_{sc} results in improvement of PCE from 0.0026% to 0.0040%. The IPCE spectra of the cells without and with MoO_3 are depicted in Figure 3.8c. It can be seen that all the cells show broad photoresponses in the wavelength range of 440−780 nm. The maximum IPCE values are also summarized in Table 3.1.

(2) Spiro-OMeTAD as HTL

The structure of the cell with Spiro-OMeTAD (Figure 3.9b) as HTL is presented in Figure 3.9a. The cross-sectional SEM image (Figure 3.9c) shows that a Au halfshell layer (thickness: 55 nm), a Spiro-OMeTAD layer (thickness: ca. 180 nm), and a flat Au film (thickness: 100 nm) are on the SiO_2@TiO_2 template. As can be seen from the top-view SEM image (Figure 3.9d), the flat Au film is composed of interconnected Au NPs. The J−V characteristics of the cell is shown in Figure 3.9e. For the cell with Spiro-OMeTAD, the performance was predominantly improved by increase of FF. This is possibly because the thick Spiro-OMeTAD layer prevents the short-circuit of the device at the sites of structural defects, thereby leading to an increase in shunt resistance (the reciprocal of the slope of the J−V curve at 0 V). The PCE values of the cells with and without Spiro-OMeTAD were 0.0026% and 0.0039%, respectively, as shown in Table

3.1. The IPCE spectra of the cells were presented in Figure 3.9f. The photoresponses are similar to those of other Au halfshell cells prepared in this thesis.

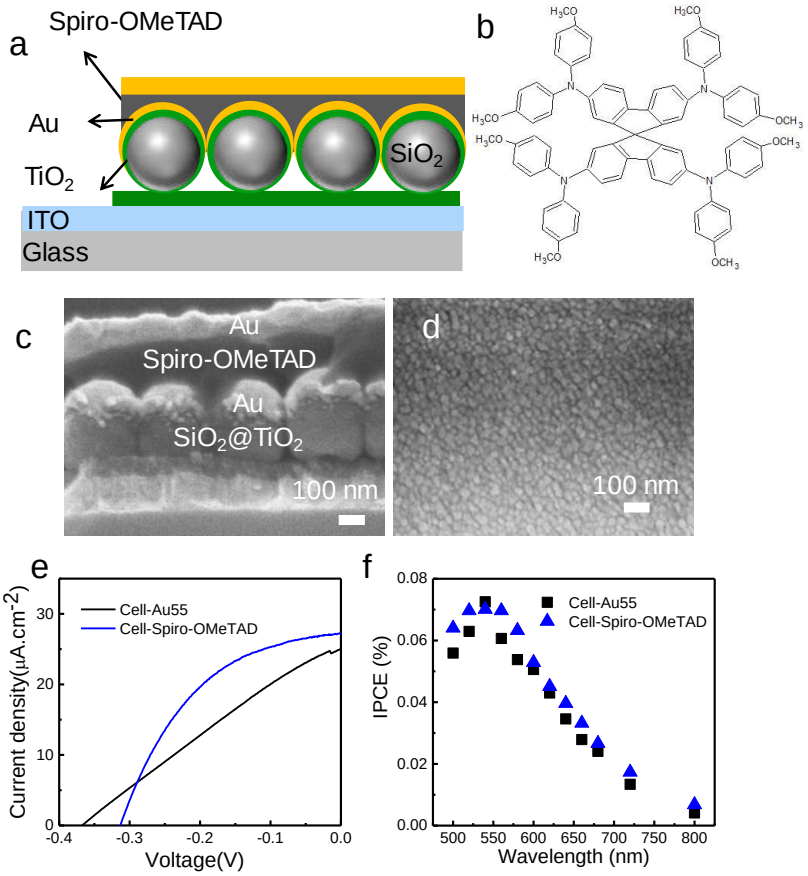

Figure 3.9 (a) Schematic illustration of cross-sectional structure of the Au halfshell cell with Spiro-OMeTAD as HTL. (b) Structural formula of Spiro-OMeTAD. (c) Cross-sectional and (d) top-view SEM images, (e) *J*–*V* characteristics measured under light irradiation (>460 nm, 100 mW cm^{-2}), and (f) IPCE spectra of the cells. Light was illuminated from ITO side.

3.3.3 Cells with Ag and Cu Halfshell Arrays

(1) Morphologies of the cells

In addition to the Au halfshell cell, Ag and Cu halfshell cells were also fabricated. The structure of the metal halfshell cell is shown in Figure 3.10a. Four devices (2 × 2 mm) are on one substrate (2.3 × 2.3 cm). Photographs of the prepared cells are presented in Figure 3.10b. The reflection colors depend on the constituent metal of the halfshell.

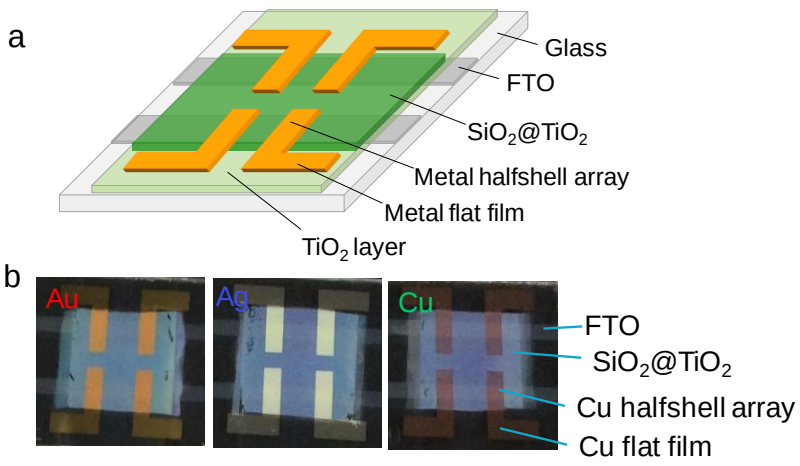

Figure 3.10 (a) Schematic illustration for the structure of metal halfshell cells. (b) Photographs of the prepared photovoltaic cells.

The SEM images of the resulting devices are shown in Figure 3.11. All of the cells showed similar morphology, indicating that various metal halfshell cells can be fabricated by the same procedure just changing the evaporation source.

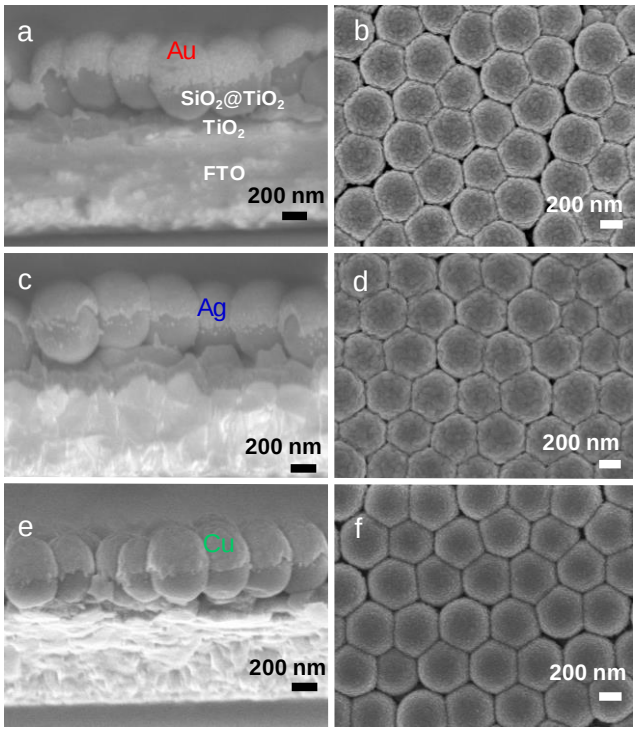

Figure 3.11 (a, c, e) Cross-sectional and (b, d, f) top-view SEM images of the (a, b) Au, (c, d) Ag, and (e, f) Cu halfshell cells.

(2) Photovoltaic performances

The *J*–*V* characteristics under light irradiation (>440 nm, 100 mW cm^{-2}) are depicted in Figure 3.12a and V_{oc}, J_{sc}, FF, and PCE are summarized in Table 3.2. The performance is clearly dependent on the composition of metal halfshell. Compared with the Au and Cu halfshell cells, the Ag one showed higher V_{oc}, J_{sc}, and FF. The dependence was also confirmed by V_{oc} and J_{sc} measurements upon intermittent light irradiation (Figure 3.12b and c). All the cells exhibited the same polarity. The FTO electrode and the metal halfshell (*i.e.* counter electrode) showed negative and positive potential shifts under light irradiation, respectively (Figure 3.12b). Under short-circuit condition, electrons flow out of the FTO electrode and into the halfshell electrode (Figure 3.12c). Remarkably, the Ag halfshell cell achieved the highest PCE (0.112%) among the reported solid-state PICS devices (Table 1.1 in Chapter 1), which could be attributed to the broad-band absorption of the metal halfshell array and the simple construction of the device.

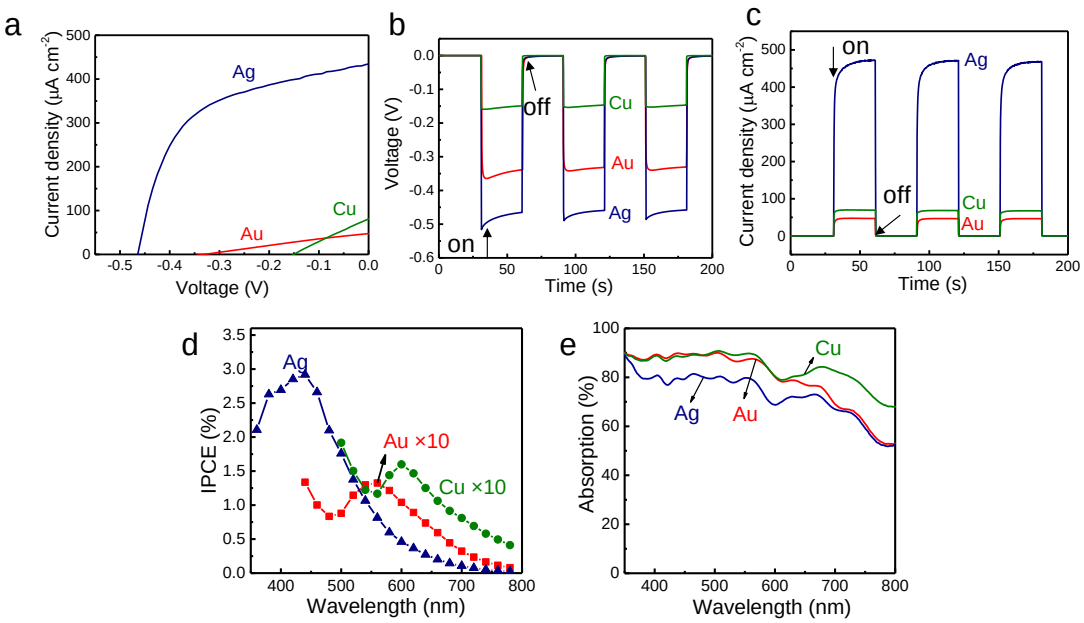

Figure 3.12 (a) *J*–*V* characteristics, (b) open-circuit photovoltage, and (c) short-circuit photocurrent responses of Au, Ag, and Cu halfshell cells under light irradiation (>440 nm, 100 mW cm^{-2}). (d) Absorption spectra and (e) IPCE spectra of the cells. Light was illuminated from FTO side.

The absorption spectra of the halfshell cells are presented in Figure 3.12d. As is the case for Au halfshell cells, the Ag and Cu ones exhibited intense and broad absorption in the visible and NIR regions. Figure 3.12e shows typical IPCE action spectra of the cells. Again, the Ag halfshell cell exhibited the maximum IPCE of 2.92% at 440 nm, which is much higher than that of Au (0.13% at 560 nm) or Cu (0.16% at 600 nm) ones (Table 3.2). However, even though the Au and Cu half shells exhibit similarly high absorption (80%−90%), the maximum IPCE values vary from 0.13 to 2.92% by about 22 times. This is explained mainly in terms of the difference in Schottky barrier height E_{SB} and interband transition energy.

Table 3.2 Performances of the cells with different metal halfshell arrays.

Cells	J_{sc} (A cm^{-2})	V_{oc} (V)	FF	PCE (%)	IPCE (%)
FTO/TiO_2/Au	47.5	0.33	0.27	0.0043	0.13 (560nm)
FTO/TiO_2/Ag	434	0.47	0.55	0.112	2.92 (440 nm)
FTO/TiO_2/Cu	81.0	0.15	0.26	0.0032	0.16 (600 nm)

(3) Differences in metal species and the efficiency

In the case of metal-TiO_2 contact, E_{SB} is determined by the equation $E_{SB} = W_m - \chi_s$, where W_m is the work function of a metal and χ_s is the electron affinity of TiO_2. Quantum efficiency η of an external photoelectric effect has been formulated on the basis of the modified Fowler's equation $\eta = k(h\nu - E_{SB})^2$,[15, 16] where k is a constant. If the equation holds, the ratios η_{Ag}/η_{Au} and η_{Cu}/η_{Au} (subscripts represent metal species) are determined to be 5.9 and 1.7, respectively, assuming that the χ_s of anatase TiO_2 is 3.9 eV,[17] the W_m of Au, Ag, and Cu are 5.1, 4.26, and 4.65 eV, respectively,[18] and k is independent of the metal species. Although the calculated η_{Cu}/η_{Au} value is close to the experimental one ($0.16/0.13 \approx 1.2$), that of η_{Ag}/η_{Au} is much lower than the experimental one ($2.92/0.13 \approx 22$).

Actually, the *k* value should be affected by various factors. One possible factor is interband transition in the metals which does not contribute to surface plasmon excitation. Upon light irradiation, electrons in the Ag halfshell array are excited only through intraband transition (within the sp band) indicated by the black arrow in Figure 3.13a. In this case, interband transition (from the d band to sp band) does not occur because there is too large energy difference (3.7 eV) between the d band and the Fermi level. As a result, energetic electrons are generated via the intraband transition and overcome the Schottky barrier to realize the charge separation. With regard to Au and Cu halfshell arrays, however, interband transition, as shown by the red arrow in Figure 3.13b, takes place simultaneously with the plasmon excitation because of the relatively small energy difference between the d band and the Fermi level (2.3 eV for Au and 2.1 eV for Cu). The interband transition produces electrons with lower energies which cannot contribute to the uphill electron transfer, indicating that *k* value for Ag halfshell cell should be higher than that for Au and Cu ones. Therefore, it is reasonable to think that the 22-times higher IPCE for Ag halfshell is derived from difference both in *k* and E_{SB}.

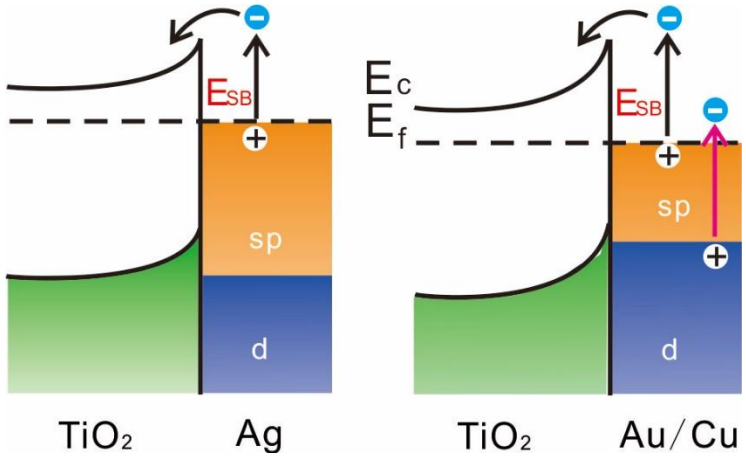

Figure 3.13 Band structures and PICS mechanisms at the metal-TiO_2 interface.

(4) Stability of the cells

The stability of the solid-state Au, Ag, and Cu halfshell cells were also investigated. The J_{sc} of the metal halfshell cell was recorded during long-term light irradiation (>440

nm, 100 mW cm^{-2}) as shown in Figure 3.14a. All the cells showed a slight photocurrent increase in the initial few hours. This is may be due to a temperature increase in the cells. The Au and Cu halfshell cells showed good stabilities and maintained their PICS capabilities. Both halfshell structures remained unchanged even after light irradiation for 24 h, as can be seen from Figure 3.14b and d. The Ag halfshell cell suffered from a photocurrent decrease by 21% after the initial increase. However, the decrease is much smaller than that reported for the solid-state cell using Ag NPs (a 42% decrease after 20-h light irradiation).[6] Ag NPs on TiO_2 are known to be oxidized to Ag^+ based on PICS in a humid air.[1] The Ag halfshell array on TiO_2 is also dissolved in an aqueous electrolyte after 30-min irradiation (Figure 3.1a). The photocurrent drop of the Ag halfshell cell in air could thus be ascribed to the PICS-based oxidation of Ag, although no observable morphological changes can be seen from the SEM image (Figure 3.14c). This issue would be suppressed by sealing the device tightly.

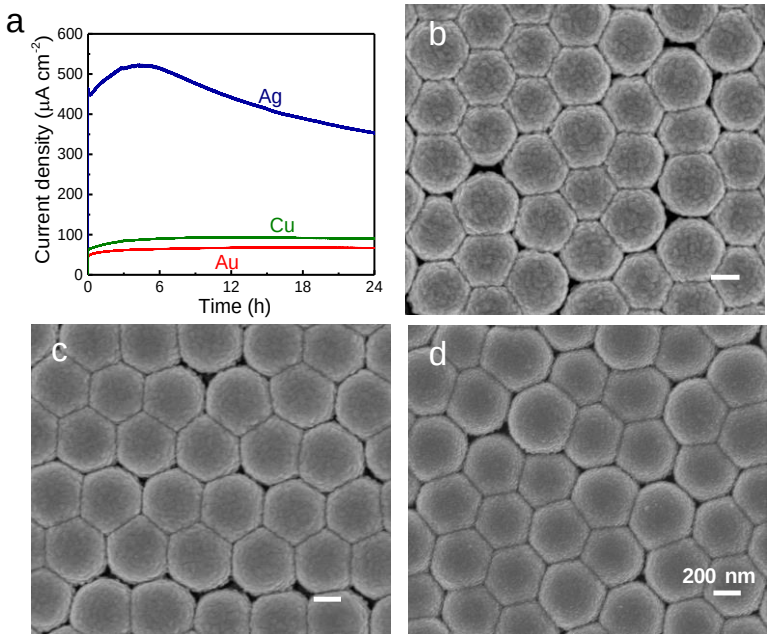

Figure 3.14 (a) Time-courses of the short-circuit photocurrents of the Au. Ag, and Cu halfshell cells under light irradiation (>440 nm, 100 mW cm^{-2}). SEM images of the (b) Au, (c) Ag, and (d) Cu halfshell cells after a 24-h photocurrent measurement. All scale bars are 200 nm.

3.4 Conclusions

In summary, solid-state PICS photovoltaic cells were developed by taking advantage of the interconnected Au, Ag, and Cu halfshell arrays, which serve both as light absorbers and current collectors. A thick TiO_2 shell was advantageous for generation of higher photocurrents due to low series resistance. The cell performance was further improved by introducing MoO_3 or Spiro-OMeTAD as a HTL. The structure differences make the cell performance improved by different mechanisms. Compared with the Au and Cu halfshell cells, the Ag halfshell cell showed much higher photovoltaic performance due to the lower Schottky barrier height E_{SB} and higher interband transition energy. Remarkably, the highest PCE of 0.112% was achieved among the previously reported solid-state PICS cells. The high cell performance is likely due to the broad-band absorption, simple structure and good stability. This work may deepen the study of PICS and open a pathway for enhancing photovoltaic performance of plasmonic solid-state cell.

3.5 References

1. K. Naoi, Y. Ohko, and T. Tatsuma, *J. Am. Chem. Soc.*, 2004, **126**, 3664-3668.
2. S. Panigrahi, S. Kundu, S. K. Ghosh, S. Nath, S. Praharaj, S. Basu, and T. Pal, *Polyhedron*, 2006, **25**, 1263-1269.
3. K. Yu, N. Sakai and T. Tatsuma, *Electrochemistry*, 2008, **76**, 161-164.
4. M. W. Knight, H. Sobhani, P. Nordlander, and N. J. Halas, *Science*, 2011, **332**, 702-704.
5. Y. Takahashi and T. Tatsuma, *Appl. Phys. Lett.*, 2011, **99**, 182110.
6. P. Reineck, G. P. Lee, D. Brick, M. Karg, P. Mulvaney, and U. Bach, *Adv. Mater.*, 2012, **24**, 4750-4755.
7. F. P. García de Arquer, A. Mihi, D. Kufer, and G. Konstantatos, *ACS Nano*, 2013, **7**, 3581-3588.
8. S. Mubeen, J. Lee, W. R. Lee, N. Singh, G. D. Stucky, and M. Moskovits, *ACS Nano*, 2014, **8**, 6066-6073.
9. K. Nakamura, T. Oshikiri, K. Ueno, Y. M. Wang, Y. Kamata, Y. Kotake, and H. Misawa, *J. Phys. Chem. Lett.*, 2016, **7**, 1004-1009.

10. P. Reineck, D. Brick, P. Mulvaney, and U. Bach, *J. Phys. Chem. Lett.*, 2016, **7**, 4137-4141.
11. T. Kawawaki, Y. Takahashi, and T. Tatsuma, *Nanoscale*, 2011, **3**, 2865-2867.
12. K. Sugawa, T. Tamura, H. Tahara, D. Yamaguchi, T. Akiyama, J. Otsuki, Y. Kusaka, N. Fukuda, and H. Ushijima, *ACS Nano*, 2013, **7**, 9997-10010.
13. X. Chen, S. Yang, Y. C. Zheng, Y. Chen, Y. Hou, X. H. Yang, and H. G. Yang, *Adv. Sci.* 2015, **2**, 1500105.
14. H. Robatjazi, S. M. Bahauddin, C. Doiron, and I. Thomann, *Nano Lett.*, 2015, **15**, 6155-6161.
15. A. Giugni, B. Torre, A. Toma, M. Francardi, M. Malerba, A. Alabastri, R. P. Zaccaria, M. I. Stockman, and E. Di Fabrizio, *Nat. Nanotechnol.*, 2013, **8**, 845-852.
16. A. V. Uskov, I. E. Protsenko, R. S. Ikhsanov, V. E. Babicheva, S. V. Zhukovsky, A. V. Lavrinenko, E. P. O'Reilly, and H. Xu, *Nanoscale*, 2014, **6**, 4716-4727.
17. R. Könenkamp, *Phys. Rev. B*, 2000, **61**, 11057.
18. H. B. Michaelson, *J. Appl. Phys.*, 1977, **48**, 4729-4733.

Chapter 4 Periodic Au Nanodisks and Nanoholes on TiO_2 for Localized Surface Plasmon Resonance Sensors and Plasmon-Induced Charge Separation

4.1 Introduction

As described in the previous chapters, ordered metal nanostructures are of particular interest for various applications such as sensing,[1,2] PICS[3,4], and surface enhanced Raman spectroscopy (SERS),[5-7] because of good controllability and reproducibility. However, time-consuming and costly techniques, focused-ion-beam milling (FIB),[8] photolithography,[9] and electron beam lithography (EBL),[10,11] are used for fabrication of such ordered nanostructures. Therefore, a simple and low-cost colloidal template technique has been exploited to prepare the two-dimensional (2D) metal halfshell arrays in Chapter 2 and 3. These arrays showed extensive absorption, high photoelectrochemical and photovoltaic responses in visible and near-infrared (NIR) range.

In this chapter, the colloidal template method is further used for fabrication of a variety of ordered plasmonic photoelectrodes. Au nanodisks and nanoholes are fabricated on the bottom and top of a TiO_2 nanohole array which is used as the template for Au deposition. Refractive index sensitivity and PICS behaviors of the prepared plasmonic nanostructure are investigated experimentally and computationally. Finally, future perspective of the template method is discussed and various TiO_2 templates that are potentially applicable to novel plasmonic nanostructures are fabricated.

4.2 Experimental Methods

4.2.1 Fabrication of Au Nanodisks and Nanoholes on TiO_2 Nanohole Array

As illustrated in Figure 4.1, Au nanodisks and nanoholes were fabricated by evaporating Au onto a TiO_2 nanohole array obtained using a polystyrene (PS) colloidal crystal. The details are as follows.

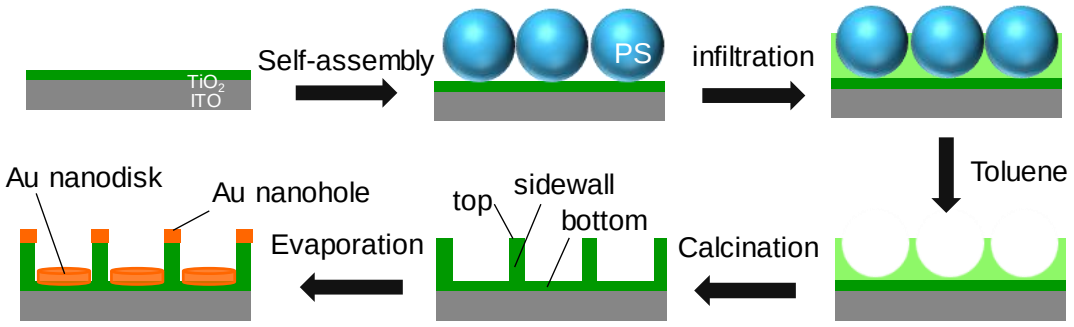

Figure 4.1 Schematic illustration for fabrication of electrodes with Au nanodisks and nanoholes on TiO_2. nanohole array.

(1) Preparation of TiO_2 sol

A mixture of water (529 μL), ethanol (99.5 vol%, 7.2 mL), and HNO_3 (63 wt%, 97.8 μL) was slowly added to a mixture of titanium butoxide (5 mL), ethanol (14.3 mL), and acetic acid (1.26 mL) and stirred for 2h at room temperature. The obtained sol was aged for 3h before use.

(2) Self-assembly of 2D PS array[12]

A glass plate (4.2 cm × 5 cm) was pretreated with O_2 plasma (PR 300, Yamato Scientific) at 100 W for 5 min (O_2 flow rate: 30 mL min^{-1}) to make the surface hydrophilic. A suspension of PS spheres (diameter = 500 nm, 10 wt%, Sigma Aldrich) was diluted twice with ethanol. The diluted suspension (100 μL) was spin-coated on the pretreated substrate at 1800 rpm for 60 s. The acceleration rate was set to 800 rpm s^{-1}. The obtained film was opaque as shown in Figure 4.2. Then, the film with PS spheres was slowly immersed into water containing sodium dodecyl sulfate (SDS, 2 wt%) in a 100-mL beaker. The PS spheres were self-assembled into a monolayer array at the air-water interface with the help of the SDS. Finally, the 2D PS array was transferred to a hydrophilic ITO/TiO_2 substrate (ITO = indium tin oxide) which was prepared by the same method in Chapter 2 (50-nm thick compact TiO_2 on a ITO-coated glass plate (1.2 cm × 4 cm).[13]

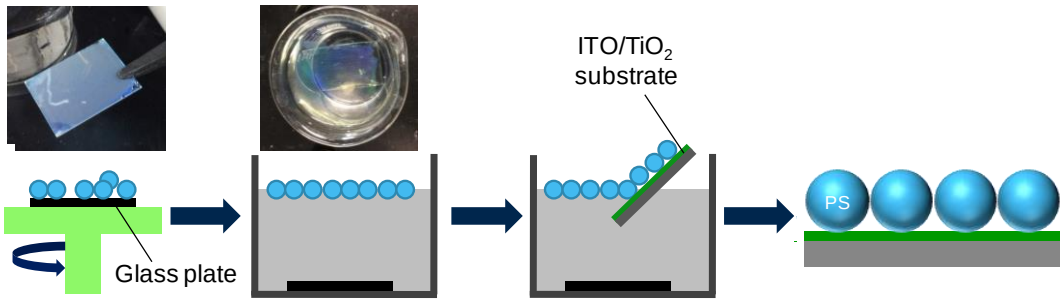

Figure 4.2 Schematic illustration and the corresponding photographs for fabrication of a 2D PS colloidal crystal.

(3) Fabrication of TiO_2 nanohole array and Au deposition

A sandwich technique[14] was employed to infiltrate the prepared TiO_2 sol into the PS template. Typically, the colloidal crystal on ITO/TiO_2 was covered with a smooth glass plate and the two plates were held together with two clips. The TiO_2 sol (10 μL) was dropped onto the gap of the plates. After infiltration, the film was dried for 24 h in air. The infiltration and drying processes were repeated twice. Then, the substrate was immersed in toluene for 15 min to remove the PS spheres and calcined at 500 ºC for 2 h. The Au nanodisk and nanohole structures were obtained through thermal evaporation (0.3 nm s^{-1}, < 4 × 10^{-4} Pa) of Au onto the TiO_2 array. The Au thickness (55 nm) was monitored by a quartz crystal microbalance (QCE).

4.2.2 Characterization

The morphologies of the prepared structures were investigated by a field emission scanning electron microscope (SEM, JSM-7500FA, JEOL) and an atomic force microscope (AFM, SPA400, SII Nanotechnology). Transmittance (*T*) and reflectance (*R*) of the electrodes were measured by a spectrophotometer (V-670, Jasco) equipped with an integrating sphere. Extinction spectra were obtained without the integrating sphere.

4.2.3 Refractive Index Sensitivity Measurements

Refractive index sensitivity was determined by measuring extinction spectra of the obtained electrodes in mixed solutions of water and glycerol. The concentrations of glycerol were 0, 20, 50, and 80 vol%, and the corresponding refractive indices (n) were 1.334, 1.361, 1.394, and 1.436, respectively.

4.2.4 Photocurrent Measurements

Short-circuit photocurrent measurements were performed using a two-electrode and single-compartment cell. The prepared electrode with Au nanodisks and nanoholes and Pt wire were served as the working and counter electrodes, respectively. 0.1 M KNO_3 aqueous solution containing 0.5 M ethanol was used as the electrolyte. Monochromatic light (FWHM = 20 nm, 5.0×10^{15} photons cm^{-2} s^{-1}) was illuminated to the working electrode from the backside (ITO side) using an optospectrum generator (Hamamatsu Photonics).

4.2.5 FDTD Simulation

The optical spectra and electric filed distributions of the plamonic nanostructure were simulated by using a finite-difference time-domain (FDTD) algorithm software (FDTD Solutions, Lumerical Solutions). The calculation model is illustrated in Figure 4.3, where a 55-nm-thick Au nanodisks and nanoholes are located at the bottom and top of a TiO_2 nanohole array, respectively. A periodic boundary condition was imposed in the x and y direction and a perfect matching layer (PML) was imposed in the z direction. The structure was irradiated from the backside with a plane wave source (300−1100 nm), propagating along the z direction and polarized parallel to the x direction. The dielectric functions used for TiO_2 and Au were obtained from literatures reported by Jellison *et al.*[15] and Johnson and Christy,[16] respectively. For comparison, the simulation for the structure only with lower Au nanodisks were also carried out.

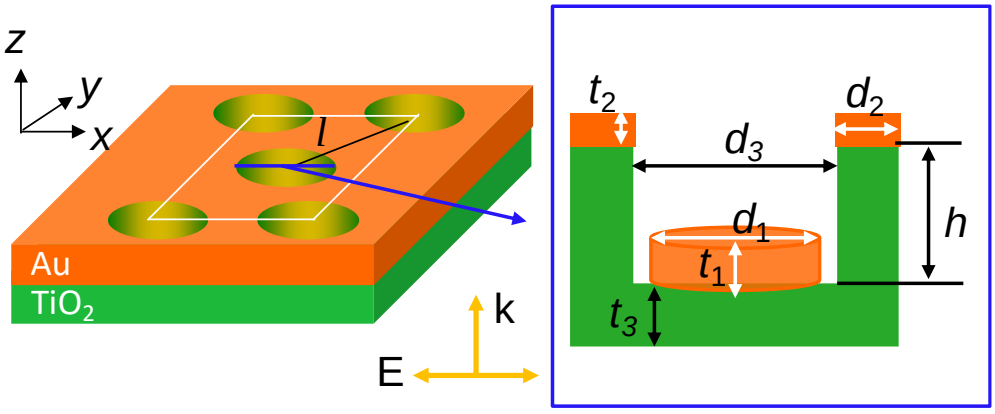

Figure 4.3 FDTD simulation model of the Au nanoholes and nanodisks on TiO_2 nanohole array. The white lines denote the calculation area. The parameters l, d_1, d_2, d_3, t_1, t_2, t_3, and h are 500, 320, 70, 430, 55, 55, 90, and 200 nm, respectively.

4.3 Results and Discussion

4.3.1 Morphology of the PS Colloidal Crystal

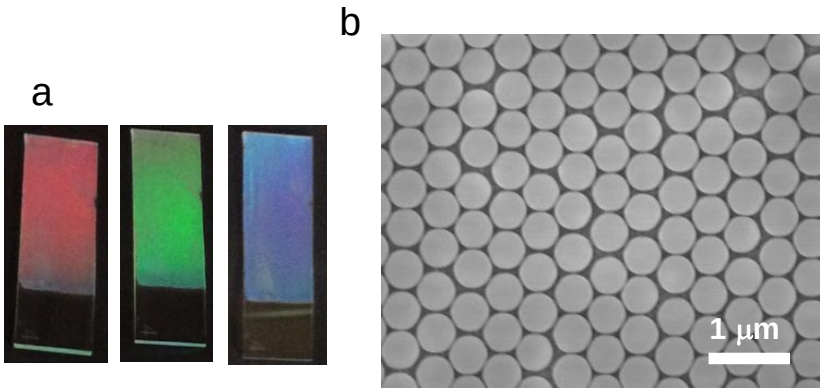

Figure 4.4 (a) Photographs of the 2D PS colloidal crystal showing angle-dependent colors and (b) SEM image of the colloidal crystal.

Figure 4.4a shows photographs of 2D PS colloidal crystal transferred to ITO/TiO_2 substrate. The colloidal crystal exhibited structural colors depending on the observed angle, suggesting the formation of a highly ordered structure. These colors can be explained in terms of Bragg's diffraction law $\lambda = 2d \sin\theta$, where λ is the wavelength of incident light, d is the period of the PS colloidal crystal, and θ is the diffraction angle.[17]

Therefore, the incident light of different wavelengths can be diffracted at different angles. Figure 4.4b shows SEM image of the colloidal crystal. It consists of large-area monolayer domains in which almost all PS spheres are arranged into a hexagonal pattern.

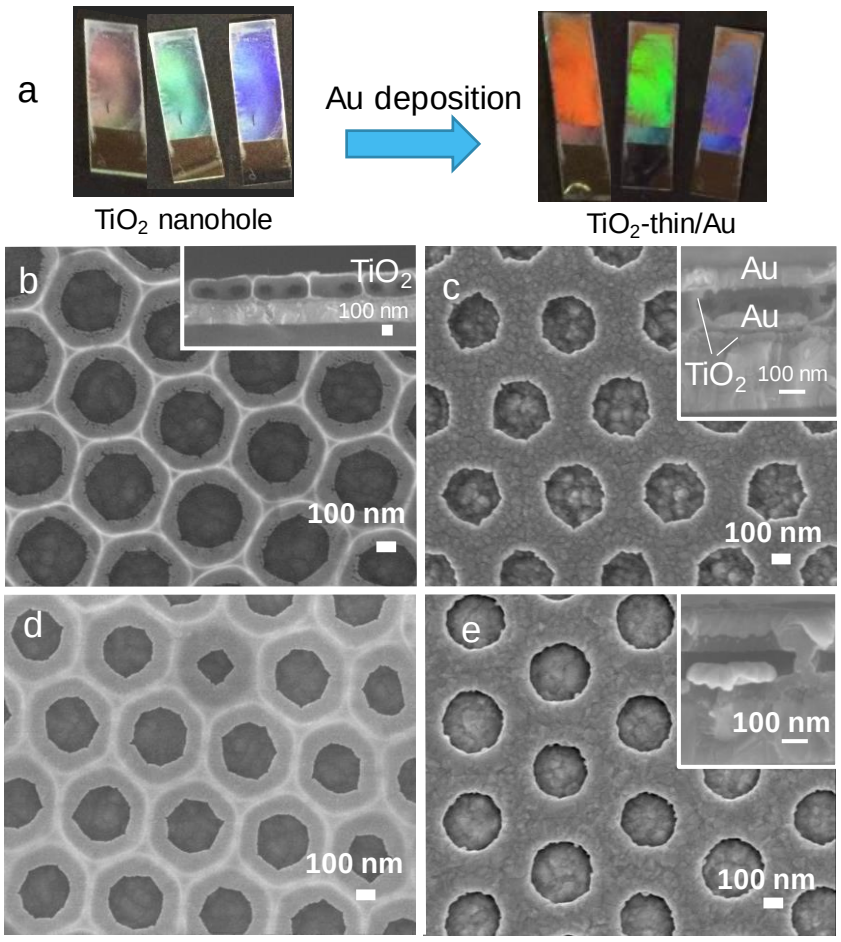

Figure 4.5 (a) Photographs of the prepared TiO_2 nanohole array and TiO_2-thin/Au showing angle-dependent colors. SEM images of TiO_2 nanohole array with (b) thin and (d) thick sidewalls, (c) TiO_2-thin/Au, and (e) TiO_2-thick/Au. The insets are the corresponding cross-sectional SEM images.

The electrode exhibited angle-dependent colors even after infiltration of TiO_2 sol, removal of PS spheres, and calcination as inferred from Figure 4.5a, indicating that the periodicity was maintained during the formation of TiO_2 nanohole array. This is further supported by the SEM investigation (Figure 4.5b). Although it seems that TiO_2 sol forms bowl-like structures (inverted structure of the PS colloidal crystal), the cross-

sectional SEM image (inset of Figure 4.5b) represents flat cylindrical nanoholes aligned on the substrate. This is may be due to shrink of the TiO_2 sol during the calcination process. The nanohole depth was ca. 200 nm and the sidewall thickness can be increased by further TiO_2 coating via the spray pyrolysis technique described in Chapter 2 (1s × 2 times) (Figure 4.5d).

The plasmonic nanostructures were fabricated by depositing Au onto the TiO_2 nanohole arrays shown in Figure 4.5c and e. The resultant nanostructures are denoted as TiO_2-thin/Au and TiO_2-thick/Au, respectively. The structural colors of the electrodes became more vivid than the TiO_2 nanohole template (Figure 4.5a). As can be seen from Figure 4.5c and e, 55-nm-thick Au film are separated into two parts: Au nanodisks and nanoholes on the bottom and top of the TiO_2 nanohole array, respectively. It should be noted that Au was not deposited on the sidewalls of the nanoholes.

4.3.2 Optical Properties and Refractive Index Sensitivities

Figure 4.6a and b show extinction spectra of TiO_2-thin/Au and TiO_2-thick/Au in mixed solutions of water and glycerol with different refractive indices, respectively. The extinction peak of TiO_2-thin/Au located at 624 nm in water (n = 1.334) showed redshifts with increasing the refractive index of the solvent. Since localized surface plasmon resonance (LSPR) peak is very sensitive to refractive index change as discussed in Chapter 1, the peak can be assigned to LSPR of TiO_2-thin/Au. The peak wavelength was plotted against the refractive index as shown in Figure 4.6d. The plot is almost linear and the refractive index sensitivity, which is determined from the slope of the regression line, is 383 nm RIU^{-1} (RIU: refractive index unit). Similarly, the extinction peak of TiO_2-thick/Au at 629 nm (n = 1.334) also showed redshifts with the sensitivities of 393 nm RIU^{-1} (Figure 4.6d).

The extinction spectra of TiO_2-thick/Au with changes of refractive index were further simulated by FDTD, as shown in Figure 4.6c. The shapes of the simulated spectra (Figure 4.6c) are roughly in accordance with those of the experimental ones, although the peaks of the simulated spectra are located at shorter wavelengths, due to the differences of structural parameters between the simulation model and the prepared

electrode. It was also found that the peaks in the simulated spectra were much sharper. This is because the structures used for the FDTD simulation are perfect periodic structures. However, some structural defects exist in the experimentally prepared samples. The refractive index sensitivities of the peaks are 401 nm RIU^{-1} (Figure 4.6d), in agreement with the experimentally obtained value.

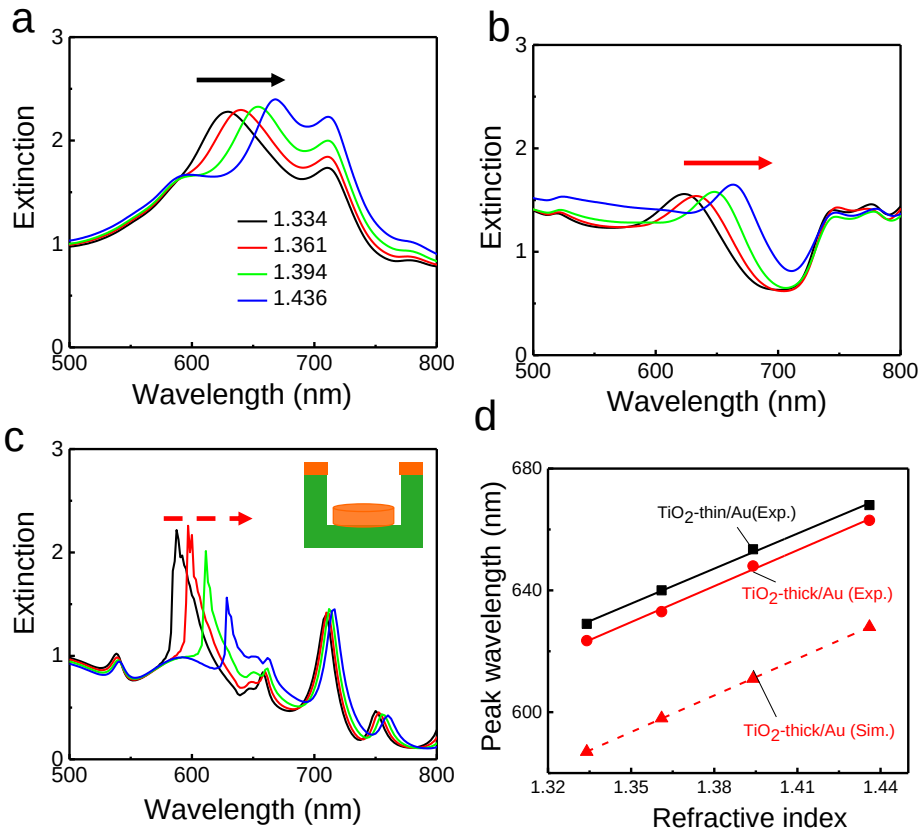

Figure 4.6 Experimentally obtained extinction spectra of (a) TiO_2-thin/Au and (b) TiO_2-thick/Au recorded in water and glycerol-water solutions. (c) FDTD simulated extinction spectra of TiO_2-thick/Au. The black arrow in panel a represent redshift of extinction peaks for TiO_2-thin/Au and the red arrows (solid and dashed) in panel b and c indicate those for TiO_2-thick/Au. Peak wavelengths plotted against the refractive index: obtained from panel a-c.

Figure 4.7 depicts FDTD simulated electric filed distributions of TiO_2-thick/Au irradiated at 587 nm (n=1.334). Both Au nanodisks and nanoholes exhibited localized electric filed, indicating that the peak at 587 nm of the extinction spectrum results from

their LSPR. Thus, it is reasonable to deduce that both of them contribute to the refractive index sensitivity. It has been reported that the refractive index sensitivities of the substrates with Au nanodisks were 128 (diameter = 140 nm) and 171 (diameter = 215 nm) nm RIU^{-1},[18] and those of the substrates with Au nanoholes were 100 (diameter = 60 nm)[19] and 146 nm (diameter = 140 nm) RIU^{-1}.[20] Compared with these results, the developed substrate with Au nanodisks and nanoholes showed much higher sensitivity, maybe due to the interactions between the Au nanodisks and the nanoholes.

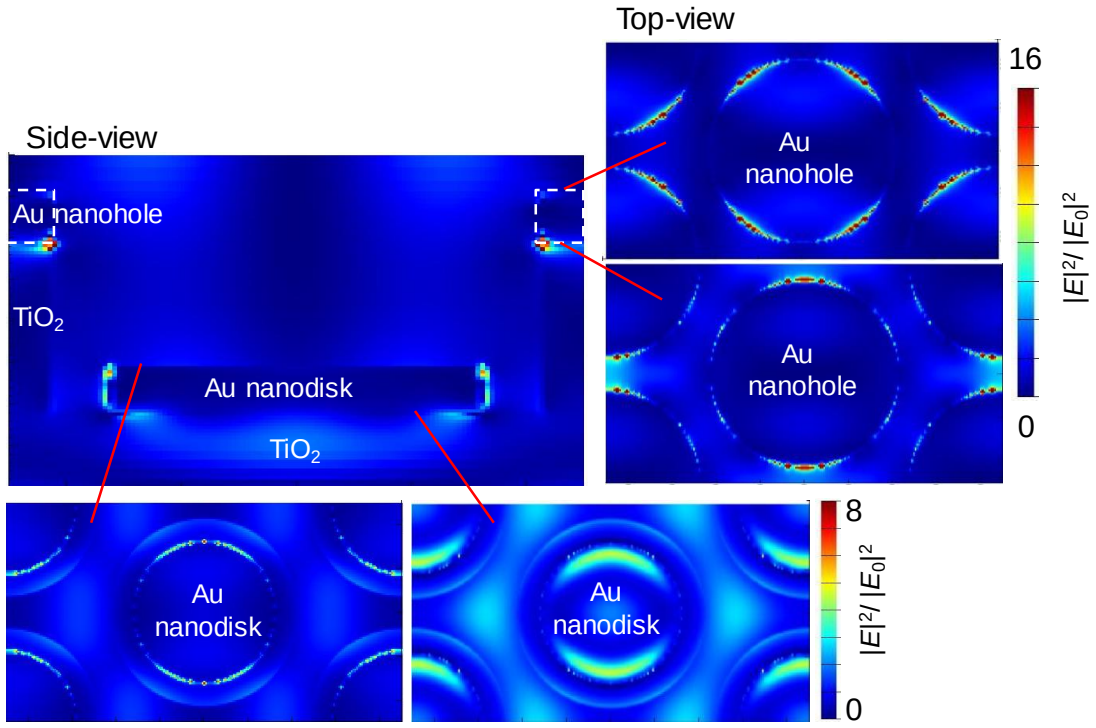

Figure 4.7 FDTD simulated electric field distributions of TiO_2-thick/Au in water (n = 1.334) irradiated at 587 nm.

4.3.3 PICS Behaviors

The optical properties of the electrodes with Au nanodisks and nanoholes were studied experimentally Absorption spectra (A) calculated from T and R of the electrodes ($A = 100 - T - R$). As shown in Figure 4.8a, both electrodes exhibit extensive absorption in the wavelength range examined (300−1000 nm). The broad absorption may contain intrinsic absorption of TiO_2, interband transition of Au, photonic resonance of periodic

structure, and plasmonic absorption of Au nanodisks and nanoholes. Short-circuit photocurrents of TiO_2-thin/Au and TiO_2-thick/Au were measured to evaluate their PICS behaviors. The electrodes exhibited anodic photocurrent responses under light irradiation (440−780 nm), as is the case for Au halfshell array in Chapter 2. Incident photon-to-current conversion efficiency (IPCE) spectra are shown in Figure 4.8b. These results suggest that PICS occurs at the interface between the Au nanostructures (nanodisks and nanoholes) and the TiO_2 nanoholes. Electrons are transferred from the photoexcited Au to the conduction band of the TiO_2 and transported to counter electrodes through an outer circuit, while holes in the Au nanostructures are used for oxidation of the electron donor (ethanol). The IPCE values of TiO_2-thick/Au were higher than those of TiO_2-thin/Au. This is because a sufficient band bending is formed at the interface between thick TiO_2 and Au, thereby achieving a higher PICS efficiency.[21]

The IPCE of the electrode with Au nanodisks and nanoholes was comparable to that of the optimal electrode with Au halfshell array. Further improvement of refractive index sensitivity and PICS efficiency could be realized by optimizing the thickness, size, and geometry of the Au nanostructures.

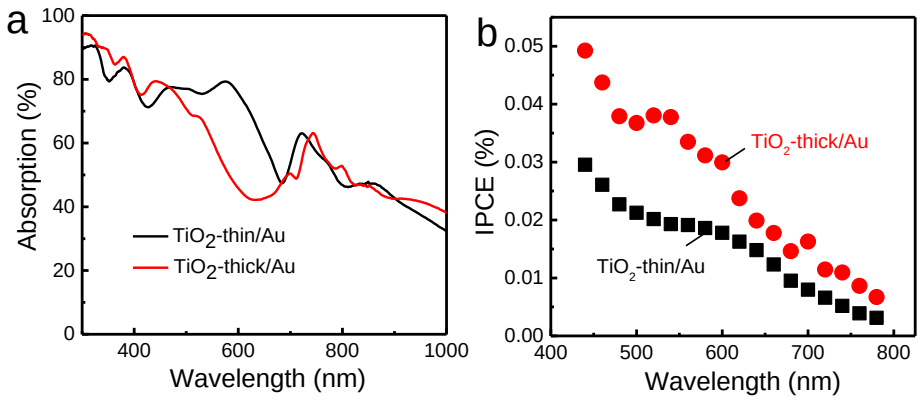

Figure 4.8 (a) Experimentally obtained absorption spectra and (b) Short-circuit anodic photocurrent responses (shown by incident photon to current conversion efficiency, IPCE) of TiO_2/Au photoelectrodes.

4.3.4 Development of Other Plasmonic Nanostructures

It is believed that higher refractive index sensitivity and PICS efficiency can be achieved by tuning the size and geometry of the Au nanodisk and nanohole by using various PS colloidal crystals (Figure 4.9a and Figure 4.10a). Here, the morphology of PS colloidal crystal was changed by exposure to O_2 plasma and UV light.

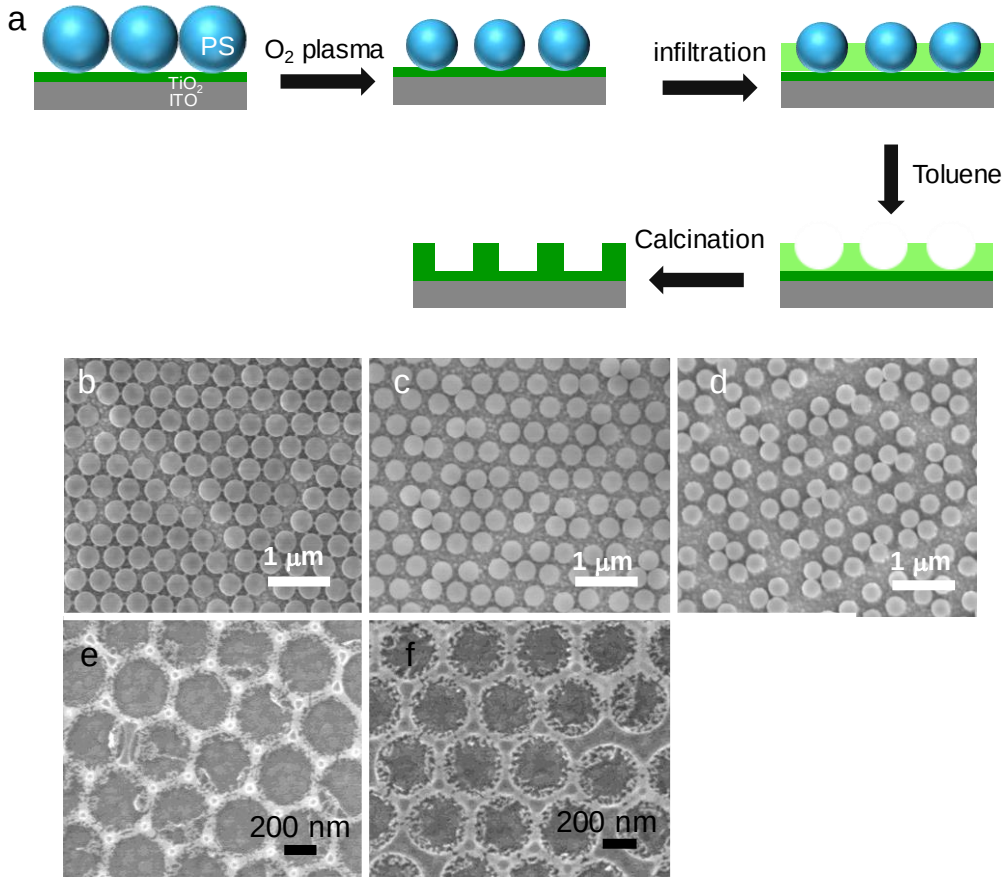

Figure 4.9 (a) Schematic illustration for fabrication of TiO_2 nanohole array by using 2D PS colloidal crystals treated by O_2 plasma. SEM images of 2D PS colloidal crystals after O_2 plasma for (b) 50 s, (c) 70 s, and (d) 100 s. SEM images of the prepared TiO_2 nanoholes by using the PS templates after O_2 plasma for (e) 50 s, (f) 70 s.

As shown in Figure 4.9 b–d, the diameter of PS spheres was decreased with increasing the time of plasma treatment from 50 to 100 s. It should be noticed that PS spheres became disordered after 100 s of plasma treatment. TiO_2 templates (Figure 4.9 e and f) for further deposition of Au nanostructures were obtained by infiltrating TiO_2

sol into the interstitial spaces of the treated PS arrays consisting of PS spheres of different diameters, removal of PS, and annealing (Figure 4.9a). Therefore, the size of the resultant Au nanodisks and nanoholes are readily tuned.

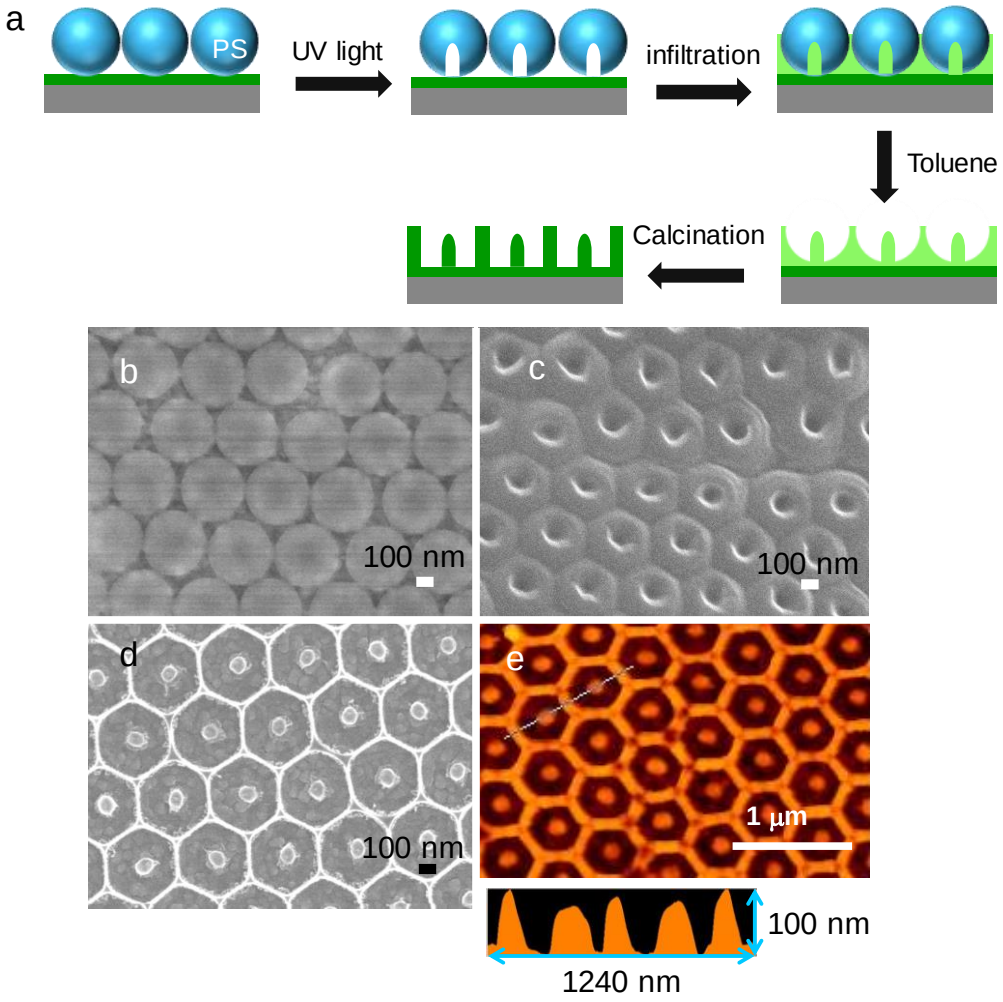

Figure 4.10 (a) Schematic illustration for fabrication of TiO_2 nanohole array by using 2D PS colloidal crystals treated by UV irradiation. SEM images of the (b) top and (c) bottom of a 2D PS colloidal crystal after UV light irradiation for 4 h. (d) SEM and (e) AFM images of the prepared TiO_2 nanoholes with pillars.

Interestingly, the PS array can also be modified by UV light irradiation. As shown in Figure 4.10 b and c, holes were formed at the bottom of PS spheres. It is known that the excitation of TiO_2 under UV light results in the generation of charge carriers which can be used for the oxidation of PS. The oxidation reaction preferentially occurs at the

bottom of the PS spheres to form the holes which accordingly leads to the formation of a TiO_2 template composed of nanoholes with pillars (Figure 4.10 d and e). Obviously, plasmonic film with new geometry can be obtained by using this TiO_2 template.

4.4 Conclusions

In this chapter, ordered plasmonic photoelectrodes with Au nanodisks and nanoholes were developed with the aid of TiO_2 templates which were obtained by inversely duplicating 2D PS colloidal crystals. The extinction peaks assigned to LSPR of Au nanodisks and nanoholes showed redshifts in the wavelength range of 600−700 nm. The refractive index sensitivities of the peaks were determined to be 393 RIU^{-1}, much higher than the reported substrates only with Au nanodisks and nanoholes. The prepared plasmonic electrodes were also applied to PICS. The PICS-based anodic photocurrents were detected in the wavelength range examined (440−780 nm). Further improvement of refractive index sensitivity and PICS efficiency can be realized by optimizing the size and geometry of the Au nanostructures.

4.5 References

1. P. Da, W. Li, X. Lin, Y. Wang, J. Tang, and G. Zheng, *Anal. Chem.*, 2014, **86**, 6633-6639.
2. T. Tatsuma, Y. Katagi, S. Watanabe, K. Akiyoshi, T. Kawawaki, H. Nishi, and E. Kazuma, *Chem. Commun.*, 2015, **51**, 6100-6103.
3. Y. Tian and T. Tatsuma, *J. Am. Chem. Soc.*, 2005, **127**, 7632-7637.
4. T. Tatsuma, H. Nishi, and T. Ishida, *Chem. Sci.*, 2017, **8**, 3325-3337.
5. N. R. Jana and T. Pal, *Adv. Mater.*, 2007, **19**, 1761-1765.
6. N. C. Lindquist, P. Nagpal, K. M. McPeak, D. J. Norris, and S. H. Oh, *Rep. Prog. Phys.*, 2012, **75**, 036501.
7. J. Reguera, J. Langer, D. J. de Aberasturi, and L. M. Liz-Marzán, *Chem. Soc. Rev.*, 2017, **46**, 3866-3885.
8. E. Laux, C. Genet, T. Skauli and T. W. Ebbesen, *Nat. Photonics*, 2008, **2**, 161-164.
9. Y. Shen, J. Zhou, T. Liu, Y. Tao, R. Jiang, M. Liu, G. Xiao, J. Zhu, Z. K. Zhou, X. Wang, C.

Jin, and J. Wang, *Nat. Comm.*, 2013, **4**, 2381.

10. Y. Nishijima, K. Ueno, Y. Yokota, K. Murakoshi, and H. Misawa, *The J. Phys. Chem. Lett.* 2010, **1**, 2031-2036.
11. P. Offermans, M. C. Schaafsma, S. R. Rodriguez, Y. Zhang, M. Crego-Calama, S. H. Brongersma, and J. Gómez Rivas, *ACS Nano*, 2011, **5**, 5151-5157.
12. Z. Yi, G. Niu, J. Luo, X. Kang, W. Yao, W. Zhang, Y. Yi, Y. Yi, X. Ye, T. Duan, and Y. Tang, *Sci. Rep.*, 2016, **6**, 32314.
13. T. Kawawaki, Y. Takahashi, and T. Tatsuma, *Nanoscale*, 2011, **3**, 2865-2867.
14. Z. Cai, J. Teng, Z. Xiong, Y. Li, Q. Li, X. Lu, and X. Zhao, *Langmuir*, 2011, **27**, 5157-5164.
15. G. Jellison Jr, L. Boatner, J. Budai, B. S. Jeong, and D. Norton, *J. Appl. Phys.*, 2003, **93**, 9537-9541.
16. P. B. Johnson and R. W. Christy, *Phys. Rev. B*, 1972, **6**, 4370-4379.
17. K. Sugawa, T. Tamura, H. Tahara, D. Yamaguchi, T. Akiyama, J. Otsuki, Y. Kusaka, N. Fukuda, and H. Ushijima, *ACS Nano*, 2013, **7**, 9997-10010.
18. Y. B. Zheng, B. K. Juluri, X. Mao, T. R. Walker, and T. J. Huang, *J. Appl. Phys.*, 2008, **103**, 014308.
19. J. Prikulis, P. Hanarp, L. Olofsson, D. Sutherland, and M. Käll, *Nano Lett.*, 2004, **4**, 1003-1007.
20. M. P. Jonsson, P. Jönsson, A. B. Dahlin, and F. Höök, *Nano Lett.*, 2007, **7**, 3462-3468.
21. N. Sakai, Y. Fujiwara, Y. Takahashi, and T. Tatsuma, *ChemPhysChem*, 2009, **10**, 766-769.

Chapter 5 Conclusions

This thesis is mainly focused on plasmon-induced charge separation (PICS) behavior of periodic plasmonic metal nanostructures which were prepared by a simple colloidal template method. The fundamental and applied studies on PICS of the developed periodic plasmonic nanostructures were performed.

In Chapter 2, plasmonic photoelectrodes with sputtered Au semishell arrays and halfshell arrays on core-shell SiO_2@TiO_2 colloidal crystals were developed. Compared with the conventional electrodes with disordered Au nanospheres, the electrodes with Au semishell and halfshell arrays exhibited broader and more extensive absorption in the visible and near-infrared (NIR) regions due to both localized and propagating surface plasmon resonances (LSPR and PSPR) resulting in high negative open-circuit photopotential shifts and anodic short-circuit photocurrent responses under light irradiation. The PICS efficiency of the evaporated halfshell arrays was higher than that of the sputtered semishell ones. The halfshell electrode with the middle-sized SiO_2 cores (374 nm) showed the highest photoresponses. The size dependence can be explained in terms of intensity of electric field localized at the junction of Au halfshells which is known to contribute to the PICS efficiency.

In Chapter 3, solid-state PICS photovoltaic cells were developed by taking advantage of the characteristics of the Au halfshell arrays. The halfshell in the cell serves both as light absorber and current collector (counter electrode), allowing the cell to be more simplified. A thicker TiO_2 shell was advantageous for higher photocurrents due to lower series resistance. The cell performance was further improved by introducing MoO_3 and Spiro-OMeTAD as hole transport layers. Ag and Cu halfshell arrays were also fabricated by the same procedure as Au halfshell cell. Compared with the Au and Cu halfshell cells, the Ag one showed much higher photoresponses because of lower Schottky barrier height and higher interband transition energy. Remarkably, the highest incident photon-to-current conversion efficiency (IPCE) of 2.92% and power conversion efficiency (PCE) of 0.112% were achieved among the previously

reported solid-state PICS cells, probably because of the broad-band absorption, simple structure, and good photostability.

In Chapter 4, ordered plasmonic photoelectrodes with Au nanodisks and nanoholes were developed with the aid of TiO_2 templates which were obtained by inversely duplicating 2D PS colloidal crystals. The extinction peaks attributed to LSPR of Au nanodisks and nanoholes showed redshifts in the wavelength range of 600−700 nm. The refractive index sensitivities of the peaks were determined to be 393 RIU^{-1}, much higher than the reported substrates only with Au nanodisks and nanoholes. The PICS-based photoelectrochemical properties were also examined in a liquid cell with ethanol as an electron donor. The PICS-based anodic photocurrents were detected in the wavelength range of 440−780 nm. The IPCE of the electrode with Au nanodisks and nanoholes was comparable to that of the optimal electrode with Au halfshell array. It is expected that further improvement of refractive index sensitivity and PICS efficiency can be realized by optimizing the thickness, size, and geometry of the Au nanostructures.

The most important finding in this work is that a well-defined and continuous plasmonic nanostructure gives rise to broad light absorption, high PICS efficiency, and applicability to sophisticated plasmonic devices.

Further work may focus on development and application of other novel periodic plasmonic nanostructures like nanodome. Ag and Au composite halfshell array is also the candidate to achieve higher photovoltaic performance and photostability.

Abbreviations

AFM	Atomic force microscope
AM 1.5	Air mass 1.5
BEM	Boundary element method
CB	Conduction band
CE	Counter electrode
DDA	Discrete dipole approximation
EBL	Electron beam lithography
EQE	External quantum efficiency
FDTD	Finite difference time domain
FF	Fill factor
FIB	Focused-ion-beam milling
FTO	Fluorine-doped tin oxide
FWHM	Full width at half maximum
HQ	Hydroquinone
HTL	Hole transport layer
IPCE	Incident photon-to-current conversion efficiency
ITO	Indium-tin oxide
KFM	Kelvin probe force microscopy
Li-TFSI	Lithium bis(trifluoromethanesulfonyl)imide
LSPR	Localized surface plasmon resonance
MB	Methylene blue
NHE	Normal hydrogen electrode
NIR	Near-infrared
NPs	Nanoparticles
NR	Nanorod
NS	Nanosphere
NSL	Nanosphere lithography
PCE	Power conversion efficiency
PICS	Plasmon-induced charge separation
PL	Plasmonic material
PML	Perfect matching layer
PS	Polystyrene
PSPR	Propagating surface plasmon resonance
QCE	Quartz crystal microbalance
RE	Reference electrode
RhB	Rhodamine B
RIU	Refractive index unit
SC	Semiconductor
SDS	Sodium dodecyl sulfate
SEF	Surface-enhanced fluorescence
SEM	Scanning electron microscope

Spiro-OMeTAD	2,2′,7,7′-tetrakis(N,N-di-p-methoxyphenylamine)-9,9-spirobifluorene
SPR	Surface plasmon resonance
TEM	Transmission electron microscope
TEOS	Tetraethyl orthosilicate
UV	Ultraviolet
VB	Valence band
Vis	Visible
WE	Working electrode
2D	Two-dimensional
A	Absorption
V_{oc}	Open-circuit voltage
J_{sc}	Short-circuit photocurrent
T	Transmittance
T	Thickness
R	Reflectance
R	Resistance

Appendix

List of Publications

1. L. Wu, H. Nishi, and T. Tatsuma, Plasmon-induced charge separation at two-dimensional gold semishell arrays on SiO_2@TiO_2 colloidal crystals, *APL Mater.*, 2015, **3**, 104406. (Chapter 2)
2. L. Wu, N. Tsunenari, H. Nishi, K. Sugawa, J. Otsuki, and T. Tatsuma, Two-dimensional arrays of Au halfshells with different sizes for plasmon-induced charge separation, *Chemistryselect*, 2017, **2**, 3744-3749. (Chapter 2)
3. L. Wu, G. M. Kim, H. Nishi, and T. Tatsuma, Plasmonic photovoltaic cells based on dual-functional gold, silver and copper halfshell arrays, in revision. (Chapter 3)
4. L. Wu, H. Nishi, K. Akiyoshi, and T. Tatsuma, in preparation. (Chapter 4)

Presentations Related to This Thesis

1. L. Wu, G. M. Kim, H. Nishi, and T. Tatsuma, Plasmon-induced charge separation at two-dimensional metal semishell arrays on SiO_2@TiO_2 colloidal crystals, The 5th CSJ Chemistry Festa, Tokyo, October 2015. (Poster presentation)
2. L. Wu, N. Tsunenari, G. M. Kim, H. Nishi, K. Sugawa, J. Otsuki, and T. Tatsuma, Photoelectrochemistry of plasmonic two-dimensional halfshell arrays and their applications, The 83th Annual Meeting of the Electrochemical Society of Japan, Osaka, April 2016. (Oral presentation)
3. L. Wu, G. M. Kim, H. Nishi, and T. Tatsuma, Photoelectrochemical and photovoltic properties of plasmonic two-dimensional halfshell arrays, Annual Meeting on Photochemistry 2016, Tokyo, September 2016. (Poster presentation)
4. L. Wu, G. M. Kim, H. Nishi, and T. Tatsuma, Plasmon-induced photoelectrochemical and photovoltaic properties of two-dimensional metal halfshell array, The 9th Asian Photochemistry Conference (ACP2016), Singapore, December 2016. (Oral presentation)
5. L. Wu, G. M. Kim, H. Nishi, and T. Tatsuma, Plasmonic photovoltaic cells based on two-dimensional metal halfshell arrays, The 64th JSAP Spring Meeting, Yokohama, March 2017. (Oral presentation)

Awards

1. CSJ Poster Presentation Award for Excellent Research, 2015.
2. Best Presentation Award at the IIS Student Live, 2016.
3. JSPS Research Fellowship DC2, 2017−2019.

Acknowledgments

I would like to express my sincere thanks to all of those who helped me during my doctoral studies in the University of Tokyo. The utmost thanks go to my supervisor, Professor Tetsu Tatsuma, for his patient guidance. I have continuously benefited from his enormous knowledge, unique new ideas, and sophisticated writing skill. His insightful advice made my research go smoothly. I also would like to appreciate his hard work on all the paper that I have published and suggestions about how to make a wonderful presentation. He has helped and inspired me to keep moving on the way to my Doctoral degree even a scientist in the future.

I would like to acknowledge Professor Fujioka, Professor Ishikita, Associate Professor Sunada, and Lecturer Minami for taking their precious time for reviewing my thesis and giving very important and constructive comments. I would like to thank Dr. Sugawa and Ms. Tsunenari of Nihon University for their cooperation in fabrication of SiO_2 colloidal crystals.

I would like to thank Dr. Nishi for his encouragement and fruitful research discussion. I would like to thank Mr. Kuroiwa for operating various instruments and renting apartment.

I would like to express my appreciation to all the colleagues and graduates in the Tatsuma Laboratory for their help and friendships. I would like to appreciate Mr. Nakamura for his help in my entrance exam, my life in Tokyo, and research work. I would like to thank Mr. Asami for his support in my daily life. I will never forget that he sent me back home when I lost my way on the first day, taught me eagerly Japanese, and took care of me so much. I would like to thank Mr. Akiyoshi for his support throughout my doctoral studies. He always helped me when I met problems. I would like to thank Mr. Kim for his collaboration in the research on solid-state cells. I would like to thank Mr. Saito for his help in FDTD simulations. I would like to thank Dr. Kao for his encouragement when I felt frustrated and lost my confidence. I would like to thank Ms. Aizawa, Dr. Ishida, Mr. Lee, Mr. Liu, and Mr. Sugiyama for creating a

pleasant research environment.

I would like to express my gratitude to my friends Dr. Han Zhengli, Dr. Shang Fang, Dr. Tang Zeguo, and Mr. Wang Pujin for productive discussion in theories of electromagnetics, optics, and photovoltaics. All of you made my life more colorful and memorable.

Special thanks to my family: my mother, father, husband, daughter, and my sister. Without your support, love, and encouragement, I could not have finished my research work and thesis.

July 6th, 2017

Wu Ling